Ultra low frequency (ULF) waves observed at mid to low latitudes during daytime using low Earth orbit (LEO) satellite and ground-based data

by

Dzivhuluwani Christopher Ndiitwani

A thesis submitted in fulfilment of the academic
requirements for the Degree of
Doctor of Philosophy
in the School of Physics,
University of KwaZulu-Natal,
Durban

23 February 2011

As the candidate's supervisor I have approved this thesis for submission

Signed: Name: P R Sutcliffe Date: 23-02-2011

As the candidate's co-supervisor I have approved this thesis for submission

Signed: Name: A.D.M. Walker Date: .23/02/2011

Abstract

The launch of German geoscience satellite CHAMP inspired the increased interest in the study of ultra low frequency waves. In this work data from low Earth orbiting (LEO) German CHAMP satellite and South African ground-based magnetometer data were used to study geomagnetic pulsations, in particular continuous pulsations, Pc3, with periods in the range 10-45 seconds. Both Fast Fourier Transform (FFT) and Maximum Entropy Spectral Analysis (MESA) were used as analysis techniques to compute and compare spectra. We simulated a Pc3 oscillation using a sinusoidal function in order to test and establish appropriate parameters to use on the application of these analysis techniques. In this study the region chosen for a low latitude geomagnetic pulsations study excludes high current regions such as polar regions where field aligned currents occur. The structure of low-latitude pulsations was studied by comparing satellite and ground magnetic field measurements. The magnetic field measurements observed in the topside ionosphere by CHAMP were compared to Hermanus data for times when CHAMP crossed the ground station L-shell. The data were analysed for Pc3 pulsation activity using the MESA method to visualise field line resonance (FLR) in the vector magnetometer data. A number of discrete frequency oscillations for the fast mode wave were observed, one of which drives FLR at characteristic latitude as detected by both ground and satellite measurements. The toroidal mode frequency on CHAMP experiences a Doppler shift due to the rapid motion across the resonance region. Polarization hodograms in the resonance region show the expected 90^0 rotation of the field line resonant magnetic field components. We present first time observations of toroidal standing Alfvén mode oscillation with clearly L-dependent frequencies in the inner magnetosphere for $L < 3$. Our observations show FLR frequency continuously increasing as a function of decreasing latitude down to L = 1.6 and then decrease as a result of the larger plasma density of the upper ionosphere. The L-dependent frequency oscillations were observed in the presence of broadband compressional wave spectra. Our observation confirms the well-known magnetohydrodynamic (MHD) wave theoretical prediction of a compressional wave being the driver of the field line resonance, and that the Pc3 pulsations do not have a source with the same frequency structure.

Keywords: ULF waves, Fast Fourier Transform, Maximum Entropy Spectral Analysis, CHAMP satellite, Geomagnetic pulsations, Pc3, Alfvén wave, Field line resonance.

PREFACE

The experimental work described in this thesis for PhD was carried out in Hermanus Magnetic Observatory, Hermanus and the School of Physics, University of KwaZulu-Natal, Durban, from February 2006 to June 2010 under the supervision of Professor Peter Sutcliffe and co-supervision of Professor Dave Walker.

These studies represent original work by the author and have not otherwise been submitted in any form for any degree or diploma to any tertiary institution. Where use has been made of the work of others it is duly acknowledged in the text.

Dzivhuluwani Christopher Ndiitwani

DECLARATION 1 - PLAGIARISM

I,Dzivhuluwani Christopher Ndiitwani declare that

1. The research reported in this thesis, except where otherwise indicated, is my original research.
2. This thesis has not been submitted for any degree or examination at any other university.
3. This thesis does not contain other persons' data, pictures, graphs or other information, unless specifically acknowledged as being sourced from other persons.
4. This thesis does not contain other persons' writing, unless specifically acknowledged as being sourced from other researchers. Where other written sources have been quoted, then:
    a. Their words have been re-written but the general information attributed to them has been referenced
    b. Where their exact words have been used, then their writing has been placed in italics and inside quotation marks, and referenced.
5. This thesis does not contain text, graphics or tables copied and pasted from the Internet, unless specifically acknowledged, and the source being detailed in the thesis and in the References sections.

Signed: Dzivhuluwani 18/03/2011

DECLARATION 2 - PUBLICATIONS

DETAILS OF CONTRIBUTION TO PUBLICATIONS that form part and/or include research presented in this thesis (include publications in preparation, submitted, in press and published and give details of the contributions of each author to the experimental work and writing of each publication)

The publications that form part of research presented in this thesis are given below as Publications 1 and 2. The candidate performed the experimental work as well the writing of the articles. The candidate is listed as the first author in both of the articles citations. The second author is the candidate's supervisor who provided the guidance for the work presented in this thesis. He also proof read the two articles.

Publication 1

Ndiitwani, D. C., Sutcliffe, P. R., 2009. The structure of low-latitude Pc3 pulsations observed by CHAMP and on the ground. Ann. Geophys., 27, 1267-1277.

Publication 2

Ndiitwani, D. C., Sutcliffe, P. R., 2010. A study of L-dependent Pc3 pulsations observed by low Earth orbitting CHAMP satellite. Ann. Geophys., 28, 407-414.

Signed: Dendikwani 18/03/2011

Acronyms

CHAMP	Challenging Minpayload Satellite
DFT	Discrete Fourier Transform
ELGI	Eötvös Loránd Geophysical Institute
FAC	Field Aligned Currents
FFT	Fast Fourier Transform
FLR	Field Line Resonance
HER	Hermanus
IGY	International Geophysical Year
IMF	Interplanetary Magnetic Field
LEO	Low Earth Orbit
LPFF	Low Pass Filtered Field
MESA	Maximum Entropy Spectral Analysis
MHD	Magnetohydrodynamic
SEGMA	South European Geomagnetic Array
SUT	Sutherland
SW	Solar Wind
THY	Tihany
ULF	Ultra Low Frequency
UW	Upstream Wave

Acknowledgments

I thank Heavenly Father for his Grace that has seen me completing this work and letting me study the small portion of his magnificent creation.
I express my gratitude to the following people and institutions:

- Prof Peter Sutcliffe, my supervisor, for the assistance, guidance and for the time he spent on my work despite his busy personal research and managerial activities.
- Prof Dave Walker, my co-supervisor, and Dr Lindsay Magnus for discussions and assistance on various occasions.
- Prof Nancy Van Schaik and Mrs Jeanne Cilliers for evaluating the grammar and spelling of this thesis.
- The GFZ German Space Agency institutions and Goddard's Space Physics Data Facility for providing CHAMP and OMNI data respectively used in this work.
- Mr Balázs Heilig of the ELGI institution in Hungary for the collaboration opportunity and useful discussions during the course of this work.
- The Hermanus Magnetic Observatory (HMO) for financial support and use for their facilities.
- My office mates and HMO students and staff, the likes of Mr Kenneth Maphaha, Sibusiso Mthembu, John Bosco, Stefan Lotz, Emmanuel Nahayo, and Dr Patrick Sibanda e.t.c. for their friendship, assistance with computer related problems and queries and discussions that contributed to this study, most importantly for making my stay in Hermanus pleasant.
- The HMO Managers Dr Sandile Malinga and Dr Lee-Anne McKinnell for their leadership and patience.

A special thanks to:
My grandmother: Vho Matodzi Masindi, parents, siblings, cousins and extended family members for understating my absence from many domestic activities and responsibilities during the course of this study. It is your support and Prayers that have seen me completing this study.
Mrs Shandukani Khorommbi and Ms Azwitamisi Ndiitwani for being the greatest pillar of support.
Tumelo, Fhedzi and Dali for my endless trips from and to O.R. Tambo airport.

Ndaa!

Dedication

To my late grandmother: Vho Munzhedzi “Munengiwa” Maria Ndiitwani

Contents

List of Figures

List of Tables

Chapter 1

Introduction

Magnetometers on board spacecraft and on the Earth's surface detect the magnetic signature of ultra-low frequency (ULF) upstream waves, geomagnetic field line resonances and magnetospheric cavity resonances known as geomagnetic pulsations. These pulsations are manifestations of hydromagnetic waves generated in the magnetosphere by a variety of physical processes and instabilities. Geomagnetic pulsations are characterized by their period and structure as continuous Pc or irregular Pi pulsations (Jacobs et al., 1964). The continuous pulsations are quasi-sinusoidal signals lasting more than several cycles and the irregular pulsations are broadband or short-lived pulsations. In this work we studied the field line resonance (FLR) which is the most frequent characteristic of dayside Pc3 pulsation observed at low latitudes. In this thesis FLR refers to the single frequency driven magnetic field line resonances and continuum ULF field line resonances as discussed by Waters et al. (1995).

The magnetospheric ULF wave phenomenon, monitored by magnetic sensor instruments on board spacecraft, ground magnetometer arrays and ground radars, is a useful magnetospheric system diagnostics tool (Cummings et al., 1969). Magnetospheric magnetic field lines often undergo toroidal (azimuthal) Alfvén wave oscillations. The field lines are tied down (fixed) at the ionospheric boundary and only certain discrete frequencies are allowed which depend on the particular harmonic, just like waves on a string (Dungey, 1954). The harmonic frequencies respond differently to the mass density at various locations along the field line (Denton and Gallagher, 2000) because of the different parallel structures associated with the harmonics. Therefore, because of this close relation between harmonic frequency and mass density the information about the mass density can be determined as a function of a radial distance in the equatorial plane, from the frequencies of the toroidal Alfvén waves (Troitskaya and Gul'elmi, 1967). Ideally, this information can be sensed remotely using ground magnetometers that continuously take measurements of harmonic frequency as done by Menk et al. (1999) and others as indicated in their article. The relationship between the observable ULF wave oscillation parameters and

the dynamics of the magnetosphere that set up the field line resonance makes it possible to diagnose the magnetospheric system using ULF waves. Impulsive Pi2 pulsations are best known for their occurrence at the time of magnetospheric substorm onset and intensification (Sutcliffe and Lühr, 2003). Pi2 pulsations recorded at low latitudes are regarded as one of the clearest indicators of magnetospheric substorm onset and intensification and can consequently play an important role in space weather forecasting. Therefore, understanding geomagnetic pulsations is useful for magnetosphere diagnostics and important for space weather forecasting. However, the current work concentrates on the physics of the ULF wave phenomenon.

The advances in precise high-rate measurements of the geomagnetic field by low-altitude satellites have made it possible to detect ULF waves in the topside ionosphere. Recent observations by low Earth orbiting satellites with high accuracy magnetometers on board e.g. Oersted, CHAMP and ST5, have provided detailed pictures of the Pc3 wave structure in the topside ionosphere. These observations indicate that earlier opinions claiming that comparisons of ULF observations from a low-altitude satellite with ground measurements are not very promising due to the too rapid movement of the satellite, must be revised (Pilipenko et al., 2008). This study utilizes data obtained from the CHAMP satellite orbiting the Earth in the topside F-region ionosphere. This satellite provides magnetic field data of unprecedented accuracy. The satellite was launched into its near circular, almost polar and low altitude orbit at an initial altitude of 450 km on 15 July 2000 from the cosmodrome Plesetsk in Russia (Reigber et al., 2002). The low orbit of this satellite is rather special, being roughly a similar distance above the ionosphere as ground stations are below the ionosphere (Sutcliffe and Lühr, 2003). This provides a unique opportunity of testing MHD theoretical predictions. The effect of ionospheric currents on the propagation of ULF waves can be studied by directly comparing the satellite and ground observations. Previously, the difficulty has been extracting relatively small pulsation perturbation from relatively large background field due to the limited digitisation step of the satellite magnetometer and environmental noise. This led many authors to adopt special techniques to detect pulsation with relatively small amplitudes of only 1 nT or less. The ability of Takahashi et al. (1990) to resolve pulsations from AMPTE CCE data was made possible by averaging highest time resolution to nearly exactly the spacecraft spin period. Takahashi et al. (1999) relied on the interpolation technique in order to resolve pulsations observed by the UARS satellite. The magnetic field measurements from CHAMP are unprecedented in their accuracy and resolution, thus making it possible to extract and resolve clear small amplitude pulsation oscillations from magnetic field data.

The main objective of this work is to study the effect of the ionosphere on the propagation of the causative MHD waves and to understand the coupling between fast and transverse

Alfvén wave modes. This is attempted by using Fast Fourier Transform (FFT) and Maximum Entropy Spectral Analysis (MESA) as analytic tools to calculate spectra estimates for ground and satellite magnetometer data and to compare the two sources of observations. These two methods of spectral analysis are also utilised to study L-dependent Pc3 pulsations. These investigations will improve the understanding of the physical system responsible for the geomagnetic pulsations.

According to MHD models the structure of field line resonant oscillation may be dependent on the frequency spectral content of the fast mode source wave. Our observations confirm this theoretical expectation. In this study two main distinguishable classes of Pc3 pulsations are identified:

- The first class is characterised by a number of discrete fast mode frequency oscillations driving field line resonances at the characteristic latitude as detected by both ground and satellite measurements.
- The second class is characterised by the toroidal oscillations frequency that varies smoothly with L-shells observed in the presence of a broadband source visible on the fast mode source wave frequency spectral content.

The two classes are studied in chapters 5 and 6 respectively. A statistical study of these two classes is presented in chapter 7. This thesis is structured as follows:

Chapter 2 gives an overview of the basic features of the Earth's magnetosphere, including the basic theory of ultra-low frequency ULF oscillations called geomagnetic pulsations. It introduces the relevant terminology used in geomagnetic pulsation studies and discusses the general properties of the Sun, the solar wind, the magnetosphere and its general features, and geomagnetic pulsation. This chapter contains a mathematical derivation of the MHD wave equations that describe the propagation of ULF waves in cold plasma as a solution of Maxwell's equation. The derived MHD wave equation has a two root solution that corresponds to the dispersion relations of the two MHD waves found in a cold plasma. The two waves are the transverse Alfvén and fast magnetosonic waves. This chapter also includes a discussion of the sources of geomagnetic pulsation such as the ULF upstream waves and field line resonance (FLR) including its drivers.

Chapter 3 provides the description of the CHAMP mission and the instruments on board this satellite. We describe both the magnetometers on board CHAMP satellite and on the ground, with more emphasis on the measured magnetic field components and the respective sensor orientations. The satellite has a fluxgate magnetometer (FGM) and an Overhauser

magnetometer (OVM) to measure geomagnetic field precisely. The FGM data was identified as suitable for geomagnetic pulsation studies. The vector magnetometer data suitable for studying wave phenomena were rotated into a geomagnetic field-aligned coordinate system. We briefly describe the method of transforming low pass filtered data into a field-aligned coordinates system. This chapter closes with an experiment that establishes the preferred laboratory for our study of low-latitude Pc3 geomagnetic pulsations.

Chapter 4 introduces FFT and MESA techniques used in this study to compute spectral estimates. This chapter includes a review of the two methods based on the available literature and our work of evaluating and comparing the two methods. We demonstrate that the shortcoming of FFT is its limited resolving power when analyzing short data records and demonstrate the superior resolving power of the MESA technique over the FFT technique by comparing their spectral estimates computed for various signals lengths. In this chapter we determine experimentally the MESA's appropriate parameter values e.g. prediction error filter length (PEF). Inadequate PEF lengths do not yield optimal results and an excessive length introduces spurious peaks into the spectrum. We experimented with real magnetometer data and established the PEF length to be used in this study for ground and satellite data analysis. The ground data has less noise compared to the satellite data and requires a shorter length as demonstrated by experimenting with the modelled Pc3 structure. The satellite data noise level is higher and a longer length is required. The established values are used throughout this work for data analysis. This chapter includes a short description of the crossphase technique used to facilitate the detection of FLR. This technique requires at least two stations in the same meridian, forming a pair. We used the Hermanus and Sutherland stations which are 220 km apart.

In **chapter 5** a number of MHD theoretical predictions are tested and confirmed by comparing satellite and ground data sets. This chapter also illustrates the effect of ionospheric currents such as Hall and Pederson currents on the propagation of MHD waves by comparing magnetic field measurements for times when CHAMP was passing over the ground stations. These currents cause modification to the wave modes transmitted through the ionosphere. The results presented agree with the first CHAMP Pc3 observation of Vellante et al. (2004). However, our analysis differs from theirs and we used an independent data set. We plot the dynamic spectra on a logarithmic scale to emphasise the oscillations at lower power levels. Parts of chapter 5 have been published by Ndiitwani and Sutcliffe (2009).

Chapter 6 presents a study of L-dependent Pc3 pulsations observed by CHAMP in the inner magnetosphere. The continuous movement of CHAMP across different L-shells provided

this opportunity. To interpret our observations we applied a theoretical model developed by Hasegawa et al. (1983) which explains how local field lines are excited in response to fast mode signature characterised by a broadband spectral content. We report first-time observation of Pc3 toroidal oscillations with a clear L-dependent frequency for lower L-shell values (L $<$ 3) observed by a LEO satellite. The results of chapter 6 are observational evidence that the conventional FLR mechanism established by Hasegawa et al. (1983) can be adopted even in the very low latitudinal region of $L < 3$. Parts of this chapter have been published by Ndiitwani and Sutcliffe (2010).

In **chapter 7** we carry out the statistical study of events described in chapters 5 and 6. **Chapter 8** provides the summary and conclusion about the findings of this study.

Chapter 2

The Magnetosphere and Geomagnetic Pulsations

2.1 Introduction

This work is devoted to the study of quasi-sinusoidal oscillations of the Earth's magnetic field called geomagnetic pulsations. This study concentrates on the investigation of the structure of regular and continuous pulsations which draw their ultimate energy from the solar wind. These pulsations are believed to be hydromagnetic waves in the Earth's magnetosphere. Therefore, this chapter introduces the reader to the concepts of geomagnetic pulsations and the magnetosphere.

The chapter starts with brief discussions of well known aspects of space physics applicable to this thesis, the Sun and the solar wind. It also briefly discusses the link between the solar wind and the source geomagnetic pulsation observed on the ground. This chapter is also meant as a review of studies related to this work.

2.2 The Sun and the solar wind

Our nearest star, the Sun, is a rotating star which consists of ∼90% hydrogen and ∼10% helium with a small fraction of heavier elements such as carbon, nitrogen and oxygen. It is a star of intermediate size and luminosity with radius $r_{\odot} \sim 696000$ km (~ 0.005 AU). The Sun has a differential rotational period that increases with latitude from an average of 25 days at the equator up to 32 days near the poles. This odd behavior is due to the fact that the Sun is not a solid body like the Earth but rather a large "sphere of plasma" that is gravitationally bound and compressed leading to high temperatures and densities in the core. The solar atmosphere consists of four layers. The visible solar surface over the convective zone is called the

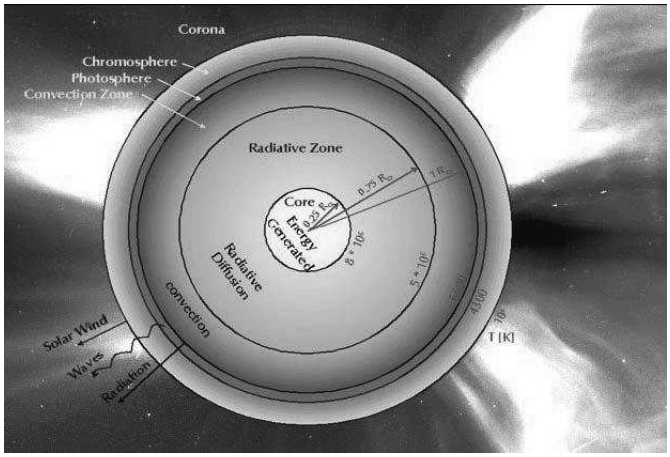

Figure 2.1: *This figure shows the layers of the Sun discussed in the text with the addition of convection and radiative zones (from www.oulu.fi/spaceweb/textbook/sun.html).*

photosphere. Above the photosphere there are two transparent layers: the chromosphere which extends some 10 000 km above the photosphere and the corona which is observable beyond the chromosphere for more than 10^6 km (Ferreira, 2002). The corona is the outer most layer of the Sun and expands into interplanetary space and becomes the solar wind. The visualization of the Sun's atmosphere described above is illustrated in Figure 2.1.

The plasma atmosphere of the Sun constantly blows away from its surface to maintain equilibrium (Parker, 1958, 1963), a phenomenon called the solar wind. It is a result of the huge difference in gas pressure between the solar corona and interstellar space. This pressure difference drives the plasma outward, despite the restraining influence of solar gravity (e.g. Hundhausen, 1995). The solar wind was discovered by Biermann (1951) when he observed that comet tails point directly away from the Sun and the first mathematical model was established by Parker (1958).

The nature of the Sun's magnetic field influences the speed of the solar wind. In the equatorial regions of the Sun the magnetic field begins and ends on the solar surface. These closed field lines result in a slow solar wind with a speed of $\sim$400 km.s^{-1}. At solar polar regions the field lines are open and are the sources of 800 km.s^{-1} fast solar wind. This latitude dependence of the solar wind speed was confirmed by Ulysses spacecraft observations (McComas et al., 1995; Phillips et al., 1995). The solar wind carries the Sun's magnetic field giving rise to the interplanetary magnetic field (IMF). This is because of high electrical conductivity of the solar wind such that the diffusion of magnetic field through the plasma is negligible and the field lines can be treated as being "frozen in" the plasma. Hence the actual solar wind is a flow of ionised solar plasma and a remnant of the solar magnetic field that pervades interplanetary

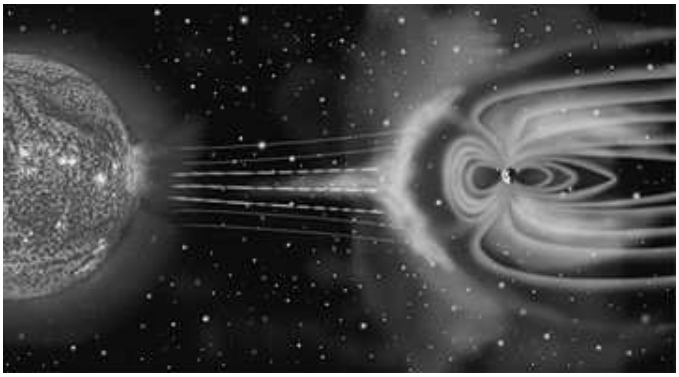

Figure 2.2: *Artist's impression and representation of the magnetosphere (from NASA website).*

space.

2.3 The Magnetosphere

In this section the magnetosphere formed by the interaction between the solar wind and Earth's magnetic field is discussed. Our planet, the Earth, is itself a huge magnet (Gilbert, 1600) and if the Earth were isolated in space the magnetic field would be approximately dipolar. Above the ionosphere the Earth's magnetic field, which extends out to a distance of the order of 10 Earth radii(R_E) on the dayside, dominates control over the motions of gas and fast charged particles. At $\sim 10\ R_E$ magnetic field energy density is of the same order as the solar wind energy density and the geomagnetic field has a significant effect on the solar wind. A balance is set up between the dynamic pressure of solar wind and static magnetic pressure of the Earth's magnetic field so that the plasma pressure decreases rapidly with increasing magnetic field. Charged particles mainly from the solar wind e.g. protons and electrons, are deflected in opposite directions by the Earth's main field creating a boundary current sheet called Chapman-Ferraro currents (Chapman and Ferraro, 1931a). The magnetic field effect of the Chapman-Ferraro current sheet is such as to cancel the geomagnetic field everywhere on the sunward side of the current sheet (e.g. Chapman and Ferraro, 1931b,c). The magnetic field is increased by this current sheet on the earthward side and immediately on the Earth-side of the sheet, the field is doubled. The net effect is that the Earth's magnetic field acts as an obstacle to the solar wind which is deflected around it, carving out a cavity known as the magnetosphere. The boundary between the magnetosphere and the solar wind where the Chapman-Ferraro current flows is called the magnetopause. The location of the magnetopause is determined by the pressure balance between the solar wind pressure and the pressure of the magnetic field. The balancing point primarily depends on the speed and density of the solar wind.

The discovery of the magnetosphere was popularised in 1958 during the International Geo-

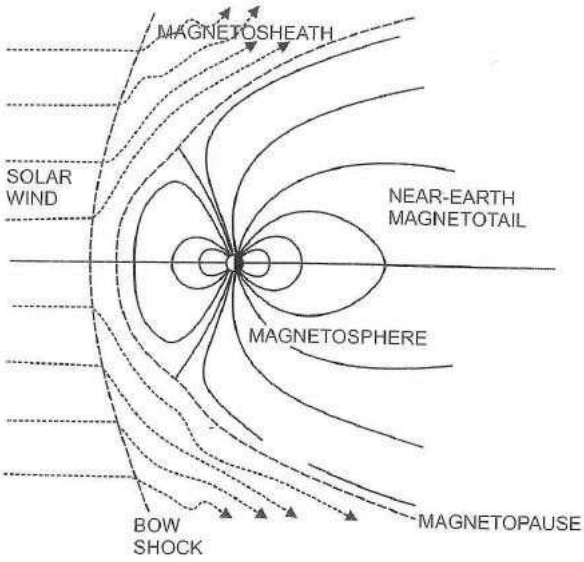

Figure 2.3: *A sketch of the closed magnetosphere including the bow shock (Walker, 2005).*

physical Year by Explorer 1 observations and the name was proposed by Gold (1959). Figure 2.2 shows an artist's impression of the magnetosphere (taken from the NASA website). The Sun is shown on the left clouded by the solar wind drifting towards the Earth as indicated by the stream lines which then interact with the geomagnetic field as they approach the Earth.

2.3.1 The closed magnetosphere model

Theoretical studies of the shape of the magnetosphere were carried out by Beard (1960); Mead and Beard (1964); Midgley and Davis (1963); Slutz and Winkelman (1964); Spreiter and Briggs (1962). These studies reviewed by Mead (1967) postulate that the magnetosphere boundary shape is determined by a pressure balance between the solar wind and the geomagnetic field. In their mathematical models a number of simplifying assumptions were made. The most important one was that the solar wind plasma was assumed to be completely field-free and at zero temperature, so that the dipole field becomes completely enclosed (Mead, 1967). This led to the *closed* model concept of the magnetosphere shown in Figure 2.3. The schematic representation shown in Figure 2.3 (from Walker, 2005) is the simplest, where the magnetic field is confined to the inside of the magnetosphere and the plasma to the outside. When the solar wind plasma on the outside encounters the Earth's dipolar magnetic field it cannot simply penetrate it but rather is slowed down and a shock called the bow shock (see Figure 2.2) is created (Baumjohann and Treumann, 1997). When solar wind plasma encounters an obstacle such as a planet's magnetic field the flow is deflected around the obstacle either by Lorentz forces or by collisions brought about by electromagnetic forces (www.physics.usyd.edu; Cravens, 1997).

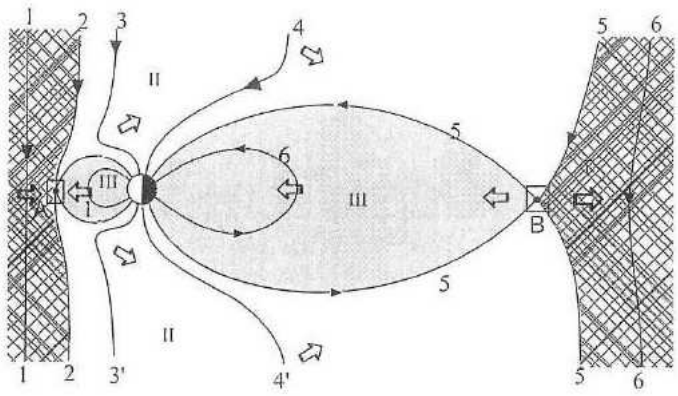

Figure 2.4: *A schematic representation of open magnetosphere suggested by Dungey (1961). Shown is the magnetic field configuration in the noon-midnight meridian for a southward solar wind field (figure from Walker, 2005).*

The physics of the bow shock embraces solar wind magnetosonic speed dynamics. The solar wind flows at a speed greater than any magnetosonic wave and as in any standard gasdynamical flow, the supersonic winds are deflected around the object. These processes lead to the formation of a bow shock (Russell, 1979, 1985, 1987; Spreiter and Stahara, 1985). The effect of bow shock is to decrease the speed of the solar wind from supersonic to subsonic speed as it flows around the magnetosphere. As shown in Figure 2.3 the bow shock has an almost parabolic shape symmetrical around the Sun-Earth line and the conditions that set up bow shock occur at $\sim$14 R_E (Burgess, 1995). The Earth's bow shock is about 100-1000 km thick. The model sketched in Figure 2.3 is oversimplified but regarded as a first approximation of the magnetospheric behaviour. On the day (upstream) side at the magnetopause boundary location it is understood that the dynamic pressure of the solar wind balances the static pressure of the geomagnetic field. On the night (downstream) side the cavity extends into a long magnetic tail.

2.3.2 The open magnetosphere model

In the closed magnetosphere model the solar wind impinging on the Earth's magnetic field cannot simply penetrate the magnetic field but flows around magnetic field lines. This is a consequence of the frozen magnetic field theorem which states that (in the absence of, for example, resistivity) the plasma particles which are located on a certain magnetic field line at one time are constrained in their motion to stay on that same field at all times. In other words, a plasma like the solar wind cannot simply leave interplanetary field lines and invade a planetary magnetic field (Paschmann, 1991). In Figure 2.3 the IMF is compressed against the magnetopause and draped over it by the flow, but ultimately the field lines slip around the sides of the magnetosphere, frozen into the magnetosheath plasma (Dungey, 1961). The frozen-

in-plasma approximation breaks down when high current densities are present in the plasma such as those occurring at the magnetopause boundary (Dungey, 1961, 1963, 1965). James Dungey, in the early 1960s, was the first to recognize the importance of this breakdown and to study its consequences leading to the concept of open magnetosphere model shown in Figure 2.4

At the subsolar point the frozen-in condition is relaxed; the field diffuses relative to the plasma in the magnetopause allowing the interplanetary field and terrestrial field lines to connect through the boundary. This leads to the formation of a neutral point at the subsolar point. The neutral point is designated A in Figure 2.4. Under these circumstances magnetic merging or reconnection takes place. This concept is illustrated in Figure 2.4. In the figure the IMF appears to have succeeded in connecting to the initially closed magnetospheric field lines on the day side. Thus, the closed lines become open (i.e. tail) field lines that are drawn toward the current sheet as the solar wind carries the IMF downstream. Because the Earth's magnetic field now extends into the magnetosheath region, such a model is called an *open* magnetosphere (e.g. Dungey, 1961, 1963).

However, unlike the theoretical models in which the magnetosphere is usually described as a container of charged particles, the magnetosphere is a dynamic entity. The waves in which we are interested, propagating through this dynamic magnetosphere usually have short periods compared with the time scale on which the gross structure changes. This work concentrates on the study of ultra low frequency (ULF) magnetic oscillations which are magnetohydrodynamic waves.

2.4 Magnetohydrodynamic waves

The word *magnetohydrodynamics* (MHD) is derived from *magneto*, meaning magnetic field, *hydro*, meaning liquid and *dynamics* meaning movement (Alfvén, 1942). The magnetohydrodynamics studies concentrate on understanding the motion and dynamics of compressible conducting fluids in the presence of magnetic fields. The wave modes derived using MHD plasma theory are called magnetohydrodynamic waves. In this section we derive MHD waves equations as a solution to Maxwell's equations in the low frequency limit:

$$\frac{\partial \mathbf{B}}{\partial t} = -\nabla \times \mathbf{E} \tag{2.1}$$

$$\nabla \times \mathbf{B} = \mu_0 \mathbf{j} \tag{2.2}$$

with the requirement that $\mathbf{B}$ be divergenceless:

$$\nabla.\mathbf{B} = 0 \tag{2.3}$$

where $\mathbf{j}$ is the current defined by Ohm's law:

$$\mathbf{j} = \sigma_0 \left(\mathbf{E} + \mathbf{u} \times \mathbf{B}\right) \tag{2.4}$$

In most circumstances in the magnetosphere the terms $\mathbf{j}/\sigma_0$ can be ignored and the pressure gradient can be neglected (Walker, 2005). Therefore, Ohm's law instead of relating current density and electric field becomes a relationship between the plasma velocity and the electric and magnetic fields.

$$\mathbf{E} + \mathbf{u} \times \mathbf{B} = 0 \tag{2.5}$$

Neglecting the pressure gradient term, the conservation of momentum is assured by:

$$\rho \frac{\partial \mathbf{u}}{\partial t} = \mathbf{j} \times \mathbf{B} \tag{2.6}$$

We are searching for wave like solutions in which perturbed quantities vary like $exp\left(i\mathbf{k}.\mathbf{r} - \omega t\right)$. The operator $\frac{\partial}{\partial t}$ can then be replaced by $-i\omega$; therefore equations 2.1 and 2.6 becomes:

$$\nabla \times \mathbf{E} = i\omega \mathbf{B} \tag{2.7}$$

$$-i\omega\rho\mathbf{u} = \mathbf{j} \times \mathbf{B} \tag{2.8}$$

From equation 2.7:

$$\nabla \times (\nabla \times \mathbf{E}) = i\omega \nabla \times \mathbf{B} \tag{2.9}$$

Using equation 2.2 equation 2.9 can be expressed as

$$\nabla \times (\nabla \times \mathbf{E}) = i\omega\mu_0 \mathbf{j} \tag{2.10}$$

The perpendicular component of 2.9 from 2.10:

$$\mathbf{B} \times \{\mathbf{B} \times \nabla \times (\nabla \times \mathbf{E})\} = i\omega\mu_0 \mathbf{B} \times \{\mathbf{B} \times \mathbf{j}\} \tag{2.11}$$

From 2.8 equation 2.11 can be expressed as:

$$\mathbf{B} \times \{\mathbf{B} \times \nabla \times (\nabla \times \mathbf{E})\} = i\omega\mu_0 \left\{i\omega\rho \mathbf{B} \times \mathbf{u}\right\} \tag{2.12}$$

From equations 2.5 and 2.12 it can be deduced that:

$$\mathbf{B} \times \{\mathbf{B} \times \nabla \times (\nabla \times \mathbf{E})\} = -\omega^2 \rho \mu_0 \mathbf{E} \tag{2.13}$$

Therefore, the wave equation describing propagation of hydromagnetic waves in a cold and collisionless magnetised plasma with infinite conductivity is:

$$\mathbf{V_A} \times \mathbf{V_A} \times \nabla \times \nabla \times \mathbf{E} = -\omega^2 \mathbf{E} \tag{2.14}$$

The parameter V_A is the Alfvén velocity which relates to the magnetic field and the mass density:

$$\mathbf{V_A} = \frac{\mathbf{B}}{\sqrt{\mu_0 \rho}} \tag{2.15}$$

In the set of equations given above ρ is the mass density, $\mathbf{u}$ is the flow velocity, $\mathbf{j}$ is the current density, $\mathbf{B}$ is the magnetic field, μ_0 is the magnetic permeability of free space, and $\mathbf{E}$ is the electric field. The simplest system in which MHD waves exist is the cold plasma state. In this state the plasma pressure can be neglected although the temperature is not necessarily zero. In a cold plasma the ratio of the plasma pressure to the magnetic pressure is less than unity, $\beta = \frac{p}{B^2/2\mu_0} \ll 1$.

The dispersion relation and wave velocities at which MHD waves propagate are next derived as the solution of the equation 2.14. We shall limit our derivation to a cold plasma case. First noting the vector identity that $\mathbf{A} \times \mathbf{A} \times \mathbf{B} = -A^2 \mathbf{B}_\perp$, equation 2.14 can be expressed as:

$$(\nabla \times \nabla \times E)_\perp = \frac{\omega^2}{V_A^2} E_\perp \tag{2.16}$$

Assuming a dependence in the form $e^{i\mathbf{k}.r}$, ∇ can be replaced by $i\mathbf{k}$ then equation 2.16 can becomes:

$$(\mathbf{k} \times \mathbf{k} \times \mathbf{E})_\perp = -\frac{\omega^2}{V_A^2} \mathbf{E}_\perp \tag{2.17}$$

With the aid of the vector identity equation 2.17 can be expressed as

$$\left[(\mathbf{k}.\mathbf{E})\,\mathbf{k} - k^2 \mathbf{E}\right]_\perp = -\frac{\omega^2}{V_A^2} \mathbf{E}_\perp \tag{2.18}$$

Taking the components of 2.18 separately x component yields:

$$\left(\frac{\omega^2}{V_A^2} - k_z^2\right) E_x = k_y \left(k_y E_x - k_x E_y\right) \tag{2.19}$$

and y component yields:

$$\left(\frac{\omega^2}{V_A^2} - k_x^2 - k_z^2\right) E_y = -k_x k_y Ex \tag{2.20}$$

Equations 2.19 and 2.20 are two coupled equations of which if we consider no y-dependence, $k_y = 0$, the two equations decouple such that x and y components are respectively expressed as:

$$\left(\frac{\omega^2}{V_A^2} - k_z^2\right) E_x = 0 \tag{2.21}$$

$$\left(\frac{\omega^2}{V_A^2} - k^2\right) E_y = 0 \tag{2.22}$$

The two roots i.e. equations 2.21 and 2.22 are associated with modes of MHD waves found in a cold plasma. In a cold uniform plasma where the thermal pressure can be neglected there are two wave modes which propagate:

- The transverse Alfvén wave, which is an incompressional regular Alfvén wave which has energy propagated exactly along the field (Walker, 2005), causes the field lines to bend. The perturbations are all perpendicular to **B** like a propagation of a wave along a guitar string.
- The fast magnetosonic wave is compressional and roughly isotropic. The perturbations in the field are under an oblique angle, so that the separation between field lines varies.

The transverse mode dispersion relation depends only on the component of $\mathbf{k} \parallel \mathbf{B}$, $k_\parallel$. Therefore, the dispersion relation of transverse Alfvén mode deducible from equation 2.21 and can be expressed as

$$\omega^2 = k_\parallel V_A^2 \tag{2.23}$$

where $k_\parallel = \mathbf{k}.\mathbf{B}/B$. This implies that its group velocity is parallel to **B** and field guided. The velocity perturbation is in the direction perpendicular to the plane containing the wave vector and the magnetic field (Southwood, 1985). These Alfvén waves propagate at a velocity

$$V_{ph} = V_A^2 cos\,(\theta) \tag{2.24}$$

where θ is the angle between the wave vector k and magnetic field **B**. The dispersion relation of the fast mode is deduced from equation 2.22:

$$\omega^2 = k V_A^2 \tag{2.25}$$

and propagates at Alfvén velocity

$$V_{ph} = V_A. \tag{2.26}$$

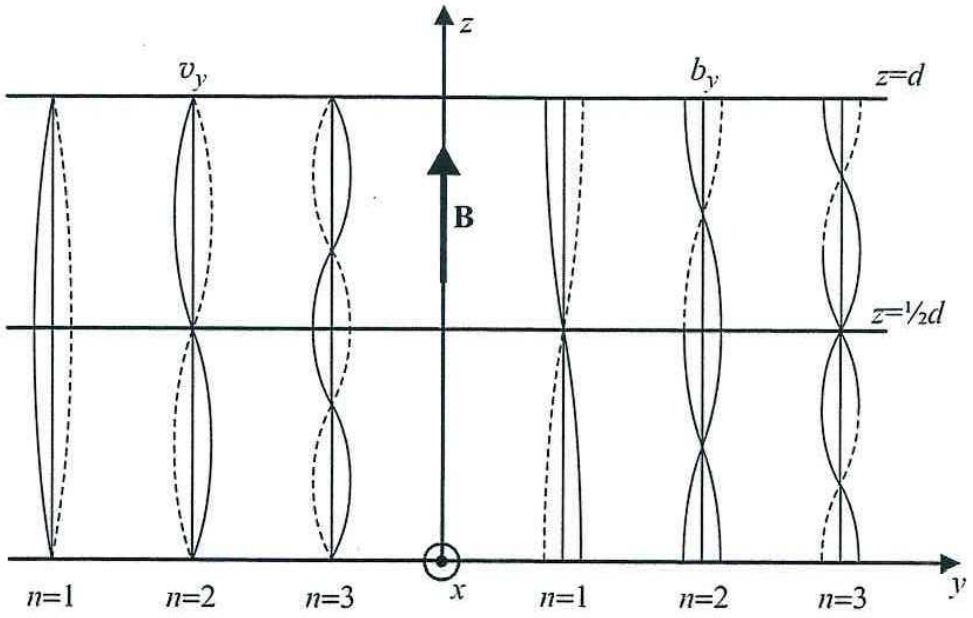

Figure 2.5: *Tranverse Alfvén wave modes in cartesian geometry (adopted from Walker, 2005). Shown are the velocity perturbation* $v_y \propto exp(-i\omega t)sink_z z$ *which is zero wherever* $k_z z = n\pi$ $n = 1, 2, 3, ...$ *and the corresponding magnetic field perturbation* $b_y \propto -k_z exp(-i\omega t)cosk_z z$.

This fast mode wave changes the density of the fluid and the magnetic pressure and is therefore referred to as a compressional wave.

2.5 Standing waves

This section is complementary to the previous section, where the MHD waves in the context of propagating waves were introduced. Here we introduce the concept of a wave in bounded media, called a standing wave. This phenomena is important for studying and understanding oscillations in bounded media that occurs in the magnetosphere. The transverse mode Alfvén waves that propagate along the closed field line are reflectable by the ionosphere through which the magnetic field line passes, setting up a standing wave between the two ionosphere. The simplest case of MHD standing waves exist in the model in which the field lines are straighted and the region is bounded by the magnetopause, the polar cap boundary and the ionospheres. The transverse mode dispersion relation in equation 2.23 depends on parallel wave number so that the lowest frequency can have arbitrary structure perpendicular to magnetic field line (**B**) but because of the requirement of slow variation along **B** such signals will have a standing structure along **B** (Southwood and Hughes, 1983). The nature of oscillation of standing wave system is shown in Figure 2.5. The figure shows resulting standing wave velocity and magnetic field perturbation on the left and right hand side respectively. The perturbation on the left shows the nodes at the ionosphere and on the right show the antinodes at the ionosphere. This

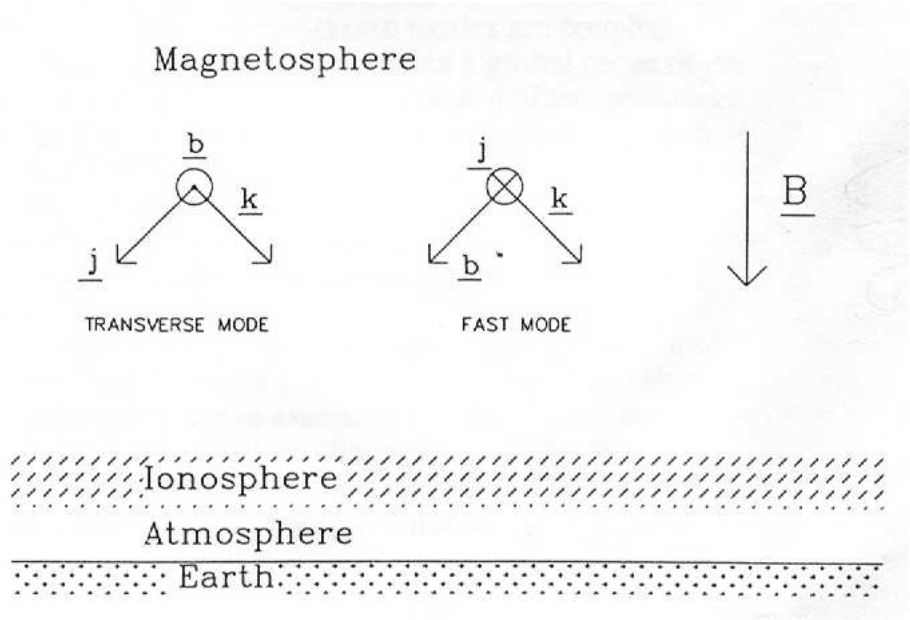

Figure 2.6: *Schema of the polarization of the transverse (shear Alfvén) wave [left] and the fast mode [right] obliquely incident on the ionosphere from the magnetosphere. (Adopted from Kivelson and Southwood (1988).)*

is a scenario of a transverse Alfvén standing wave in a uniform medium with the magnetic field in the z-direction, and having wave vector k in the x-z plane. As a result of the standing structure the wave field exhibits some symmetry about the midpoint at $z = 1/2d$, where d is the separation of the conducting plane. If the ionosphere is treated as as a perfectly conducting boundary, the standing oscillation of the magnetospheric dipole field line adopts a similar structure and should exhibit some symmetry about the field line equator. If north-south symmetry is assumed in the background field, the fundamental structure should have electric field, field displacement and plasma velocity perturbation symmetric about the equator while the transverse magnetic field perturbation is antisymmetric. In contrast, the next higher harmonic has a transverse magnetic perturbation that is symmetric about the equator and **E** field an field displacement and velocity perturbation that are antisymmetric (Southwood and Kivelson, 1981).

2.6 The effect of ionospheric currents on MHD wave propagation

The picture of a standing wave is modified when a finite conductivity is introduced. Figure 2.6 shows the configurations of fast and transverse Alfvén mode wave perturbations for waves incident on a flat ionosphere at height h above the ground in the presence of a vertical background magnetic field, **B** (Kivelson and Southwood, 1988). In the non-uniform plasma of the

magnetosphere, there is always a degree of coupling between the two wave modes. When propagated from the magnetosphere to the ground these wave modes are affected by the ionosphere and atmosphere. The ionosphere presents an interface between magnetosphere and atmosphere that couples the fast and transverse Alfvén wave modes (Yoshikawa and Itonaga, 1996, 2000).

In the lower ionosphere the electrons are essentially collision-free and provide a Hall current through **ExB** drift while the ion motion is dominated by collisions with neutrals and provides the Pederson current. These currents cause modifications to the wave modes as they are transmitted through the ionosphere and the atmosphere (Hughes and Southwood, 1976). Pedersen currents in the ionosphere shield the incident magnetic field from the ground. The signal below the ionosphere is due to the ionospheric Hall currents which are at right angles to the Pedersen currents. The magnetic signal on the ground is rotated through 90^0 with respect to the magnetic field of the transverse Alfvén mode in the magnetosphere because the signal below the ionosphere is proportional to the Hall current (Kivelson and Southwood, 1988). According to Kivelson and Southwood (1988) the ionosphere has little effect on the fast mode signal and the magnetic signal recorded at the ground is expected to be similar to that recorded just above the ionosphere in the magnetosphere. Thus, if the ionosphere was non inductive the magnetic field on the ground would be aligned in the same way as the transverse poloidal component of the magnetospheric wave field. However, Yoshikawa and Itonaga (2000) showed that inductive ionosphere alters the nature of reflection and mode conversion of MHD waves.

Recently, Sciffer et al. (2005) modelled the propagation of ULF wave fields from the Earth's magnetosphere through the ionosphere, atmosphere and into ground using one dimensional computational model. They observed that for a typical ULF wave scale sizes, a 90^0 rotation of the wave polarization azimuth from the magnetosphere to the ground occurs at high latitudes and not always occurring at lower latitudes. They showed that the degree to which the wave polarization azimuth rotates critically depends on the properties of the compressional ULF wave mode. Another effect of the ionosphere on these waves is smoothing of the amplitude and phase variation, that is, short scale variations less than the height of the ionosphere are strongly attenuated on the ground. The dynamic of ionospheric currents that transmit or reflect the incident wave has the property of a low pass filter effect which cuts off higher spectral frequencies.

2.7 Geomagnetic pulsations

Geomagnetic pulsations are the magnetic signature of ULF waves, which are naturally occurring magnetohydrodynamic (MHD) waves in the Earth's magnetosphere. They are sinusoidal oscil-

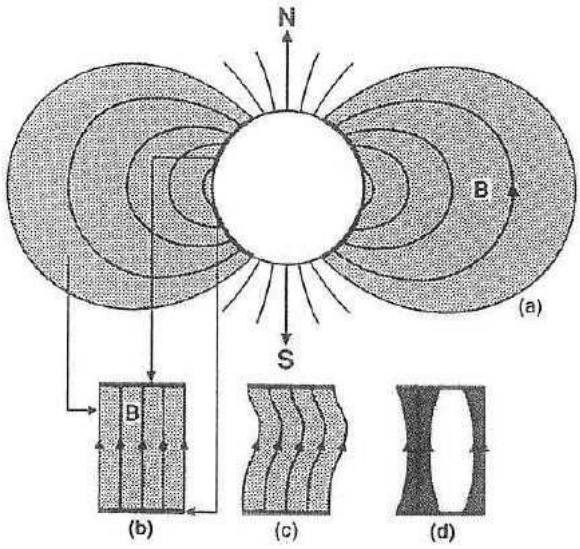

Figure 2.7: *The box model of the magnetosphere suggested by Kivelson and Southwood (1985, 1986). Dipole field lines in Figure a are relaxed in the box model Figure b. The perturbation of field and plasma in a shear Alfvén wave and in a fast compressional wave are shown* c *and* d. *The density of shading illustrates increases and decreases in the plasma density. (Adopted from Kivelson (1995))*

lations of the Earth's magnetic field and were reported first from ground observations (Stewart, 1861). It was only after the theory of electromagnetic wave propagation through a conducting fluid by Alfvén (1942), that Stewart's observation could be better explained according to the current understanding of ULF waves.

During the 1950s it was proposed that the oscillations observed on the ground with long but regular periods may be the result of standing Alfvén waves being excited on geomagnetic field lines (Dungey, 1954). These oscillations today have become known as geomagnetic pulsations. Dungey proposed that the pulsations were caused by waves standing along magnetic field lines and reflected at the ionospheres at the two ends. This behaviour can be depicted by the box model of Kivelson and Southwood (1985, 1986) shown in Figure 2.7. In this figure, the high latitude ionosphere forms boundaries at the ends of field lines and the near equatorial ionosphere serves as an inner boundary and the magnetopause as an outer boundary. The principle of the box model is the replacement of the dipole geomagnetic field with a uniform field, thus treating it as a straightened geomagnetic field. The field lines in Figure 2.7a have been straightened, bounded by the off-equatorial ionosphere at the top and bottom in Figure 2.7b to form a "box model" of the magnetosphere. The waves incident on the ionosphere will be reflected or transmitted depending on the ionospheric conductivity. The perturbation of field lines and plasma are shown in Figure 2.7c and d. The two figures show how the field line and plasma might be deformed if standing Alfvén waves or compressional waves perturb the magnetosphere. In

Continuous	**Period (s)**	**Frequency (mHz)**
Pc1	0.2-5	200-5000
Pc2	5-10	100-200
Pc3	10-45	22-100
Pc4	45-150	6.6-22
Pc5	150-600	1.6-6.6
Impulsive		
Pi1	1-40	25-1000
Pi2	40-150	6.6-25

Table 2.1: *Typical classification scheme for the ULF waves according to the period of pulsation (Jacobs et al., 1964).*

Figure 2.7c the density remains constant whereas in Figure 2.7d the density changes as the flux tube volume changes. The two primary modes of oscillation of a dipole field are transverse mode and fast mode (Southwood and Hughes, 1983). If pulsations are due to oscillations of standing waves, they must be observed simultaneously at magnetically conjugate points. In literature examples are available of simultaneous magnetic oscillations at conjugate points (Wilson and Sugiura, 1961; Nagata et al., 1963).

2.8 Pulsation classification

During the International Geophysical Year (IGY) of 1957/1958 it was established that pulsations detected by ground-based instruments differed in fundamental ways. A subcommittee of the International Association of Geomagnetism and Aeronomy (IAGA) suggested two main classes of pulsations based on their wave form and period (Jacobs et al., 1964). The first class includes pulsations of quasi-sinusoidal form and mainly continuous character with well defined spectral peaks. This class is treated as continuous pulsations and is denoted as Pc. This class is further broken down into 5 subclasses on the basis of predominant periods or frequencies (Saito, 1969). The second class includes irregular, impulsive pulsations and is denoted Pi. The Pi pulsations contain power at many different frequencies (Jacobs, 1970; Orr, 1973). The pulsation classes suggested by IAGA are shown in Table 2.1. An integer following prefixes “Pc” and “Pi” denotes the period and frequency range tabulated in the second and third columns respectively.

This work concentrates on the study of the Pc3 pulsation structures observed on the ground and along the CHAMP satellite trajectory in the ionosphere. This choice is informed by two facts:

- At latitudes considered in this thesis, Pc3 pulsations are mostly observed during local day time.

- Hence, directly comparing satellite and ground data sets provides an opportunity for testing MHD theoretical predictions by investigating the pulsation structure observed.

The continuous pulsations such as Pc3 are mainly thought to be the resonances of either geomagnetic field lines with ends fixed on the conjugate ionospheres or of cavities in the magnetosphere (Dungey, 1954, 1964). The resonance mechanism follows three steps: the source wave is excited at or near the dayside magnetopause/bow shock, it propagates into the magnetosphere as a fast-mode magnetosonic wave, and the latter couples into the local standing Alfvén wave (Southwood, 1974). The treatment of pulsations as harmonics of Alfvén waves follows suggestions (Sugiura and Wilson, 1964) that field lines or shells oscillate independently from each other in a manner similar to that of resonant waves on a vibrating string.

2.9 Solar wind as a source and control of ULF waves

The relationship between Pc3-4 pulsations and the solar wind parameters were obtained by comparing Pc3-4 periods with solar wind parameters (Gringauz et al., 1970) measured on Venus 2 (1965), Venus 4 (1967) and Venus 5 and 6 (1969). The purpose of this section is to describe the main source of Pc3 pulsations and highlight their propagation path in the magnetosphere. Extensive theoretical and observational studies of ULF pulsations available in the literature inform and drastically improve our knowledge and understanding of pulsation source mechanisms.

Observational evidence suggesting that these geomagnetic pulsation are controlled, if not actually generated by the solar wind, has been mounting in the literature. This supported the formulation of the problem of diagnosing the magnetosphere by means of ULF waves (Troitskaya, 1961; Troitskaya and Melnikova, 1959; Troitskaya et al., 1962). Upstream waves associated with the quasi-parallel shock have been linked to both compressional Pc3 and toroidal multi-harmonic field line resonance (Anderson, 1994). The ULF upstream waves with a typical period of 20-30 s are large amplitude waves found almost everywhere in the Earth foreshock region (Greenstadt et al., 1968) generated by ion-cyclotron resonant instability caused by ions backstreaming along the magnetic field to generate Alfvén waves in the interplanetary medium (Fairfield, 1969; Thomsen, 1985). The ion cyclotron waves are subsequently convected downstream across the bowshock to the magnetopause and couple energy into magnetosphere (Barnes, 1970; Greenstadt et al., 1968; Le and Russell, 1996).

The ULF waves observed in the upstream region from the Earth's bow shock, appear with different wave forms depending on their locations in the foreshock: nearly monochromatic transverse waves near the foreshock boundary, compressional waves with steepening edges deep into the foreshock, and very irregular nonlinear waves near the bow shock (Le and Russell,

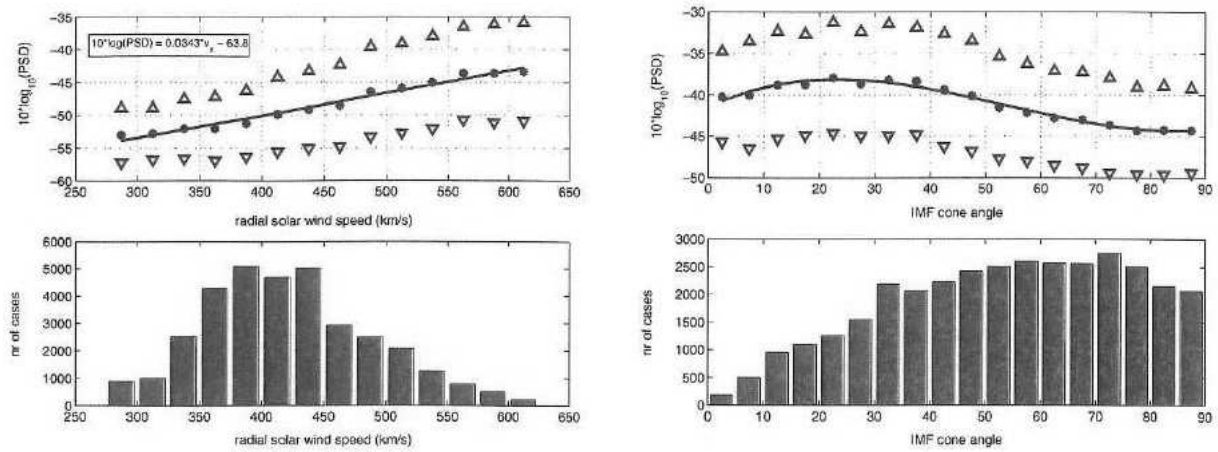

(a) (b)

Figure 2.8: *a) SW speed control of UW mean compressional power. b) IMF cone angle control of UW compressional power. (Adopted from Heilig et al. (2007).)*

1994, 1996).

2.9.1 Upstream wave path

Engebretson et al. (1991) reviewed models of upstream wave entry into the Earth's magnetosphere, focusing on the direct entry of wave energy across the magnetopause, followed by mode conversion to generate resonant transverse pulsations. The Earth's foreshock is the region upstream from the bow shock where the interplanetary magnetic field intersects the bow shock and is characterised by backstreaming electrons, ions and associated waves (Le and Russell, 1994). ULF waves generated in the region upstream of the bow shock are convected downstream by the solar wind into the magnetosheath. When the IMF cone angle is small, waves in the subsolar upstream region are carried to the magnetopause boundary. The magnetopause responds to these pressure fluctuations and transfers wave energy into the dayside magnetosphere where they can excite field line resonances. Upstream waves have a broad-band spectrum, and when propagating through the magnetosphere, different parts of this spectrum correspond to local field line resonances and excite them (Varga, 1980). It is generally agreed that upstream waves are the major source for dayside Pc3 and 4 magnetic pulsations (Le and Russell, 1994). However, the wave structure observed may be affected by cavity modes (Menk et al., 2000).

2.9.2 The observable relationship between the upstream wave and Pc3-4 pulsations

The frequency of UWs is proportional to the magnitude of the interplanetary magnetic field (Troitskaya et al., 1971) and the UW occurrence rate is controlled by IMF direction, namely the

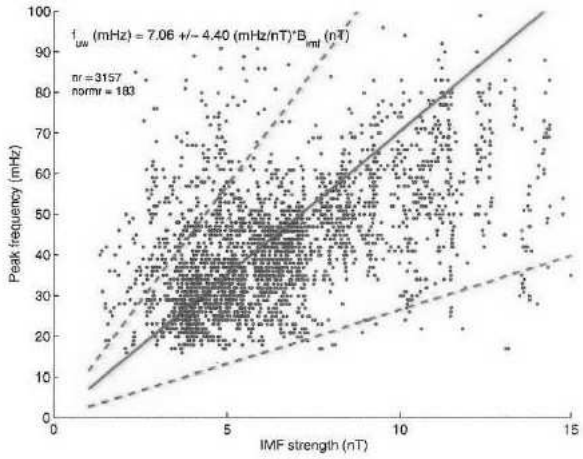

Figure 2.9: *The relationship between UW peak frequency and the IMF strength. (Adopted from Heilig et al. (2007)).*

IMF cone angle (Bolshakova, 1966; Bolshakova and Troitskaya, 1968; Greenstadt and Olson, 1977; Russell et al., 1983). A small cone angle creates a favourable condition for the generation of upstream waves (Le and Russell, 1996). The relationship between IMF strength and wave frequency is explained by linear theory (Fairfield, 1969) since the majority of the waves are believed to be generated by resonant interactions coming from the bow shock (Barnes, 1970; Gary et al., 1981). The dominant frequency of Pc3-4 pulsations observed on the ground was shown to be controlled by the strength of the IMF (Green et al., 1983). The relationship between upstream wave frequency and the IMF was suggested as:

$$f_{UW}(mHz) = 6\ IMF(nT). \tag{2.27}$$

Heilig et al. (2007) used magnetic field measurements from the CHAMP satellite to investigate upstream waves (UW) in the topside ionosphere and made suggestions concerning the entry mechanism of UW's from the foreshock region into the magnetosphere. They compared their comprehensive observations of UW in the topside ionosphere observed by CHAMP with pulsations observed on the ground. The mean signal power of compressional wave activity in CHAMP data for the group of waves confined to the dayside (06:00-18:00 LT) was shown to be highest over the equator and lowest around 40^0 latitude.

Heilig et al. (2007) tested the effect of solar wind speed, interplanetary magnetic field (IMF) and cone angle on the UWs, since these parameters are known to control the generation of UWs (Saito, 1964; Troitskaya et al., 1971). They confirmed that high solar wind speed provided higher power input to UWs and that a smaller cone angle creates a favourable condition for the generation of upstream waves as shown in Figures 2.8(a) and 2.8(b) respectively; also

that the frequency of the UWs is proportional to the IMF strength (see Figure 2.9). They also provided the first observational verification of the Doppler shift of the UW frequency relative to the satellite frame, caused by the super Alfvénic solar wind.

2.10 Field line resonances (FLR)

The ULF waves observed at ground level are not usually the same waves that enter the magnetosphere from the source (solar wind). The wave energy is transformed and amplified by processes in the magnetosphere, e.g. field line resonances and other cavity resonances (McPherron, 2005). In this section the concept of MHD field line resonance attributed to a response of the magnetosphere to solar wind impacting the magnetopause (Ruohoniemi et al., 1991), is introduced. FLR theory explains how the perturbation energy of a monochromatic compressional wave couples to and excites the standing shear Alfvén mode on the resonant field line. We focus our discussion on the theories of Southwood (1974) and Chen and Hasegawa (1974) which successfully explain the typical features of ULF waves, i.e. that the waves are harmonically structured and azimuthally polarised. These structures have been effectively resolved by Walker et al. (1978, 1979) using the STARE radar. Their theories are widely accepted. Their theories assume that the solar wind induces a flow of plasma in the magnetosheath or low-latitude boundary layer that leads to velocity shears and the growth of Kelvin-Helmholtz instabilities (KHI) on the magnetopause. In the magnetosphere these instabilities induce almost circularly polarised hydromagnetic waves (Samson et al., 1971) and result in waves that propagate away from the sun along the magnetospheric flanks (Ruohoniemi et al., 1991). Energy from the KHI propagates into the magnetosphere as compressional Alfvén waves until the increasing Alfvén velocity leads to a turning point for the waves and part of the energy is reflected (Kivelson and Southwood, 1986). On the Earthside of the turning point the wave is evanescent, but the coupling of the compressional and shear Alfvén wave due to the dipole geometry can lead to the resonance on the field line for which the wave frequency equals the natural frequency of oscillation. The resonance are set up by hydromagnetic waves confined within cavities formed by extremes in the Alfvén velocity (Samson et al., 1971). Some of the obvious boundaries mentioned in the earlier studies are the ionosphere, the plasmapause, and the magnetopause, with the ionosphere and the inner dipole field of the Earth forming the most symmetric activity.

The two characteristic modes of resonance in a dipole geomagnetic field line which can be inferred from the transverse magnetic field components of the wave equations of Dungey (1954) are the toroidal and poloidal modes. Dungey (1954) developed the wave equations for the dipole field geometry. What Dungey did was to derive hydromagnetic wave equations in general axisymmetric field geometry (a dipole being a special case) and showed that these equations

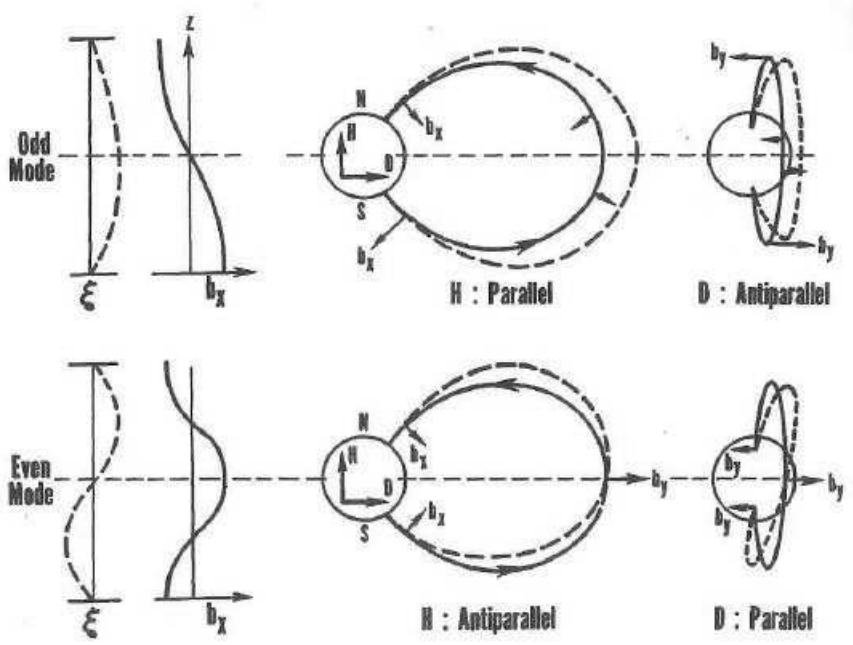

Figure 2.10: *Standing oscillations in a dipole field approximating stretched strings (left panel). A schematic illustration of dipole oscillation in two orthogonal directions: radial (middle panel) and azimuthal (right panel). The oscillation may consist of odd (top row) or even (bottom row) harmonics. In the diagram the field displacement is denoted by* ξ*, and* b_x *and* b_y *are the components of the magnetic perturbation. The field lines are anchored at the ends (ionosphere) and are nodes of field line displacement, but antinodes of the magnetic perturbation (from McPherron, 2005).*

decouple in two limits. Hughes (1994) reviewed Dungey's equations and briefly discussed the two limits that lead to the decoupling of the transverse components. For the axisymmetric wave with finite azimuthal wave number (m = 0), the toroidal and poloidal mode decouple. For this limit Dungey's equations describe a mode where the electric field is pure radial and the magnetic and velocity perturbations are azimuthal. Magnetic L-shells (shells containing only magnetic field lines with similar L values) decouple and each shell oscillates azimuthally independently of all others (Hughes, 1994). This is the toroidal mode. For an infinite azimuthal wave number (m$\rightarrow \infty$) Dungey's equation describes a mode in which the electric field is azimuthal and the velocity and magnetic perturbations are contained in the meridian plane. In this scenario the oscillations of each meridian plane decouple, producing a poloidal mode oscillations (Hughes, 1994). The axially symmetric case corresponds to a fast mode with magnetic oscillations in a meridian plane and represents alternate symmetric compressions and expansion of the entire magnetosphere. The nature of the resonance of the two modes are illustrated in Figure 2.10. The behaviour of the dipole field line resonances is analogous to the waves of a violin string (Bellan, 1996). The toroidal mode is a displacement in the azimuthal direction creating azimuthal magnetic perturbations as shown in the right-hand panel of Figure 2.10.

The poloidal mode is a radial displacement with radial magnetic perturbations as shown in the middle panel of the Figure 2.10.

The field line resonance theory explains why waves observed at a single station are quasi-sinusoidal and have a well-defined frequency. This is because field line resonances can be imagined to occur as modes of Standing Alfvén waves which are excited in the entire magnetosphere on geomagnetic field lines. Periodic disturbances of frequency ω_{ex} arriving at the magnetopause may set the field line with a resonant frequency $\omega_{res} = \omega_{ex}$ into oscillation (Baumjohann and Treumann, 1997). A magnetic field line in an inhomogeneous plasma becomes resonant when the condition $\omega = k_{\|} V_A$ is satisfied on the field line. The ω is the angular frequency perturbation, $k_{\|}$ is the component of the wave number parallel to the magnetic field and V_A is the local Alfvén velocity on the field line (Bellan, 1996).

2.10.1 L-dependence of FLR frequency

For a standing wave in the shear or Alfvén mode, the pulsation period is governed principally by the Alfvén velocity distribution along the field line, which in turn is a function of the magnetic field intensity and the ion mass density distribution (Poulter et al., 1988). At the zeroth order the field line eigenfrequency equals the inverse travel time of Alfvén waves along the magnetic field line between the northern and southern ionosphere. The field line resonance frequency is expressed as $f_{FLR} = \left(\int \frac{ds}{V_A}\right)^{-1}$ (Fraser et al., 1988; Maeda et al., 2009). To find the mathematical expression of the FLR frequency as function of L-shells values; let us recall that (in the equatorial plane) the resonance occurs beyond the turning point where:

$$\omega^2 = k_z V_A^2 \tag{2.28}$$

where k_z is the wave vector parallel (in local coordinates) to the magnetic field, with λ_z the corresponding wave length expressed as:

$$k_z = \frac{2\pi}{\lambda_z} \tag{2.29}$$

The resonance occurs on the field line with length

$$l = \frac{n\lambda_z}{2} \quad n = 1, 2, 3, ... \tag{2.30}$$

From equation 2.29 and 2.30 the wave vector can be expressed as a function of field line length

$$k_z = \frac{\pi}{l} \tag{2.31}$$

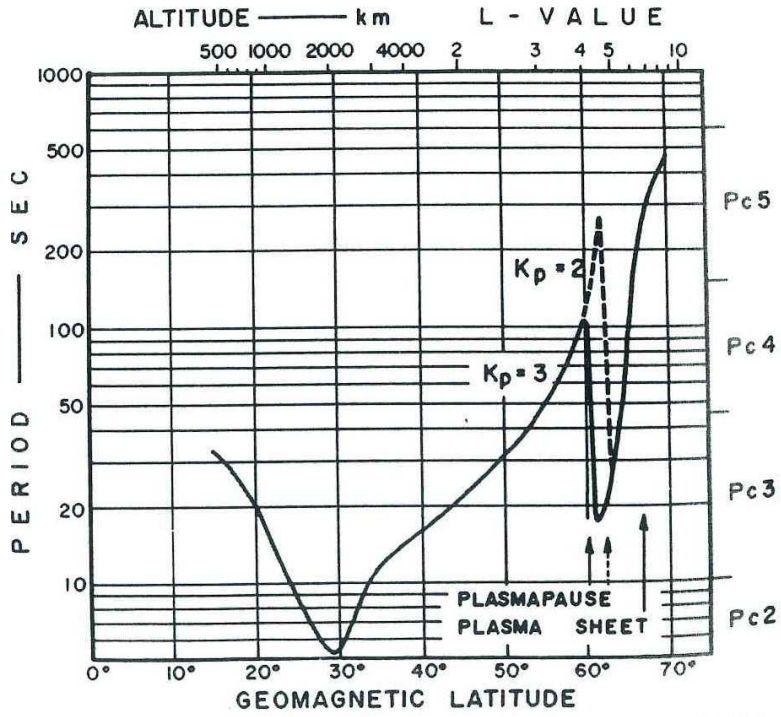

Figure 2.11: *The fundamental toroidal resonant period calculated by Nishida (1978).*

The expression 2.31 is substituted in equation 2.28 to obtain:

$$\omega^2 = \frac{\pi^2 V_A^2}{l^2} \tag{2.32}$$

The FLR frequency in hertz is obtainable from 2.32:

$$f_{FLR} = \sqrt{\frac{V_A^2}{4l^2}} \tag{2.33}$$

Therefore, the field line resonance frequency depends on the background magnetic field strength, the field line length and the plasma density along the geomagnetic field line. Consideration of the radial Alfvén wave velocity profile can provide insight into the resonant wave period in the magnetosphere. The fundamental period for the toroidal mode oscillation calculated by Nishida (1978) clearly illustrates the dependence of FLR frequency on the L-shell (see Figure 2.11). Figure 2.11 illustrates the resonant frequencies decreasing with the latitudes except near the plasmapause. FLR occurs with a wide range of frequencies in different parts of the magnetosphere and is excited by a number of different sources. This was confirmed by ULF observations over decades by stations at high, mid- and low-latitudes. Several proposed drivers of FLR include the Kelvin-Helmholtz instability at the magnetopause boundary (Samson et al., 1971; Southwood, 1974), magnetospheric global cavity modes stimulated by solar wind disturbances (Kivelson and Southwood, 1985; Allan et al., 1985), wave guide modes on the

magnetospheric flanks (Walker et al., 1992; Wright, 1994) and the upstream waves generated in the Earth's foreshock (Le and Russell, 1994).

2.10.2 Field line resonance at high latitudes

At higher latitudes the field lines are longer and the resonant frequency moves into the lower frequency (1-10 mHz) Pc5 range. Throughout local daytime, there is a largely continuous Pc5 band observed in the high latitude regions which is attributed to field line resonances. A widely accepted source of the high latitude Pc5 pulsation is a surface wave activity at the magnetopause, which is a possible consequence of Kelvin-Helmholtz instabilities. The KHI leads to the generation of compressional fast-mode waves that propagate in the magnetosphere across the geomagnetic field lines in the magnetosphere. The compressional waves can excite shear Alfvén waves at the location where the wave frequency matches the eigenfrequency of the local magnetic field, exciting the resonance. The proposed mechanism, namely KHI, cannot explain discrete FLR occurring simultaneously at different latitudes. These have been attributed to either the cavity or wave guide modes in the region between the magnetosphere and a reflection level within it (Kivelson and Southwood, 1985; Stephenson and Walker, 2010). A cavity model model focuses on the idea of the magnetosphere acting as a resonant cavity. Abrupt changes in the solar wind dynamic pressure could excite compressional waves matching the frequencies of the cavity. This compressional wave then excites a field line resonance in same way as in the KHI theory. The cavity picture was later developed to wave guide description (Samson et al., 1992; Walker, 2002). Recently it has been suggested that Pc5 pulsations may be driven by MHD waves in the solar wind (Walker, 2002) and that coherent oscillations in the solar wind give rise to Pc5 field line resonances within the magnetosphere at the same frequency (Stephenson and Walker, 2010).

2.10.3 The structure of field line resonance at low latitudes

Inside the plasmasphere FLRs are excited in the Pc3-4 band. The much shorter field line length and the larger values of Alfvén speed along the field line leads to shorter Pc3-4 periods. The compressional waves can propagate from outside the plasmapause into lower latitudes and can couple into fast magnetosonic waves (Yumoto et al., 1985). Waters (2000) reviewed the excitation of FLR observed at low latitudes based on the work of Russian scientists in the early 1970s (e.g. Troitskaya et al. 1971) and the subsequent studies of the dependence of Pc3 activity on solar wind parameters by Odera (1986) and Le and Russel (1996). He concluded that compressional waves originating upstream from the Earth are the main source of low latitude Pc3-4 magnetic pulsations. The generally accepted understanding is that fast mode energy generated as ion cyclotron waves in the bow shock region, passes through the magnetopause

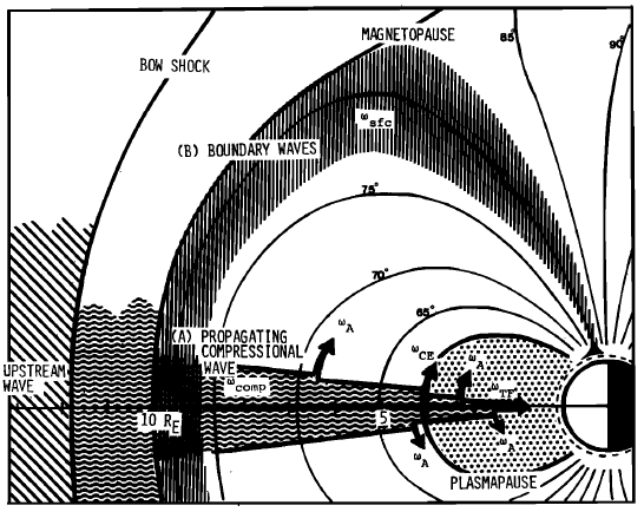

Figure 2.12: *Propagation mechanisms of daytime Pc3-4 pulsations in the magnetosphere. Propagating compressional waves (A) in the Pc 3 frequency band transmitted from the upstream region in the Earth's foreshock can couple with various hydromagnetic waves at various locations in the magnetosphere, i.e., a high-harmonic standing oscillation (ω_A) of a local field line in the outer magnetosphere, a fundamental eigenoscillation (ω_A) in the plasma trough, high-harmonic surface wave (ω_{CE}) on the plasmapause, a trapped oscillation (ω_{TF}) of a fast magnetosonic wave, and fundamental and high-harmonic standing oscillations (ω_A) in the plasmasphere (adopted from Yumoto et al., (1985)).*

with little alteration in spectra, traverses the plasmatrough and into the plasmasphere, and reaches low latitudes where it can excite field line resonances, as illustrated in Figure 2.12 (adopted from Yumoto et al., (1985)). This thesis is concerned with Pc3 frequencies generated by upstream waves.

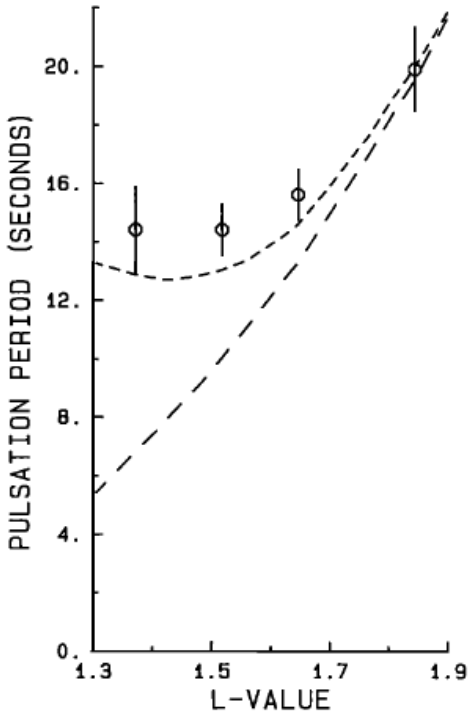

Figure 2.13: *The mean (circles) and standard deviation (error bars) of the dominant pulsations periods of the H component observed at the stations SAA (L=1.84), AUG (L=1.64), MAR (L=1.52) and TSU (L=1.37). The short dashed line shows the periods computed using a plasma model containing both O^+ and H^+ as functions of L-value. The long dashed line shows the periods computed with the same H^+ distribution, but with O^+ excluded (adopted from Hattingh and Sutcliffe (1987)).*

The modelling of the pulsation eigenperiods at low latitudes has demonstrated the importance and influence of plasma distribution along resonating field lines in computing realistic Pc3 eigenperiods. A comparison of computed and observed eigenperiods at low latitudes led to the conclusion that the inclusion of the F region O^+ in the plasma distribution noticeably affects the calculated ULF eigenperiods (Hattingh and Sutcliffe, 1987). This effect decreases with increasing L-value (see Figure 2.13). The observed periods in Figure 2.13 demonstrate the importance of including O^+ in the plasma model if realistic periods are to be calculated at low latitudes.

2.11 Field line resonances and wave guide mode at low latitudes

Menk et al. (2000) utilized a ground station array to investigate the properties of low latitude Pc3 pulsations. For their work they used a ground magnetometer array in eastern Australia

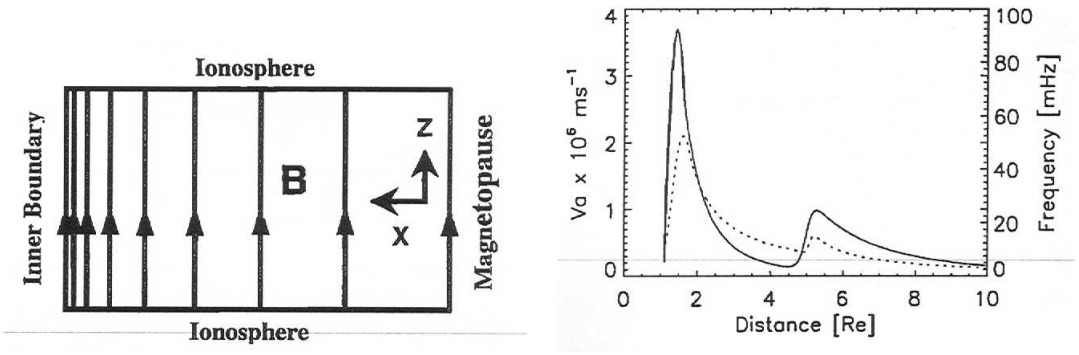

(a) (b)

Figure 2.14: *a) 1-D cavity model of the magnetosphere. b) The Alfvén velocity (solid line) and FLR frequency variation with x (dotted line) used in the 1-D model (Waters et al., 2000).*

spanning L = 1.3 to 2.0 to study the dynamics of field line resonances (FLR), e.g. the variation in Pc3-4 power with latitude, the nature and low-latitude limit of FLRs, and properties of spectral components below the local resonant frequency. They found that the resonant frequency increases with decreasing latitude up to L $\sim$ 1.6 and then decreases at lower latitudes as a result of mass loading on field line eigenfrequencies due to the effect of ionospheric heavy ions at low altitudes (Hattingh and Sutcliffe, 1987). Regarding the source, their results were consistent either with the modulation of the incoming fast-mode waves or the existence of cavity or waveguide modes. The fast mode waves or wave guide modes drive discrete forced oscillations of low-latitude field lines across a range of frequencies and couple with the local field line resonance where the frequencies match.

There is indirect evidence of the existence of cavity resonances and their importance in determining the properties of ground ULF waves (Waters et al., 2000). Using the work by Waters et al. (2000) who solved a 1-D cavity model of the magnetosphere, McPherron (2005) illustrated the nature of cavity resonances. Waters's model is summarised in Figure 2.14. In Figure 2.14(a) dipole field lines are straightened and fixed in conducting ionosphere at the top and bottom of the box as described in the box model of the magnetosphere. The characteristic features of the model includes the inner boundary at 1.1 R_E and input wave spectrum at the outer boundary (10 R_E) that varies as the inverse of frequency ($1/f$). In addition the model invoked the use of realistic Alfvén velocity that depends on the radial coordinate shown by the solid profile in Figure 2.14(b). The dashed curve in Figure 2.14(b) denotes the field line resonance frequency associated with this profile.

In this 1-D box model it was assumed that waves will stand both along field field lines and radially, but propagate azimuthally. The circular structure of the Earth's field was simulated

by choosing the azimuthal wavelength of the propagating wave so that it increases proportionally with radial distance increasing *i.e.* from left to right. The model assumed that cavity modes couple energy into field line resonances, and that field line resonances are dampened by the conductivity of the ionosphere (e.g. Waters et al., 2000). This model could successfully reproduce important features of low-latitude ULF spectra observed by Menk et al. (2000), an indication that the interaction between waveguide and field line resonance modes is important in understanding low-latitude data.

2.12 Summary

In this chapter the reader was introduced to the concepts of the magnetosphere and MHD waves. We described a closed model of the magnetosphere and a more realistic model of the magnetosphere called the open magnetosphere where the interplanetary and terrestrial field lines connect through the boundary, a process called magnetic reconnection. We derived an MHD wave equation from Maxwell's equation in the low frequency limit. This is for a frequency lower than the natural frequencies of the plasma such as the plasma frequency and ion gyrofrequency. We also derived the dispersion relations of the two MHD waves (i.e. fast and transverse Alfvén waves) found in a cold plasma. Ionospheric currents, e.g. Hall and Pedersen currents, cause modifications to MHD waves as they are transmitted through ionosphere and atmosphere to the ground. A brief review of the effects of ionospheric currents on the MHD wave was given in this chapter.

We also introduced the concept of geomagnetic pulsations which are rapid variations in the geomagnetic field. These pulsations can either be continuous (they are then called Pc pulsations) or irregular (called Pi pulsations). This work concentrates on the study of the third class of continuous pulsation, termed Pc3, characterised by a period ranging from 10-45 seconds. This type of pulsation is observed mostly during local daytime at latitudes considered in this thesis. We reviewed the effect of the solar wind and its parameters as the control mechanism of the generation of upstream waves. The upstream waves are believed to be the ultimate source of Pc3 waves. The relationship between the solar wind parameters and upstream wave is summarised as follows:

- A small cone angle favours the generation of upstream waves.
- High solar wind speeds provide higher input to upstream waves.
- The frequency of upstream waves is proportional to the strength of the interplanetary magnetic field.

The above-mentioned relationships were recently tested and confirmed by Heilig et al. (2007) using magnetic field measurements of unprecedented accuracy from the CHAMP satellite.

In the next chapter we will briefly describe the CHAMP mission which provides magnetic field data used throughout this work in conjunction with ground measured data. The magnetometers on board CHAMP and on the Earth surface at given locations are described.

Chapter 3

Data and Preferred Laboratory for Low Latitude Pc3 Studies

3.1 Introduction

An important aspect of magnetospheric studies is the accumulation of data. The analysis of the accumulated data improves our understanding of the physical system responsible for the MHD waves observed in the magnetosphere. In this work observations from the Challenging Minisatellite Payload (CHAMP) satellite are compared to observations recorded at the Earth's surface. This chapter is therefore dedicated to:

- a brief discussion of the CHAMP mission which provides unprecedentedly accurate magnetic field data.
- a discussion of the magnetometers on board CHAMP and on the Earth's surface at given locations.

The CHAMP data used in this study is rotated into a geomagnetic field-aligned coordinate system. This study employs the use of the background magnetic field and a low-pass filter to compute the angles required for rotating data into field-aligned coordinates. Although our studies focus on low latitude Pc3's, the literature informs of Pc3 pulsations observed in the Earth's polar cusp regions near local magnetic noon (Engebretson et al., 1986, 1991). It will be shown that the preferred laboratory for low latitude Pc3 geomagnetic pulsations studies excludes high current regions. In order to establish our laboratory we experimented with CHAMP data to establish latitudes where the satellite registers high currents as a consequence of the auroral electrojets or field-aligned currents (FAC).

3.2 The CHAMP mission

The Challenging Minisatellite Payload (CHAMP) mission is one of the important missions for studying aspects of the magnetosphere such as gravity and the geomagnetic field. CHAMP is the first satellite after the US's MAGSAT and Denmark's Ørsted satellites dedicated to gravity and magnetic field missions. It was initiated by the German Space Agency and GFZ scientists (Reigber et al., 1999, 2002) as a small satellite mission with science instrumentation that would allow simultaneous gravity and magnetic field measurements and also drastically improve gravity and magnetic field modelling (see also GFZ website:http://www-app2.gfz-potsdam.de/pb1/op/champ/).

The Low Earth Orbiting (LEO) CHAMP satellite was launched on 15 July 2000 into a near-polar circular orbit at an initial altitude of 454 km. It was launched with a 5 year mission plan but it is currently still running. The low altitude orbit supports the spatial resolution of the geopotential field whereas the long mission duration helps to recover temporal field variations (e.g. Reigber et al. 2002). The instrument of interest for this study on board the CHAMP

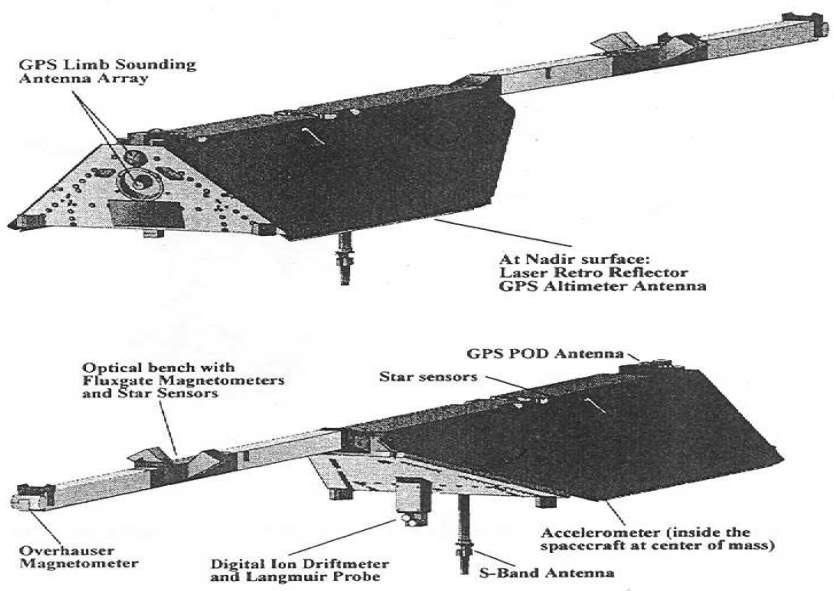

Figure 3.1: *Sketch of the CHAMP satellite and payload accommodation (adopted from Reigber et al. 2002)*

satellite is the fluxgate magnetometer. CHAMP magnetometry comprises the high performance Fluxgate magnetometer with the Overhauser scalar magnetometer serving as magnetic reference. In the satellite sketched in Figure 3.1 high quality magnetometers and star cameras are placed on the long boom facing flight direction to avoid magnetic effects. The satellite is equipped with these magnetometers to accomplish the mission objective of studying the geomagnetic field. The Fluxgate magnetometer measures the three components of the ambient

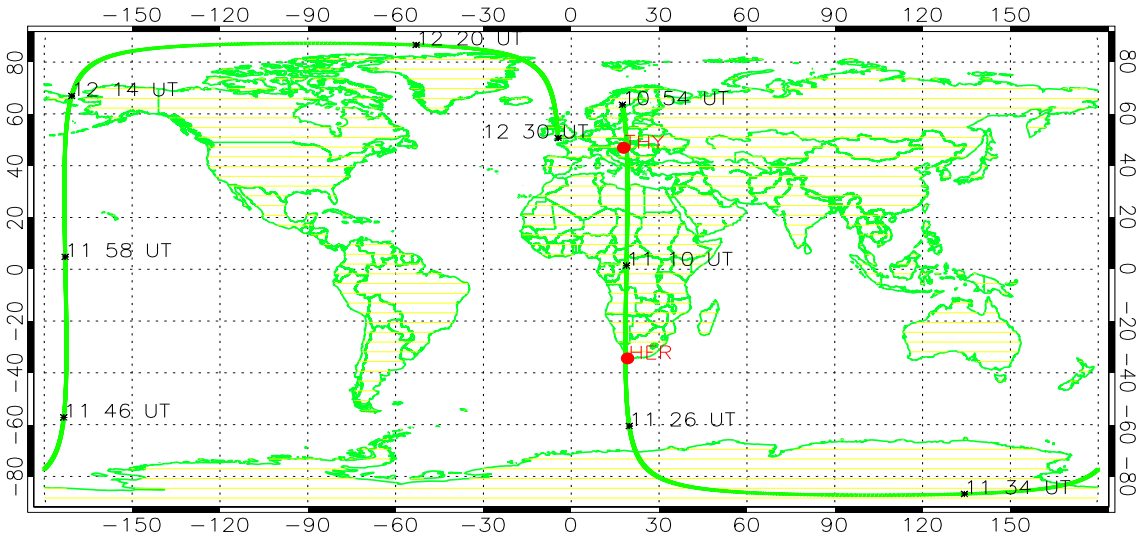

Figure 3.2: *IDL generated map showing the conjugate magnetometer stations and the satellite ground track as the satellite orbits the Earth*

geomagnetic field in the instrument frame. A star camera determines the attitude of the assembly with respect to a stellar frame. The specific primary objectives of the CHAMP mission as described by Reigber et al. (2002) are also available on the GFZ website and include:

- mapping both the gravitational geopotential by the analysis of the observed orbit perturbations,
- mapping the magnetic geopotential via on-board magnetometry, and
- performing atmospheric and ionospheric profiling using GPS radio occultation measurements.

3.2.1 CHAMP orbit characteristics

CHAMP was launched at a maximum inclination angle from the Plesetsk cosmodrome, Russia. The satellite was launched into a near-circular orbit as that provides the advantage of getting a homogeneous and complete global coverage of the Earth's sphere. The magnetometer measurements are important for resolving the gravitational field and magnetic geopotential. The advantage of an 87^0 inclination angle vs a dawn-dusk sun-synchronous orbit is the local time variation of the satellite's ground track. Figure 3.2 shows an IDL-generated map with the locations of conjugate reference ground stations which provide ground magnetic field measurements. The ground stations Hermanus and Tihany are labelled as HER and THY respectively, using their INTERMAGNET codes. The line plotted over the map indicates a 96 minute satellite ground track as the satellite orbits the Earth. The universal time is indicated along the path for a specific orbit. The figure suggests that CHAMP orbits the Earth every 90 minutes and

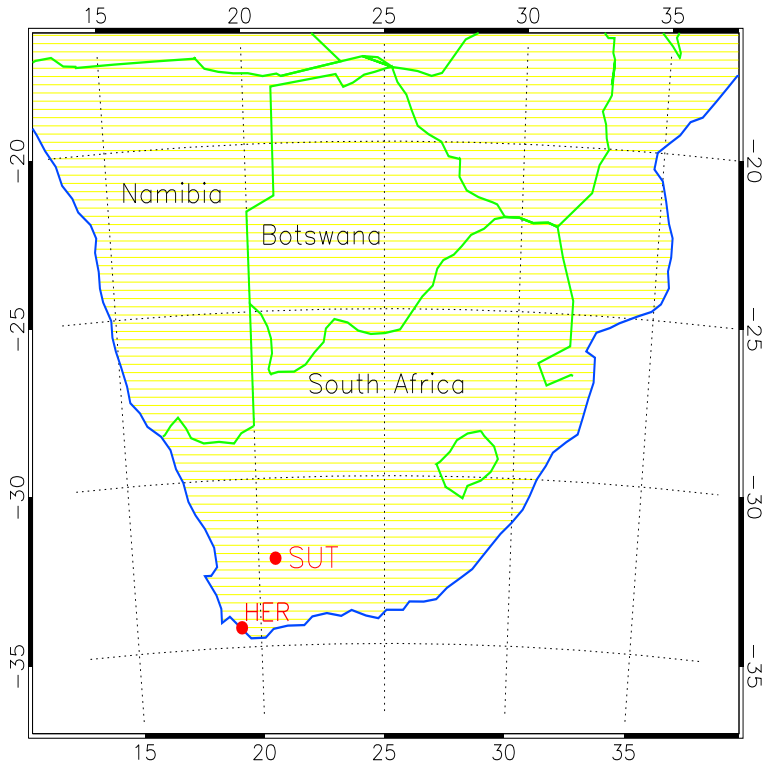

Figure 3.3: *Current geomagnetic pulsation recording stations, Hermanus (HER) and Sutherland (SUT), in South Africa operated by Hermanus Magnetic Observatory (HMO).*

shifts longitude by 23.5^0 west for each subsequent orbit. Thus, almost full coverage of the Earth occurs every 24 hours.

3.3 Magnetometer instrumentation and data

A magnetometer is a scientific instrument used to measure the strength and/or direction of the magnetic field in the vicinity of the instrument (en.wikipedia.org/wiki/Magnetometer). Magnetometers can be divided into two basic types, namely scalar and vector magnetometers. The scalar magnetometer measures the total strength of the magnetic field to which it is subjected, whereas the vector magnetometer has the capability of measuring the components of the magnetic field in a particular direction. In this work vector magnetometer data is preferred over scalar data.

A 3-vector component magnetometer on board CHAMP measures the strength of the Earth's magnetic field using the combination of Fluxgate magnetometers and the star camera and the Overhauser scalar magnetometer serving as a magnetic reference. The data provided in the FGM reference sensor frame and the data transformed into the North-East-Center (product identifier CH-ME-2-FGM-NEC) coordinate system are available to the public through the ISDC

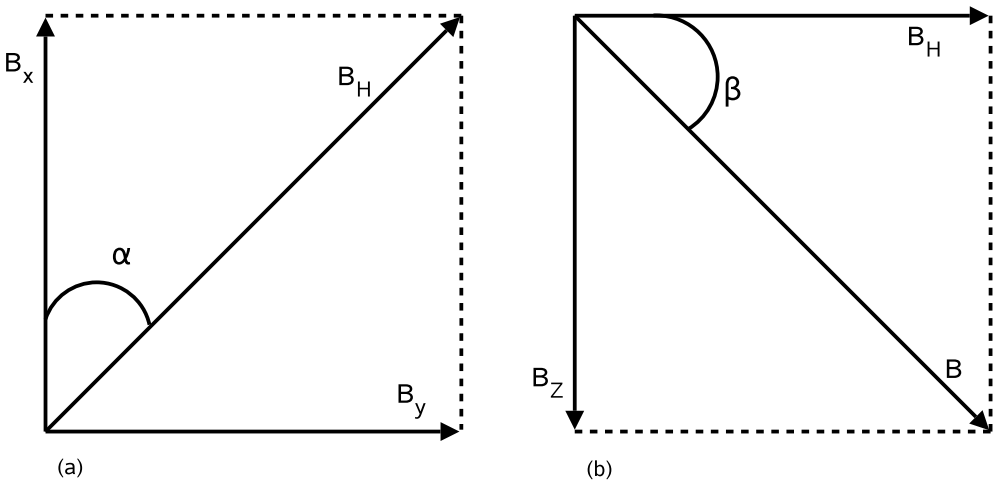

Figure 3.4: *The computation of the resultant magnetic field and the angle of rotation*

data center (http://isdc.gfz-potsdam.de/CHAMP). The CHAMP data used in this study is the preprocessed (level 2) Fluxgate vector magnetometer data (product identifier CH-ME-2-FGM-FGM). The instrument samples data at a rate of 50 Hz at a resolution of 0.1 nT. However, in this work we used the standard processed data averaged to 1 Hz samples. The data in the sensor reference frame were used because the data transformed into the North-East-Center (NEC) coordinate system are contaminated by attitude noise and not entirely suitable for Pc3 studies.

In this work the satellite data is used in conjunction with data recorded at ground by equipment typically operated by magnetic observatories. Currently, two induction magnetometers for recording geomagnetic pulsations in South Africa are located at Hermanus (HER) (34° 25′ S, 19° 13′ E) and Sutherland (SUT) (32° 24′ S, 20° 40′ E). The station locations shown in Figure 3.3 are 220 km apart. The induction magnetometers at both stations sample the H-component (magnetic North-South) and D-component (magnetic East-West) data at 1 second intervals. At Sutherland there is an additional vertical (Z-component) sensor. The geomagnetic pulsation recording equipment consists of induction sensors (2m long metal rods wound with 100 000 turns of copper wire) and associated electronics. There is a scientific reason for placing the stations in pairs. The calculation of spectral difference in ULF amplitude and crossphase spectrum between closely spaced meridional ground stations is an efficient method to determine the eigenfrequency of geomagnetic field lines (Baransky et al., 1985; Waters et al., 1991a).

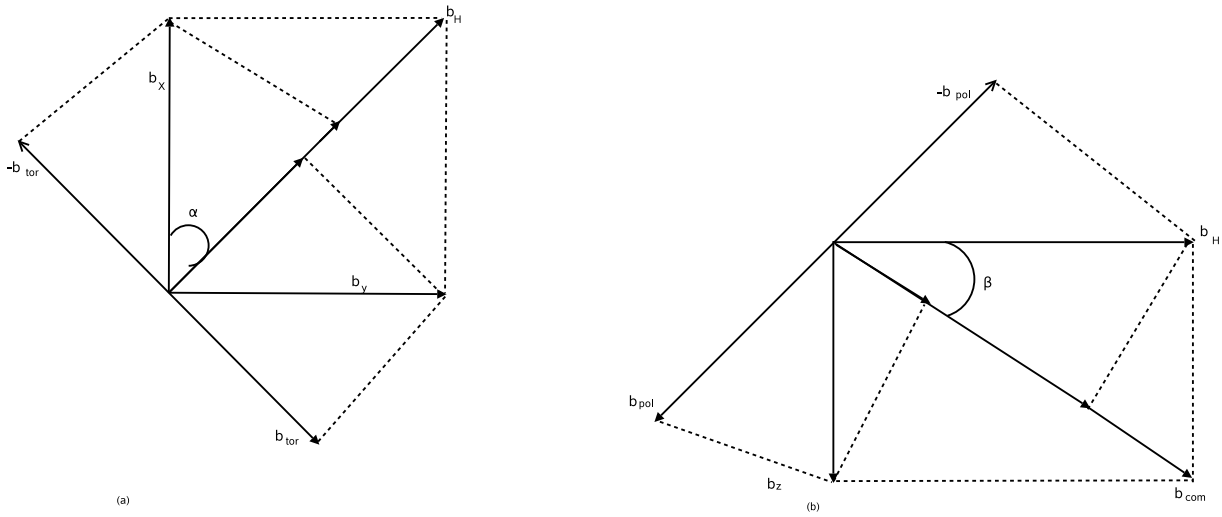

Figure 3.5: *The computation of the pulsation components i.e. toroidal (b_{tor}), compressional (b_{com}) and poloidal (b_{pol}).*

3.4 A field-aligned coordinate system

For geomagnetic pulsation studies it is desirable to use data oriented in a system well suited for studying wave phenomena. In this study the data are transformed into a geomagnetic field-aligned coordinate system. This system enables the separation of transverse and fast mode waves. This section discusses the procedure followed in this study to rotate CHAMP magnetic field components from the FGM coordinate system into the field-aligned coordinate system. In this coordinate system, the compressional component (B_{com}) is aligned with the ambient magnetic field **B** (positive northward), B_{tor} the toroidal component is transverse to **B** in the azimuthal direction (positive eastward) and the poloidal component (B_{pol}) is transverse to **B** in the magnetic meridian plane (positive inward). The first step is the determination of the orientation of the ambient background magnetic field. In order to do this the data are filtered through a low-pass filter that passes low frequency signals but attenuates the amplitude signals with frequencies higher than the cut-off frequency. The background field is used to compute the angles of rotation which in turn are used to compute pulsation magnetic field components.

It was established that a low pass filter cut-off of 0.8 mHz gives good results, basically representing a background field from which variations with periods shorter than 20 min have been removed. It is believed that this method will provide more accurate results than using a magnetic model such as POMME (Maus et al., 2005) which provides a long-term averaged background magnetic field. The low pass filtered data takes localised temporal and spatial variation into account (P. Sutcliffe, private communication).

With the aid of vector drawings in Figures 3.4 and 3.5 the background field is used to compute the angles required for rotation into field-aligned coordinates. In the FGM data set Z-axis (B_z) is the vertical component. The angles are computed for each data point in the time series (typical at 1-second intervals) because the position of CHAMP changes very rapidly with time. Shown in Figure 3.4a is the geometry used to compute the resultant magnetic field B_H of B_X and B_Y. The angle between B_H and the resultant B_X and B_Y, α, equivalent to declination in the horizontal plane is computed from:

$$tan\alpha = B_Y/B_X \tag{3.1}$$

$$\alpha = tan^{-1}(B_Y/B_X) \tag{3.2}$$

Figure 3.4b shows the computation of the total magnetic field B from the components B_H and B_Z in the vertical plane. The angle between B_H and resultant **B** of B_H and B_Z is computed as follows:

$$tan\beta = B_Z/B_H \tag{3.3}$$

$$= B_Z/({B_X}^2 + {B_Y}^2)^{1/2} \tag{3.4}$$

$$\beta = tan^{-1}(B_Z/({B_X}^2 + {B_Y}^2)^{1/2}) \tag{3.5}$$

The next step to consider is the computation of the pulsation magnetic field toroidal component b_{tor} (transverse to **B** in the horizontal plane), compressional b_{com} (parallel to **B**) and poloidal component b_{pol} (transverse to **B** in the meridian plane) from the pulsation magnetic field components b_X, b_Y and b_Z. From Figure 3.5a we have:

$$b_H = b_X cos\alpha + b_Y sin\alpha \tag{3.6}$$

$$b_{tor} = -b_X sin\alpha + b_Y cos\alpha \tag{3.7}$$

From Figure 3.5b we have:

$$b_{com} = b_H cos\beta + b_Z sin\beta \tag{3.8}$$

$$b_{pol} = -b_H sin\beta + b_Z cos\beta \tag{3.9}$$

The equations 3.2 and 3.5 are used to compute the angles and equations 3.7, 3.8 and 3.9 are then used to compute b_{com}, b_{tor} and b_{pol}.

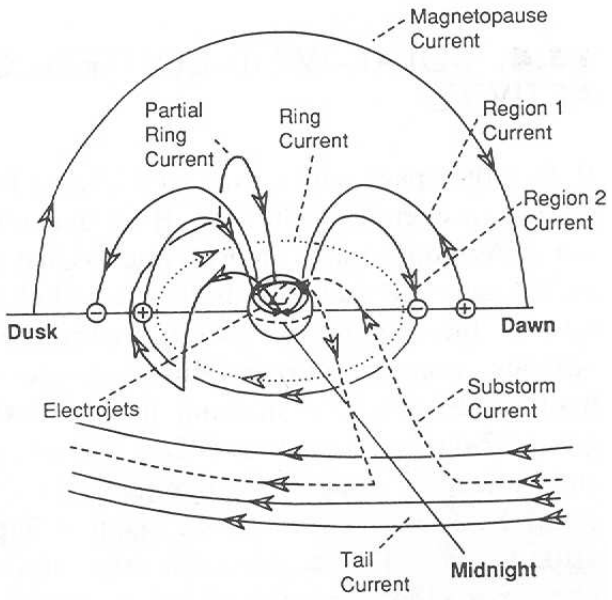

Figure 3.6: *Schematic representation of various current systems linking magnetospheric and ionospheric currents (McPherron, 1995).*

3.5 The effect of field-aligned currents (FAC) on pulsation measurements

This section aims to discuss the effect of field aligned currents on pulsation measurements. However, we shall first briefly give a general description of these current. The circulation of magnetic field in a pattern of closed closed loops within the magnetosphere as a consequence of tangential drag of solar wind is one of the sources that produces the field aligned current system. They flow on two shells surrounding the Earth (see Figure 3.6). The field aligned currents couple to the currents flowing parallel to the local magnetic field. They were first proposed by Birkeland (1908) to explain polar elementary substorm and other polar magnetic disturbances. As shown in Figure 3.6 the field aligned currents flow on two shells completely surrounding the Earth. At the polar regions the magnetosphere is dominated by the portions of ionospheric currents flowing in enhanced-conductivity channels at high latitudes. These currents include large horizontal currents that flow in the ionosphere E-region, called auroral electrojets (Erickson and Winckler, 1973). These currents are linked to the outer parts of the magnetosphere by field-aligned currents which are central to magnetosphere-ionosphere coupling. The electrojets are generally confined to the high latitudes auroral oval during magnetically quiet periods. However during disturbed periods the electrojet increases in strength and even expands to both higher and lower latitudes. This expansion results from two factors: enhanced particle precipitation and enhanced ionospheric electric fields (Erickson et al., 1979).

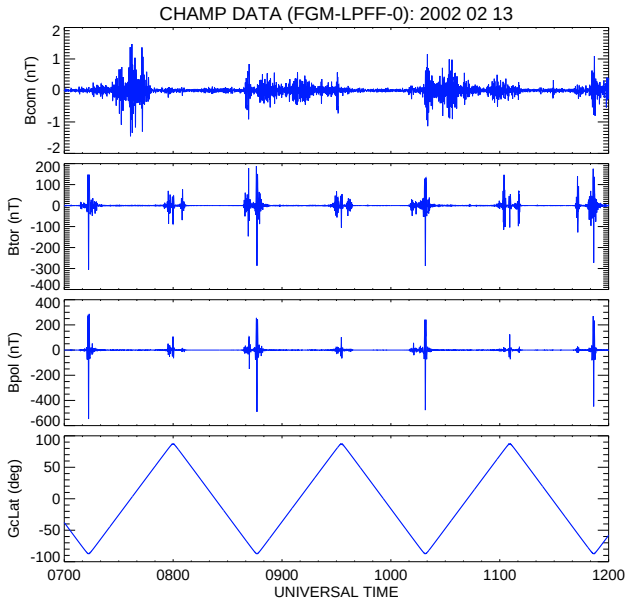

Figure 3.7: *The three field-aligned components, i.e. compressional (B_{com}), toroidal (B_{tor}) and poloidal (B_{pol}) together with the latitudinal profile from top to bottom.*

The circular orbit of CHAMP makes possible its homogeneous coverage of the Earth's sphere. High currents such as FAC are observed by the satellite as it approaches the polar regions. Their effects appear in CHAMP magnetic field data as the disturbances of tens of nT amplitudes as shown in Figure 3.7 when the satellite approaches higher latitudes. In Figure 3.7 shown on the top three panels are field-aligned magnetic field components i.e. compressional (B_{com}), toroidal (B_{tor}) and poloidal (B_{pol}) filtered in the Pc3 frequency range. It can be inferred from the latitudinal profile shown in bottom panel of the figure that there are disturbances in magnetic field data that are more pronounced in B_{tor} and B_{pol} when the satellite is centered around the polar regions. The currents of components perpendicular to the field line are larger than the currents of component along the field line. In Figure 3.7 the transverse components i.e. B_{tor} and B_{pol} are largest, indicating that they are due to FAC. For Pc3 studies it is desirable to avoid intervals dominated by disturbances caused by the flow of high currents. These disturbances when filtered may leak into the Pc3 frequency band and can be erroneously interpreted as Pc3 pulsations. Also the rapid movement of the satellite across field lines in the polar regions may result in spatial structures that can be falsely interpreted as pulsations. The approach taken in this work to avoid false interpretation of non pulsation oscillations as pulsations is explained below.

Instead of relying on the previous results, we carried out a statistical analysis experiment to determine the region where FAC occurs. The aim of the experiment was to establish the latitudes where CHAMP registers these currents which are consequences of FAC. With the

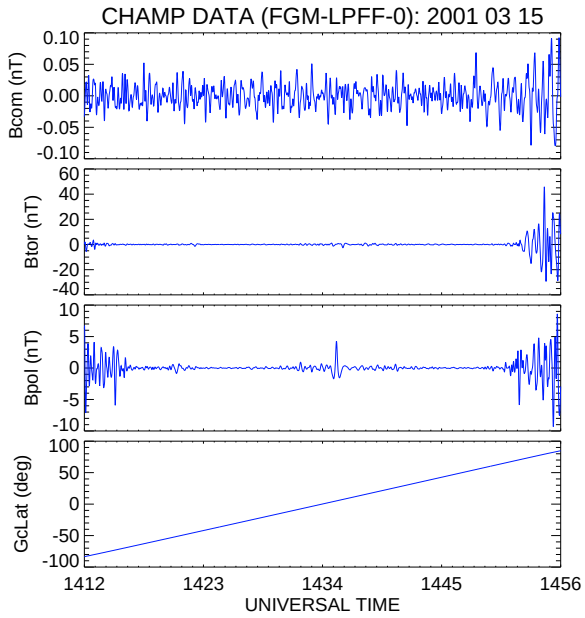

Figure 3.8: *Field aligned components magnetic field measurement and latitudinal profile.*

knowledge of the Pc3 amplitude cut-off, the latitudes where CHAMP registers these high currents can be estimated. The studies of Junginger and Baumjohann (1988) reports the significant correlations between the spectral power level of magnetospheric pulsation and Kp index. The successful completion of the experiment required knowledge about the magnetic activity in the magnetosphere. Therefore the experiment was carried out for various geomagnetic conditions approximated by Kp index values. The Kp index values used were obtained from INTERMAGNET station Hermanus Magnetic Observatory (HMO) archive. In selecting events we scanned a number of pole to pole CHAMP trajectories. The events were then grouped in terms of status or conditions of the magnetosphere represented by Kp index values. Statistically for Kp values 1 and 2 significant high currents were noticed at approximately the 78^0 geocentric latitude. This was the case for both hemispheres. For Kp = 3 and 4, currents were noticed around the 69^0 latitude, whereas for 5 and 6 these currents were observed between the 60^0 and 55^0 geocentric latitude. Values of Kp higher than 6 were not considered for the experiment because of the possibility of an unstable magnetosphere and a high probability of magnetic substorm occurrence at these Kp index values.

The values established are consistent with other spacecraft observations e.g. Triad (Zmuda et al., 1966). The first in-situ observations (Zmuda et al., 1966) and subsequent studies (Armstrong and Zmuda, 1973; Iijima and Potemra, 1976a,b; Waters et al., 2001) deduced that the average FAC pattern centers around the 70^0 magnetic latitude. The classic pattern consists of two rings, region 1 at higher latitude and region 2 at lower latitude with overlap in the pre-midnight region. Figure 3.9 shows the basic pattern of the field-aligned current distribution

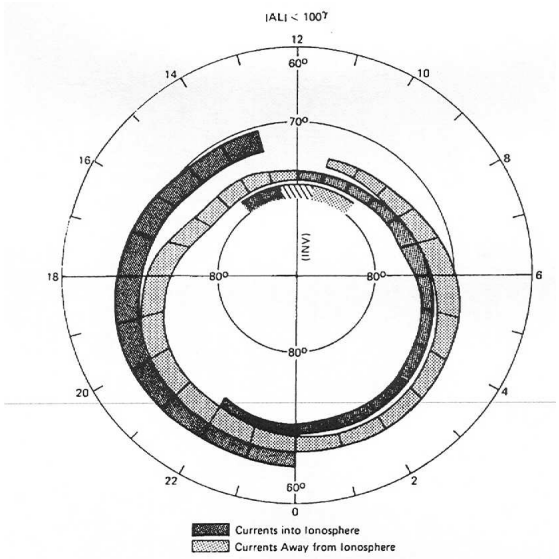

Figure 3.9: *Distribution of the field-aligned currents in the ionosphere (Iijima and Potemra, 1976b).*

(Iijima and Potemra, 1976b) yielded by statistical treatment of magnetic field measurements made on board the Triad spacecraft.

Figure 3.6 summarizes schematically current flows in the magnetosphere responsible for magnetic activity. The equatorial electrojets over the equator are also responsible for the magnetic activity. The sharp spike in B_{pol} of Figure 3.8 centered around 14:34 UT when CHAMP was crossing the equator is attributed to the equatorial electrojet current flows.

3.6 Summary

The ionospheric effects on the ULF signals from the magnetosphere detected on the Earth surface can be studied by directly comparing ground and satellite magnetic field measurements. The launch of the circular orbiting CHAMP satellite provides this kind of opportunity. In this work magnetic field data acquired by magnetometers on board the CHAMP satellite are utilized to investigate properties of the low-latitude continuous pulsation structure. A brief discussion of the CHAMP geomagnetic field mission was given. The FGM sensor frame satellite data set is preferred for Pc3 studies since NEC is contaminated with attitude noise. To study the FLR's the measured magnetic field data are often rotated into the field-aligned coordinates system. This chapter introduced the method used in this study to rotate data into the field-aligned coordinate system.

The laboratory preferred for low latitude Pc3 studies excludes the disturbed regions. The

disturbances we wish to avoid in this study which show up in CHAMP data occur in the polar region and over the equatorial regions. We experimented with CHAMP data to establish latitudes where CHAMP commenced to observe the disturbances. The commencement of these disturbances was found to be dependent on geomagnetic conditions.

The next chapter introduces the analysis techniques i.e. linear and nonlinear methods used in this work to compute spectral estimates.

Chapter 4

Analysis Techniques

4.1 Introduction

This study investigates the structure of continuous geomagnetic pulsations in the magnetosphere. This is done by utilizing linear and nonlinear methods of spectral analysis to analyse ground and satellite magnetometer data and by comparing the two sources of observation. This chapter introduces the analysis techniques used for spectral analysis, namely the Fast Fourier Transform (FFT) and Maximum Entropy Spectral Analysis (MESA). It is composed of two parts. The first part is a review of the mentioned techniques based on the available literature. In this part most of the mathematical material will be offered without proofs. Detailed mathematical proofs and derivations may be found in the cited sources.

The second part presents an evaluation and comparison of FFT and MESA signal processing techniques. In order to test the analysis technique and determine appropriate parameters, geomagnetic pulsation structures are simulated by generating artificial signals consisting of sinusoids with different frequency components and amplitudes. The two analysis techniques are used to compute spectral estimates of the generated test signals.

An inherent shortcoming of the Fast Fourier Transform (FFT) in analysing short duration signals is its limited resolving power, thus prompting the need for an alternative method. This study utilizes the MESA nonlinear method. MESA's significantly greater resolving power will be demonstrated by computing spectral estimates for short signals. This chapter ends with the brief discussion of the crossphase technique used in this work to facilitate the detection of field line resonance.

4.2 Fourier Transform and Fourier Integral

The Fourier transform is the mathematical foundation of relating a time or space signal to its frequency domain representation. Historically it was introduced in 1807 when Fourier presented theory that states that any periodic function can be represented as a series of harmonically related sinusoids. In this section the Fourier Transform is introduced, based on the text by Brigham (1974). The main purpose of transforms is to reduce the complexity of the problem in order to simplify problem solving analysis. The notation and definition used by Brigham are adopted in the discussion to follow. The Fourier Transform differs from general transforms because a function defined as from negative infinity (-∞) to positive infinity (∞) is transformed to a function of another variable also defined as from -∞ to ∞.
The Fourier integral is defined by the expression

$$H(f) = \int_{-\infty}^{\infty} h(t) e^{-j2\pi ft} dt. \tag{4.1}$$

If the integral exists for every value of the parameter f, then equation 4.1 defines $H(f)$, the Fourier transform of $h(t)$. $H(f)$ and $h(t)$ are defined as functions of frequency and time respectively. In this form $H(f)$ is called the continuous-time Fourier transform. The variable f in the complex sinusoid $\exp(-j2\pi ft)$ corresponds to frequency with units in hertz (cycles per second), assuming t has units of time (seconds). The inverse of the Fourier transform is defined as

$$h(t) = \int_{-\infty}^{\infty} H(f) e^{j2\pi ft} df \tag{4.2}$$

The inverse transformation given in equation 4.2 allows the determination of a function of time from its Fourier transform. Generally, the Fourier transform is a complex quantity and is expressible in polar format as:

$$H(f) = R(f) + jI(f) = |H(f)|\, e^{j\theta(f)} \tag{4.3}$$

where $R(f)$ and $I(f)$ are the real and imaginary parts of the Fourier transform. $|H(f)|$ is the amplitude or Fourier spectrum of $h(t)$ and is given by $\sqrt{R(f)^2 + I(f)^2}$. The phase angle $\theta(f)$ of the Fourier transform is given by $\tan^{-1}[I(f)/R(f)]$. For a better understanding refer to Chapter 2 of the book by Brigham (1974). Mathematical applications and examples are given in the cited textbook.

The purpose of continuous-time Fourier transform is to identify the frequencies and amplitudes of those complex sinusoids that combine to form an arbitrary wave form. An example of Fourier transform of a square wave function is illustrated in Figure 4.1. Figure 4.1 shows the schematic interpretation of the Fourier transform. The left panel shows the waveform defined as from

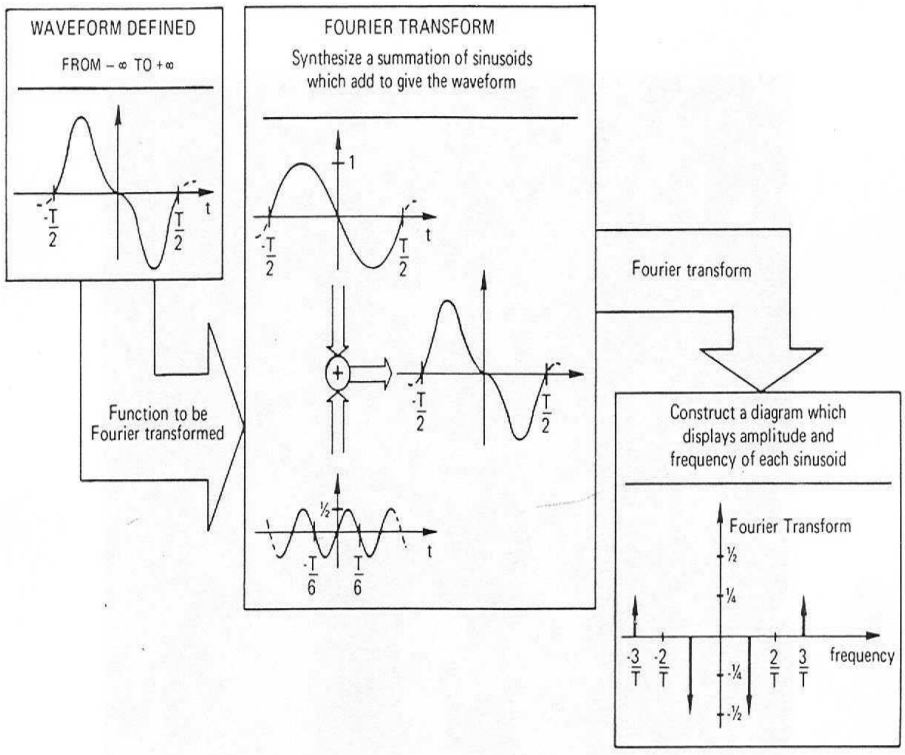

Figure 4.1: *Schematic representation of the Fourier transform applied on the waveform (from Brigham (1974))*

negative infinity to positive infinity, which is a function to be transformed. The middle panel shows synthesized sinusoids which when added, give the waveform. The right panel displays the amplitude and frequency of each sinusoid. In essence, the Fourier transform of a waveform decomposes or separates the waveform into a sum of sinusoids of different frequencies. This interpretation is used in the current study, since pulsation signals are to be decomposed into sinusoids that approximate the actual signal observed.

4.3 The Discrete Fourier Transform (DFT) and Fast Fourier Transform (FFT)

In this study we shall consider discrete signals therefore it is appropriate to introduce Discrete Fourier transform (DFT). The DFT can be defined by equation:

$$X(n) = \sum_{k=0}^{N-1} x_0(k)\, e^{-j2\pi nk/N} \quad n = 0, 1, \ldots, N-1 \tag{4.4}$$

Brigham (1974) developed a relationship between the discrete and continuous Fourier transform. The development uses two basic operations of signal processing sampling and windowing.

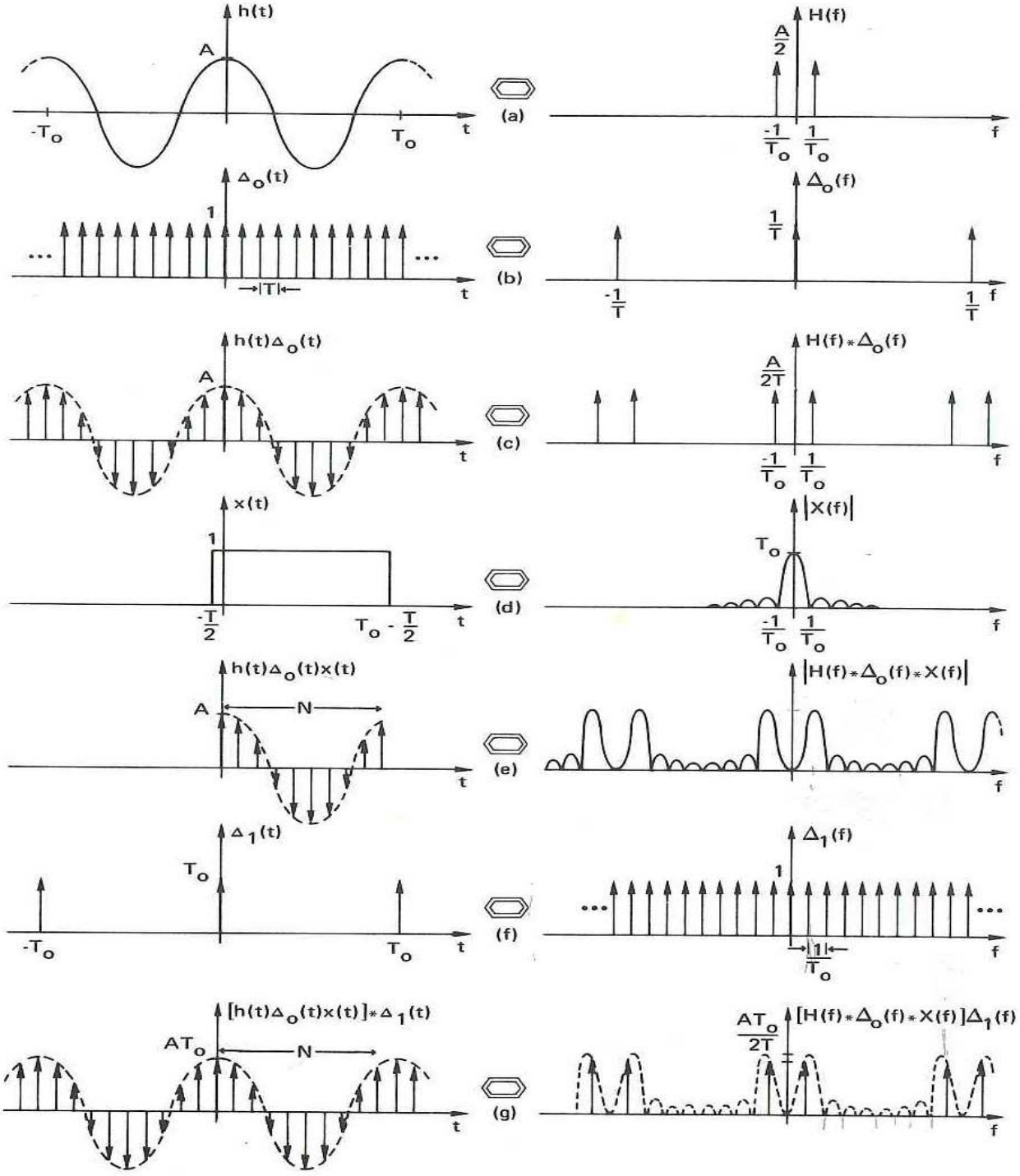

Figure 4.2: *An example of graphical development of the Discrete Fourier Transform adopted from Brigham (1974).*

For our purposes we develop the Discrete Fourier Transform (DFT) from the graphical derivation based on the continuous Fourier transform theory (Brigham, 1974). Consider the example of h(t) and its Fourier transform H(f) shown in Figure 4.2a. This example was chosen because it illustrates the derivation of DFT for the band limited periodic waveform (In this study periodic signals will be analysed). The idea is to sample the continuous sinusoidal function h(t), then truncate the sampled function to N samples in order to formulate a finite length function which is appropriate for machine computation. The continuous waveform h(t) is sampled by multiplying it with the sampling function shown in Figure 4.2b. The sampled waveform h(t)$\Delta_0(t)$ and its Fourier transform are shown in Figure 4.2c. In Figure 4.2c the time domain is the result of the multiplication of h(t) and $\Delta_0(t)$, and the frequency domain is obtained by convolving the frequency functions in Figure 4.2a and b. However, the sampled function still consists of infinite samples. In the quest to formulate a discrete Fourier transform it is necessary to truncate the sampled function so that only N points are considered. In this example the sampled function is truncated by multiplying it with a box car/rectangular function as shown in Figure 4.2d. Figure 4.2e illustrates the sampled and truncated waveform. The Fourier transform of the finite length sampled waveform in Figure 4.2d is obtained by convolving the frequency domain impulse functions of Figure 4.2c and $sinf/f$ frequency function of Figure 4.2d (Brigham, 1974). The finite length time-truncated function in Figure 4.2e has a continuous frequency domain function, hence the pair is not suitable for machine computation. Therefore, it is necessary to modify the frequency domain by multiplying it with a particular frequency sampling function as illustrated in Figure 4.2f. The discrete transform in 4.2g is represented by discrete values that make it suitable for machine computation. The original function h(t) is approximated by N samples, and the original Fourier transform H(f) is also approximated by N samples.

The first step towards applying the discrete transform is to choose the number of samples, N, and the sampling interval, T. The inherent effects of DFT are a leakage and aliasing, which introduce additional frequency components. The leakage is the consequence of the required time domain truncation.

4.3.1 Fast Fourier transform

The Fast Fourier transform (FFT) is an efficient algorithm for the calculation of discrete Fourier transforms which reduces the number of computations needed for N points from $2N^2$ to 2NlogN, where log is a base 2 natural logarithm (Cooley and Tukey, 1965). In the formulation of the FFT matrix the DFT is defined as:

$$X(n) = \sum_{k=0}^{N-1} x_0(k) W^{nk} \tag{4.5}$$

where $W = e^{-j2\pi/N}$. This is a discrete representation of a Fourier series or a Fourier integral at equally spaced points. To estimate DFT we used IDL's available FFT routine. IDL implementation of the FFT is based on the Cooley-Tukey algorithm which breaks up transform of a length N into a transform of length N/2. To compute an N-point DFT when N is composite (N= N_1N_2) the Cooley-Tukey algorithm recursively decomposes the problem by first computing the N_1 transform of size N_2 and then computing the N_2 transform of size N_1 in order to reduce the computation time. The standard development of the Cooley-Tukey algorithm is presented in Oppenheim and Schafer (1975) and Brigham (1988) shows how the DFT of a length-N sequence can be simply calculated from the two length-N/2 DFTs of the even index terms and the odd index terms. This is then applied to the two half-length DFT's to give four quarter-length DFT's, and repeated until N scalars are left which are the DFT values. Because of alternately taking the even and odd index terms, the two forms of the resulting programmes are called decimation-in-time and decimation-in-frequency (Burrus, 2009). For a length of 2M, the dividing process is repeated M=log2N times and requires N multiplications each time. This produces the famous formula for the computational complexity of the FFT of Nlog2N. The IDL FFT algorithm takes advantage of the fact that the Discrete Fourier transform (DFT) of a discrete time series with an even number of points is equal to the sum of two DFTs, each half the length of the original.

In this work in order to reduce the leakage in the periodogram we used recommended cosine-bell tapering transformation in time series prior to the spectrum analysis. In cosine bell transformation a proportion (p) of the data at the beginning and at the end of the series is transformed via multiplication by the weights:

$$W_t = 0.5\left\{1 - cos\left[\pi\left(t - 0.5\right)/m\right]\right\} \quad (for\ t = 0\ to\ m - 1) \tag{4.6}$$

$$W_t = 0.5\left\{1 - cos\left[\pi\left(N - t + 0.5\right)/m\right]\right\} \quad (for\ t = N - m\ to\ N - 1) \tag{4.7}$$

where m is chosen so that $2 * m/N$ is equal to the proportion of data to be tapered (p) (Bloomfield, 1976).

4.4 Maximum Entropy Spectral Analysis

The Maximum Entropy Spectral Analysis (MESA) method introduced by Burg (1967, 1968) is a nonlinear method used in this study to compute spectral estimates. In this section the Haykin and Kesler (1979) text is used to introduce MESA and its mathematical properties. The method was introduced to obviate the unreasonable assumption of the then classical methods, namely the Blackman-Tukey (1959) and periodogram, which were the available two traditional

approaches used for estimating spectra. The Blackman and Tukey (1959) approach involves the basics of the Wiener-Khinchin theorem where the time series is first used to estimate the sample autocorrelation function for a number of lags and which in turn is multiplied by a window function that goes to zero beyond the largest available lag. The Fourier transform of this product is then determined to obtain an estimate of the spectral density. Consequently, the stability and resolution of the spectral estimates of Blackman-Tukey approach depends highly on the choice of the window function. This was evident in the expanded effort by Jenkins and Watts (1969) in determining a good window function. In the Blackman-Tukey approach, the power spectrum $P(\omega)$ is estimated by

$$P(\omega) = \frac{1}{M} \left| \sum_{j=0}^{M-1} \rho_j w_j e^{i\omega j} \right|^2 \tag{4.8}$$

where ρ_j is the autocorrelation function, M is the maximum lag considered and w_j is the window function.

The alternative method to Blackman-Tukey for estimating the spectral density was based on the periodogram usually performed on weighted versions of the time series in order to reduce power leakage. The so-called periodogram is defined as the square magnitude of the Fourier transform of the available time series (Jones, 1965). In the periodogram method the spectral estimates are given by the absolute value squared of the Fourier transform of the time series. Due to this aspect this approach is claimed to have gained popularity after the introduction of the FFT algorithm for performing discrete Fourier transformation (Oppenheim and Schafer, 1975). The periodogram involves FFT in calculating spectral density and a periodic extension of the data is required, i.e., inserting periodicities in the spectral estimate which never existed in the data. In an effort to counter this ill effect and to improve the stability of the approach, the computation of spectral density estimation involved the use of the window function as in the Blackman-Tukey approach. The two classical approaches described above are linear as they involve the use of linear operations on the available time series, where artificial biasing of good data produce spectral estimates of reduced resolution which may be negative and in disagreement with the available data.

The major shortcomings of these two methods arise from the fact that in practice data are of finite length. They also involve the use of window functions which are independent of the properties of the stochastic processes being analyzed. Without extra care on the application of these methods, the user may draw a false or misleading conclusion. Another major shortcoming of these linear methods is the unrealistic assumption about the extension of the data outside the known interval. The nonlinear method MESA was introduced to obviate the assumptions

which the linear method of spectrum analysis makes about the extension of the data outside the known interval. MESA as a maximum entropy method is deeply rooted in information theory (i.e. entropy), and it seeks to extract maximum information from data.

The MESA method of Burg (1967, 1968) is a nonlinear method for computing spectral estimates where the idea is to choose the spectrum which corresponds to the most random or unpredictable time series in which the correlation function agrees with a set of known values. This condition is equivalent to an extrapolation of the autocorrelation function of the available time series by maximizing the entropy of the process (Haykin and Kesler, 1979). The advantages of MESA are that it provides greater resolution than the linear methods and has the ability to analyze short data records (Burg, 1967). The maximum entropy method is governed by the principle that when estimating spectra the user should choose the spectrum which:

- makes the fewest assumptions regarding the information content of the unavailable data,
- and incorporates and is consistent with all the measured data.

The outstanding feature of MESA and its greatest advantage over the conventional linear methods is the increased resolving power when applied to time series of short duration. Furthermore, the computation time required for estimating spectra with MESA is of the same order of magnitude as conventional linear spectral estimators.

4.4.1 Derivation of the MESA Spectral Estimator

The full derivations of mathematical equations and descriptions of properties which control and guide the correct usage of MESA is beyond the scope of this work. However, the mathematical description and properties are reviewed based on the Lacoss (1971), Burg (1972), Burg (1975) and (Ulrych, 1972) mathematical derivations. Only the major equations will be stated without their proofs, which are available in the cited source texts.

For a stationary complex discrete time series $x\,(t)$ with sampling interval dt and the Nyquist frequency $f_N = \frac{1}{2dt}$, the application of MESA would be to choose a spectrum that maximizes the entropy of the process (i.e. the spectrum of corresponding to the most unpredictable time series). The spectrum needs to be constrained to the known values of the autocorrelation function. The exercise is to find the real positive function of spectral density ($S(f)$) which maximizes

$$h = \frac{1}{4f_N} \int_{-f_N}^{f_N} ln\left\{S\,(f)\right\} df \tag{4.9}$$

where h is the entropy rate, subject to the constraint that

$$R(K) = \int_{-f_N}^{f_N} S(f)\, e^{i2\pi f K \Delta t} df \qquad (-M \leq K \leq M). \tag{4.10}$$

$R(K)$ is the autocorrelation function at lag K. One approach to solving this constrained optimization problem of finding the value of $S(f)$ that maximizes 4.9 subject to constraints 4.10 is to make use of a variational principle and Lagrange multipliers. The solution to the problem solved with stated approaches is given in equation 4.11

$$S(f) = \frac{1}{4 f_N \sum_{K=-M}^{M} \lambda^* e^{i2\pi f K \Delta t}} \tag{4.11}$$

The next step is the determination of the values for the set of coefficients λ^* in 4.11 such that the spectral density estimate is consistent with the known values of the autocorrelation function, that is 4.10. Substituting 4.11 into 4.10 yields

$$R(m) = \frac{1}{4 f_N} \oint \frac{z^{-M}}{\sum_{K=-M}^{M} \lambda_K^* z^{-K}} \frac{f_N dz}{i\pi z} \tag{4.12}$$

In equation 4.12 the z-transformation notation is assumed by setting $z = e^{-i2\pi f \Delta t}$. The contour integration is around the unit circle in the counterclockwise direction. Using the Hermitian property of the coefficients λ_K makes it possible to express the denominator of 4.12 as a product of two polynomials $Am(z)$ and $Am^*(m)$. Making use of Couchy's integral theorems together with the manipulation of 4.12 and product of the introduced polynomials, yields

$$\sum_{K=0}^{M} a^* R(K-m) = \begin{cases} \frac{P_{M+1}}{a_0} & m = 0 \\ 0 & m = 1, 2, ...M \end{cases} \tag{4.13}$$

This set of equations is similar in form to the prediction-error filter equations. Taking the complex conjugate of the equation above and making use of the Hermitian property $R^*(K) = R(-K)$ and selecting $a_0 = 1$ (this choice is explained in the source text), yields

$$\sum_{K=0}^{M} a_K R(m-K) = \begin{cases} P_{M+1} & m = 0 \\ 0 & m = 1, 2, ..., M \end{cases} \tag{4.14}$$

Equation 4.14 can be written in the matrix form as

$$\begin{bmatrix} R(0) & R(-1) & R(-M) \\ R(1) & R(0) & R(1-M) \\ \vdots & \vdots & \vdots \\ R(M) & R(M-1) & R(0) \end{bmatrix} \begin{bmatrix} 1 \\ a_1 \\ \vdots \\ a_M \end{bmatrix} = \begin{bmatrix} P_{M+1} \\ 0 \\ \vdots \\ 0 \end{bmatrix} \tag{4.15}$$

Given in equation 4.15 is the set of equations for finding the Mth order Prediction Error Filter (PEF) (1,a_1,a_2,... a_M) with P_{M+1} being the filter error power. Given that $z{=}e^{-i2\pi f\Delta t}$ the desired expression for calculating MESA spectral density estimate $S(f)$ is expressed as:

$$S(f) = \frac{P_{M+1}}{2f_N \left|1 + \sum_{m=1}^{M} a_m e^{-i2\pi f m \Delta t}\right|^2} \tag{4.16}$$

where P_{M+1} is the output power of a prediction-error filter of order $M{+}1$ and a_m, m =0,1,2,...,M, are the corresponding filter coefficients.

The exercise to determine maximum entropy spectrum is reduced to the calculation of a prediction error filter (PEF) equivalent to a_m in equations 4.15 and 4.16 and the corresponding error power. Burg (1968) was first to develop the algorithm to compute PEF coefficients. Chen and Stegen (1974) carried out a detailed investigation using short harmonic signals and demonstrated that MESA sometimes suffers anomalous behaviour such as frequency shifts, when the Burg (1968) algorithm is used to compute the PEF coefficients. The limitation of the Burg method is fundamental (Swingler, 1979) and can be traced to two sources: (1) the bidirectional nature of the Burg PEF and (2) the assumption that the autocovariance matrices implicitly involved in producing the algorithm are Toeplitz (Anderson, 1974), thus permitting the use of the Levinson recursion (Levinson, 1947) to form a fast, recursive technique. The second limitation is responsible for the frequency shifts incurred on processing sinusoids.

Ulrych and Clayton (1976) and Swingler (1979) independently proposed an alternative method of computing the PEF coefficients, which they called the least squares (LS) estimator and which obviates the shortcomings of the Burg (1968) algorithm. The LS estimator approach, minimizes the prediction-error power with respect to all of the autoregressive (AR) coefficients at a particular AR order. In LS estimator the power of forward and backward prediction given by

$$P_{M+1} = \frac{1}{2(N-M)} \sum_{t=1}^{N-M} \left|X_{t+m} + \sum_{m=1}^{M} a_{m,M} X_{t+M-m}\right|^2 + \left|X_t + \sum_{m-1}^{M} a_{m,M} X_{t+m}\right|^2 \tag{4.17}$$

is minimised with respect to all the filter coefficients of order M. Differentiating 4.17 with respect to each of coefficients leads to the following linear system:

$$\begin{bmatrix} r_{11} & r_{12} & \cdots & r_{1M} \\ r_{21} & r_{22} & \cdots & r_{2M} \\ \vdots & \vdots & & \vdots \\ r_{M1} & r_{M2} & \cdots & r_{MM} \end{bmatrix} \begin{bmatrix} 1 \\ a_{1,M} \\ \vdots \\ a_{M,M} \end{bmatrix} = \begin{bmatrix} S_1 \\ S_2 \\ \vdots \\ S_M \end{bmatrix} \tag{4.18}$$

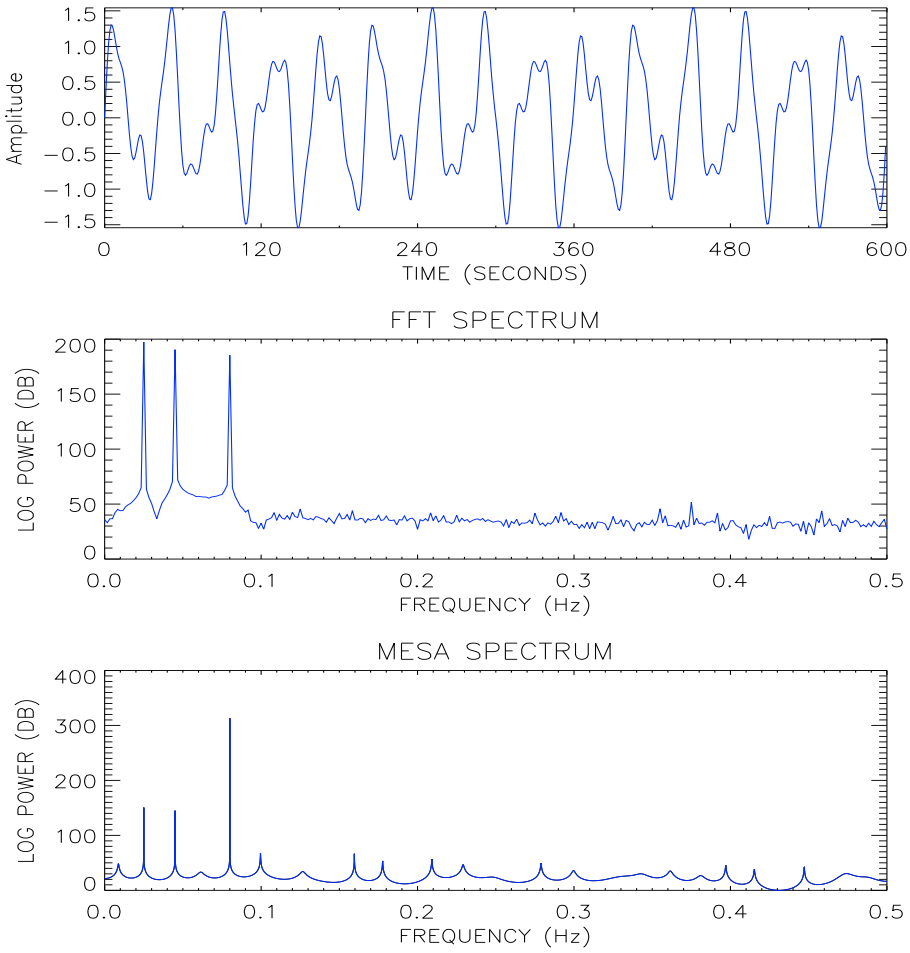

Figure 4.3: *Top graph: The synthesized 600 second signal time profile, Middle graph: FFT spectral estimate, Bottom graph: MESA spectrum*

where:

$$r_{ij} = \sum_{t=M+1}^{N} X_{t-i}X_{t-j} + \sum_{t=1}^{N-M} X_{t+i}X_{t+j} \quad i,j = 1,2,\cdots,M \tag{4.19}$$

$$S_i = \sum_{t=M+1}^{N} X_{t-i}X_t + \sum_{t=1}^{N-M} X_{t+i}X_t \quad i = 1,2,\cdots,M \tag{4.20}$$

The matrix is symmetrical but not necessarily Toeplitz, although it asymptotically approaches the Toeplitz autocovariance matrix for large N. In these equations X_t is spectral representation of AR processes. The current study adopts the Ulrych and Clayton (1976) method for computing the PEF coefficients using the algorithm shown above to calculate the prediction error filter.

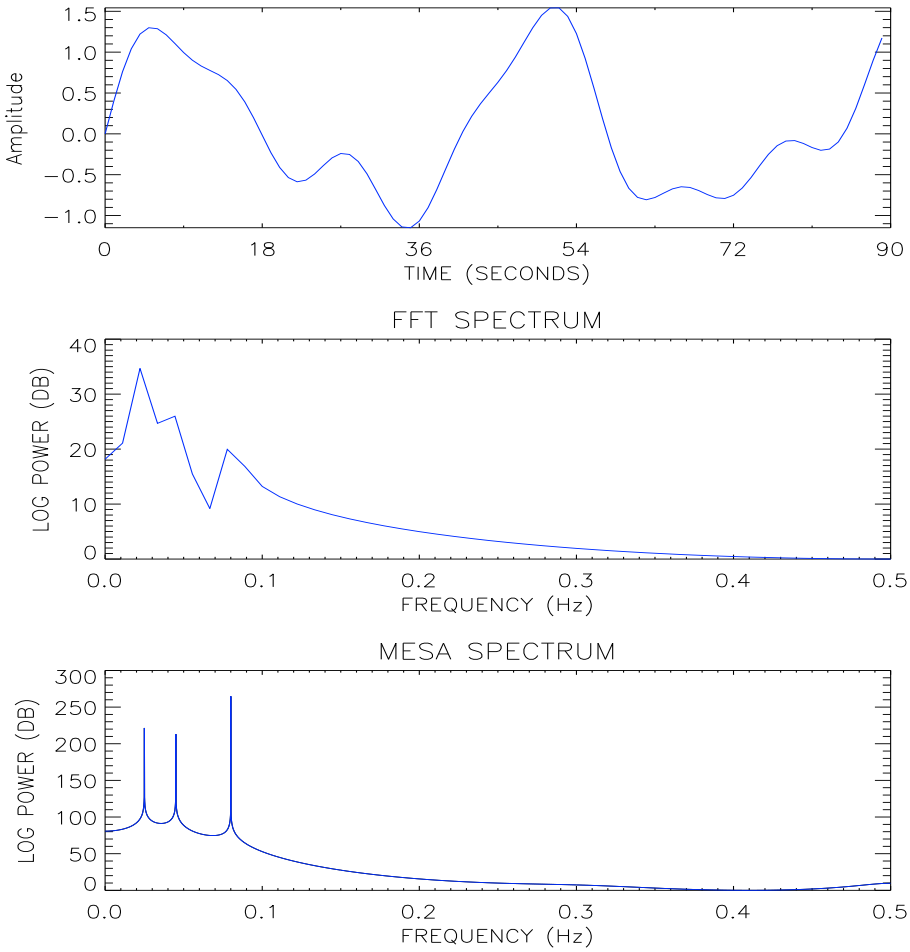

Figure 4.4: *Top graph: The synthesized 90 second signal time profile, Middle graph: FFT spectral estimate, Bottom graph: MESA spectrum*

4.5 The application of the FFT and MESA

In this section the shortcomings of FFT and the superiority of MESA for short time signals are demonstrated by experimenting with artificially generated signals. The test signal consists of sinusoids with three frequency components of different amplitudes intended to resemble a typical Pc3 event. A sinusoid is a function having the form:

$$x\left(t\right) = A\, sin\left(2\pi f t + \phi\right) \tag{4.21}$$

where t is the independent variable, and the fixed parameters amplitude A, frequency f and ϕ phase are all real constants. The frequency values used to generate the synthetic signal are shown in Table 4.1 together with their corresponding amplitudes. The chosen frequency values are within the range of Pc3 frequencies; hence, the signal represents an approximated structure of a Pc3 geomagnetic pulsation. Therefore, analysis of the spectral estimates calculated by the two methods can be viewed as interpretations of actual data. The superiority of the resolving

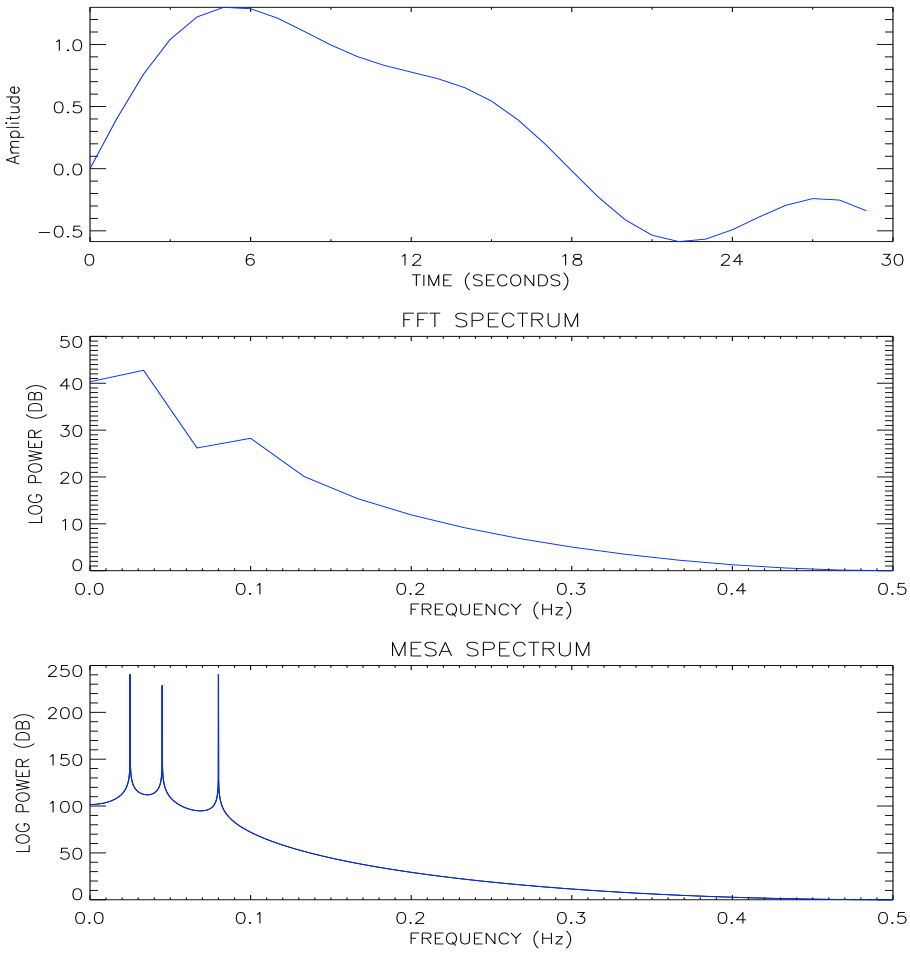

Figure 4.5: *Top graph: The synthesized 30 second signal time profile, Middle graph: FFT spectral estimate, Bottom graph: MESA spectrum*

power of MESA compared to that of FFT is now demonstrated by computing spectral estimates for 600, 90 and 30 second signals. The total length of signal ($T = N * dt$) is derived from the product of total number of points (N) and sampling interval (dt), which in these examples was set to 1 second. The respective PEF coefficient length used for the MESA computations based on the (Chen and Stegen, 1974) approach are 60, 9 and 6 respectively. The next section discusses the reasons for the choice of these values in detail.

Figure 4.3 shows the experimental results for the 600 second signal. The logarithmic power is plotted up to the Nyquist frequency. In this case both methods give sharp peaks at expected frequency position (see Table 4.1). Nonetheless, the MESA peaks are sharper than the FFT, the calculations of which is based on the periodogram. However, MESA has some well-known defects e.g. the amplitudes estimates are not fully accurate (Kane and Trivedi, 1982). In the earlier years Lacoss (1971) suggested that to obtain reliable estimates of amplitude some numerical integration should be carried out over the peak area. Our prescription is to rely on

Frequency (Hz)	Period (sec)	Amplitude	Phase
0.025	40.00	1	0
0.045	22.20	0.45	0
0.080	12.50	0.25	0

Table 4.1: *The artificially generated variable values*

logarithmic power of peak value not the power of the peak. Moreover, we are mainly interested in the frequency content rather than the amplitude.

Figure 4.4 shows the results for the 90 second signal. FFT peaks tend to become broader making it difficult to determine correct frequency position. It is noticeable that MESA peaks maintain their sharpness and are still placed at the expected frequency positions. In addition, the spurious peaks of low power seen in Figure 4.3 (see the section on the PEF length) are not visible in Figure 4.4. In an effort to demonstrate the extreme superiority of MESA for analyzing short signals, the spectra for the 30 second signal are shown in Figure 4.5. In the FFT spectrum only two out of three peaks are resolved and they are much broader with respect to Figures 4.3 and 4.4. In a case such as this it is difficult to determine the correct frequency position. This can result in a high probability of misinterpreting spectrum information. The MESA peaks are still intact at the correct frequency positions. Overall, these examples clearly demonstrate the superiority of MESA over FFT for analyzing short data records.

In this research Pc3's are investigated using CHAMP satellite data. The satellite traverse a degree and half of latitude per minute. The low orbit of the CHAMP satellite poses a problem of rapid movement across different L-shell regions. Consequently, the spectral content will also likely change rapidly e.g. field line resonant frequency varies as function of latitude. In order to account for this effect MESA will be preferred over FFT, to compute dynamic spectra because of its high resolving power despite the short duration of the signal.

4.5.1 Length of Prediction Error Filter

It has been shown that MESA is a better method for computation of spectral estimates for short signals than FFT. However, it is important to determine and use the correct PEF length (i.e. number of coefficients of the prediction error filter) when using MESA (Chen and Stegen, 1974). A PEF length which is too short results in a highly smoothed spectrum where some peaks may not be resolved, thus precluding the advantages of MESA. An excessive PEF length introduces spurious peaks and peak splitting into the spectrum. In numerous research papers following the inception of MESA, the choice of PEF length was often made subjectively, which may have led to less than optimal results.

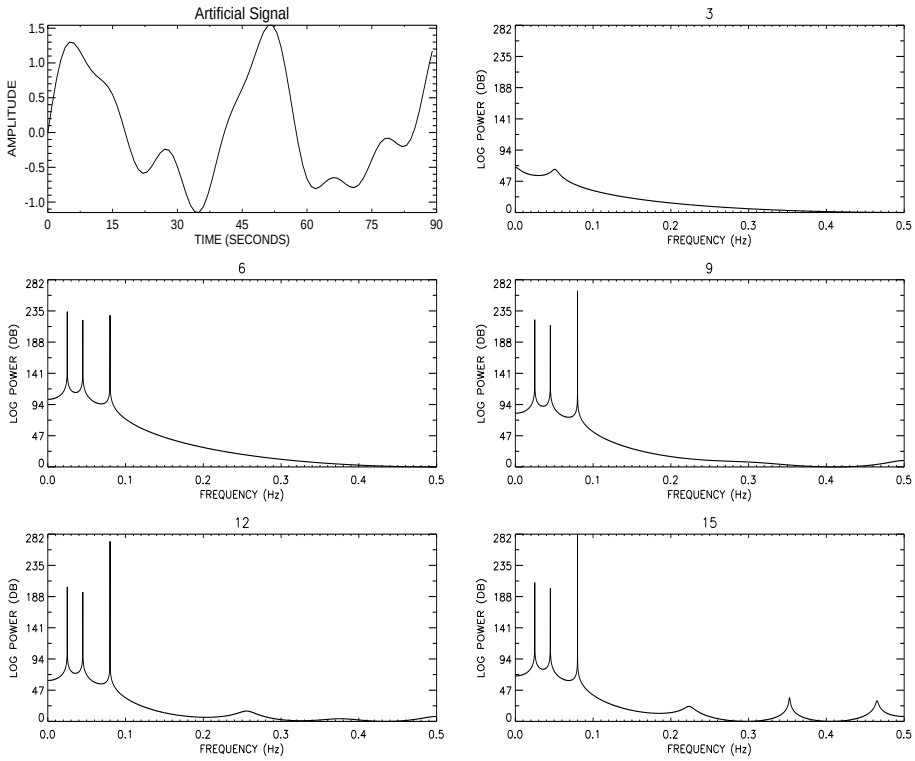

Figure 4.6: *MESA spectral estimates of a 90 second test signal consisting of three sinusoids.*

In this study, the PEF length is established by experimenting with the generated test signals. The main aim of experiments in this section is to illustrate the effect of PEF length on the spectrum by determining the spectra of signals of 90, 60, 45 and 30 second duration. The experimental results are displayed in Figure 4.6, 4.7, 4.8 and 4.9 respectively. The spectra are all labelled according to the PEF length value used in determining each spectrum. The too short lengths yield highly smoothed spectra where not all peaks are resolved for all frequencies. On average, both 90 and 60 second signals spectra suggest that a PEF length value which is approximately 10 percent of the total length of the signal is required to resolve peaks. For the 45 and 30 second signals a value slightly more than 10 percent total length of the signal is required to resolve the three expected peaks.

Fougere et al. (1976) and Fougere (1977) argue that the filter length is not the only critical parameter affecting spectrum resolution by showing the effect of noise level. The effect of noise level is also explored in this work but only for a 90 second signal consisting of sinusoids with three frequency components of different amplitude as given in Table 4.1. As mentioned in the previous section the signal is intended to resemble a Pc3 event. The choice of 90 second signal is based on the dynamic spectrum as computed in the following chapters. For the satellite measurements the dynamic spectrum will be computed for 90 seconds and progressively

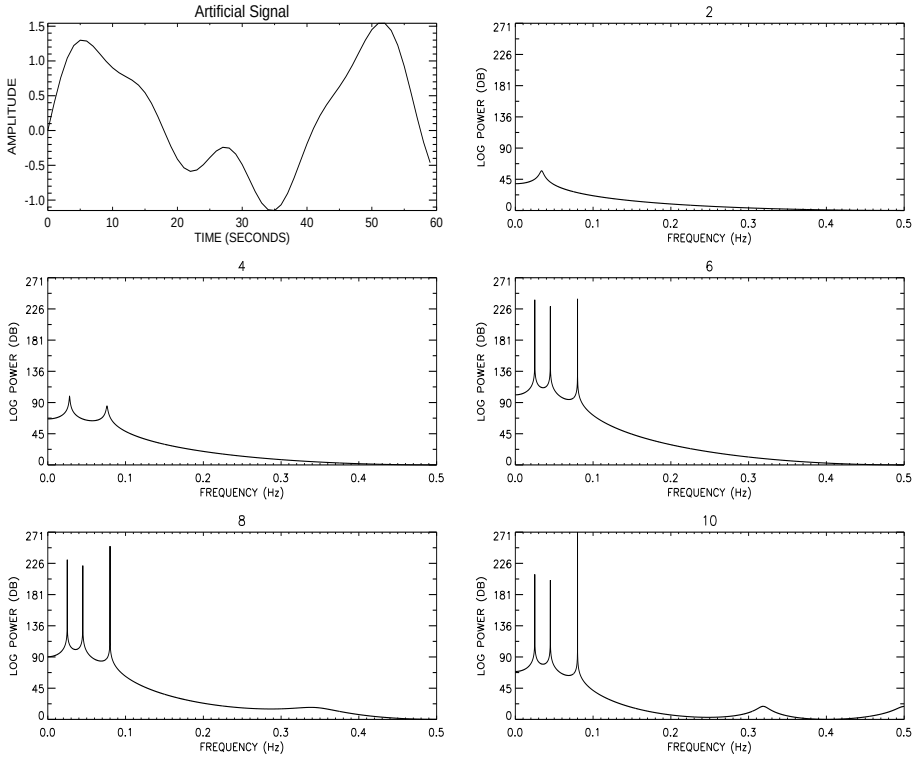

Figure 4.7: *MESA spectral estimates of a 60 second test signal consisting of three sinusoids.*

shifted by 10 seconds. Figures 4.10, 4.11, 4.12 and 4.13 show spectra for the described time series without and with 5, 10 and 30 percent random noise added.

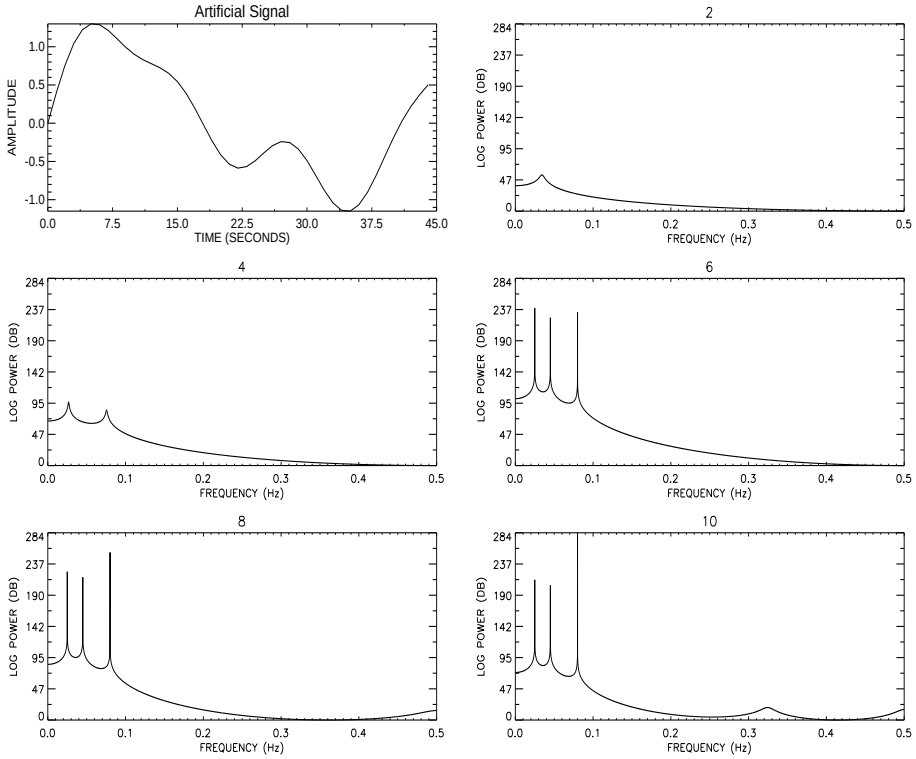

Figure 4.8: *MESA spectral estimates of a 45 second test signal consisting of three sinusoids.*

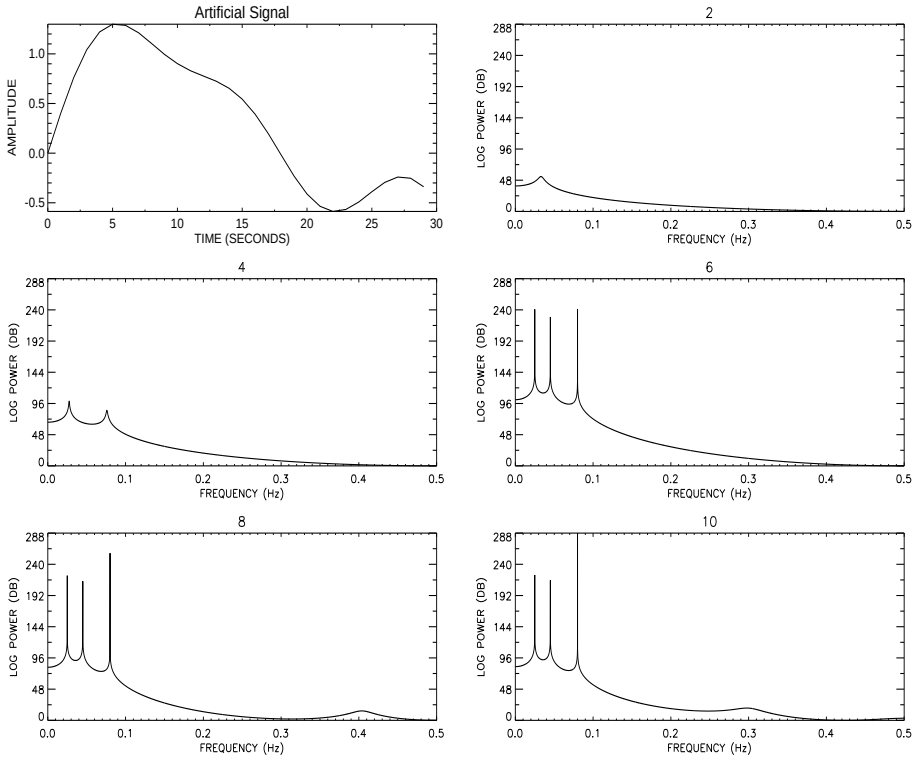

Figure 4.9: *MESA spectral estimates of a 30 second test signal consisting of three sinusoids.*

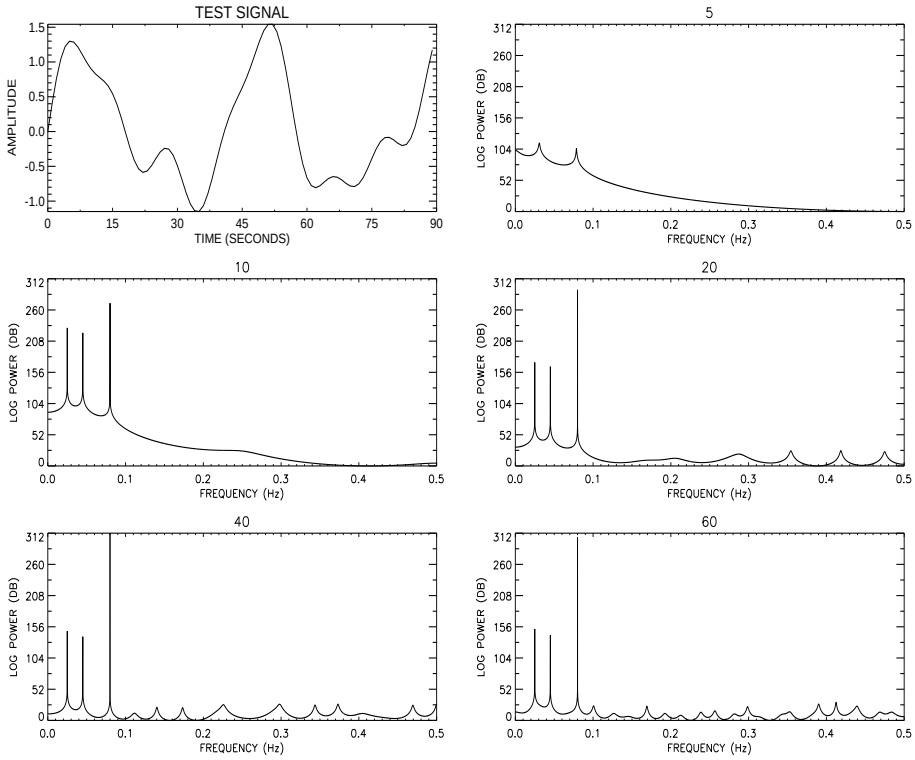

Figure 4.10: *MESA spectra of a 90 second signal for different prediction error filter lengths. The value at top of each spectrum is the prediction error filter length.*

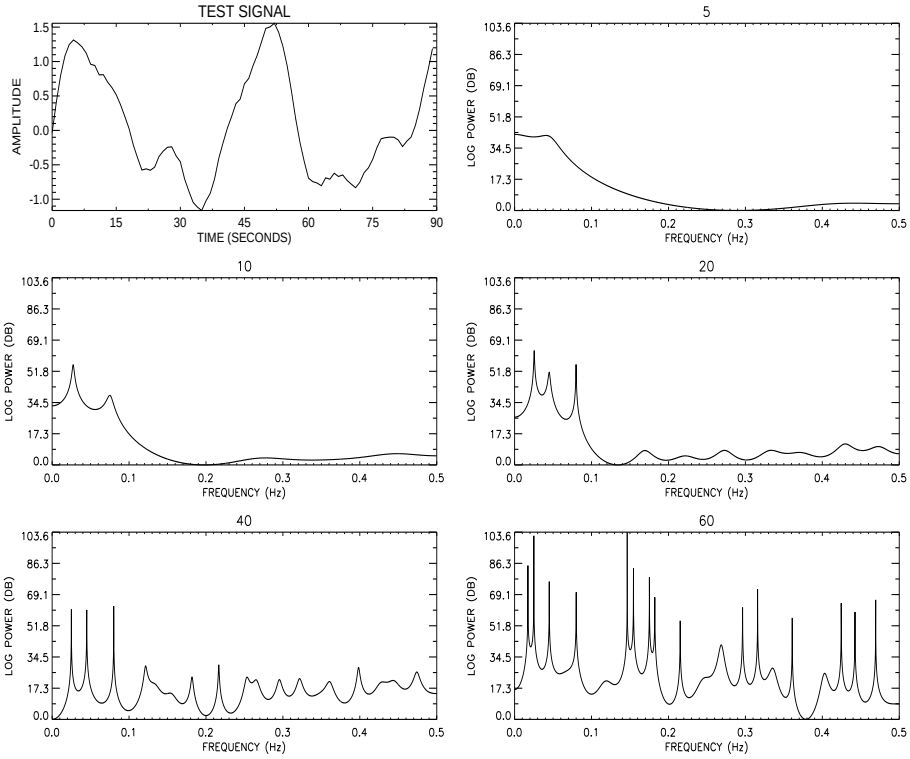

Figure 4.11: *MESA spectral estimates of a 90 second signal consisting of three sinusoids with 5 percent random noise added.*

The spectra are all again labelled according to the PEF length values used in determining the spectra. For the no-noise signal the spectrum determines that lowest PEF length results in poor resolution spectrum, with only two out of three peaks resolved. This suggests that merging of the peaks occurred. In the spectrum with the value 10 the three expected peaks are resolved without spurious peaks emerging which is not the case for signals to which noise was added. For the 5 percent noise signal a PEF length of 20 yields optimum results resolving all three expected peaks whereas for lengths less than 20 the peaks merged. For a signal with random noise level raised to 10 percent it is clear that a length greater than 20 is required since the length of 20 yields less than optimum results. For this length of 20 all peaks are visible but the 0.045 Hz peak is arguably merging with the other two peaks. In the case of the signal with the random noise level raised to 30 percent, it is clear that the length of 20 resolved only two peaks (see Figure 4.13). It was noticed from extended study that a PEF length of 35 was required to resolve the three peaks. For the no-noise signal and signals with noise, the excessive lengths of 40 and more start introducing spurious peaks into the spectrum.

The important point to note is that for a pure signal the shorter length is preferable, whereas for signals contaminated with noise a longer length is preferable. The PEF values used in this study would lie within the range of 15 to 20. The approach followed here of establishing

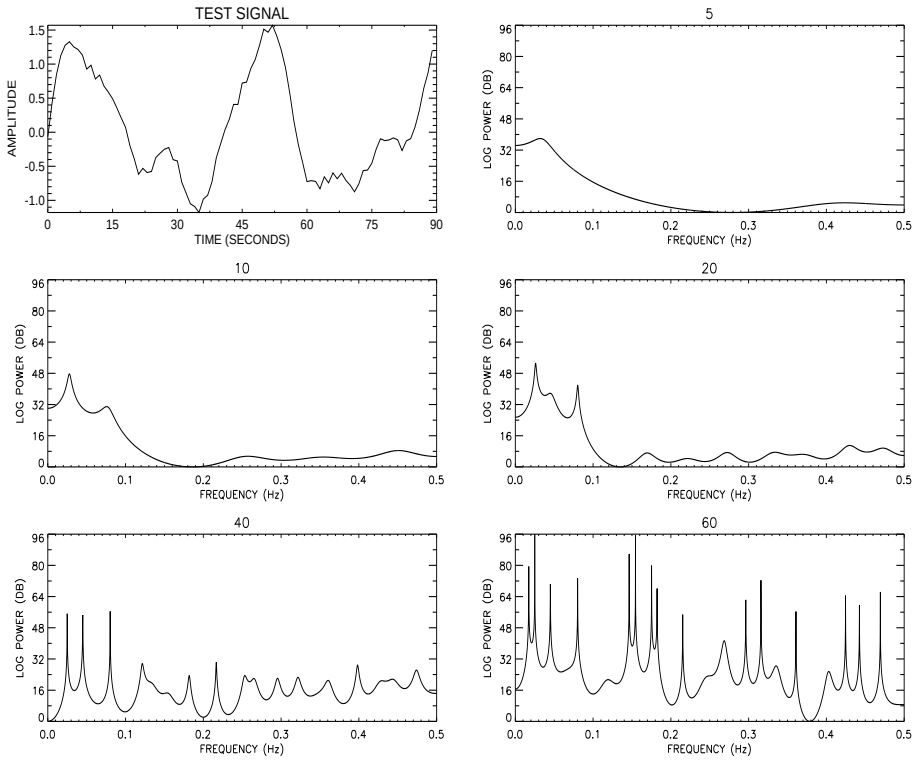

Figure 4.12: *MESA spectral estimates of a 90 second signal consisting of three sinusoids with 10 percent random noise added.*

the dependence of optimum filter length on noise level is similar to the approach of Chen and Stegen (1974). The effect of amplitude was also studied but the results are not shown. It was found that a greater PEF length is also required if one of the amplitudes is very much less than the others (e.g. by a factor 10) especially if random noise greater than 5% is added to the signal.

We also experimented with HER ground data and computed dynamic spectra using different PEF lengths in the range of 15 to 45, changing the length in steps of 5 for the event discussed in chapter 5. The results are shown in Figure 4.14 for the least, moderate and extreme lengths. Shown from panels (a) to (f) are spectra computed with PEF corresponding to 15, 20, 25, 30, 35 and 45 respectively. The full interpretation of the frequency structures observed is available in chapter 5. The main aim of the exercise here was to experiment with PEF coefficient established with test signal on the real data. In a spectrum with PEF = 15 there is a most intense frequency band at 45 mHz. It is noticeable that for PEF length greater than 25 splitting of the most intense frequency band present in the dynamic spectra is observable. In this example the peak splitting is more pronounced in the spectrum with PEF = 35. The length 35 is not an absolute value since the splitting is sometimes observable at length smaller or greater than this. Since the prime objective of this study is to identify FLRs, which if present, are generally one of the more intense spectral components, we regard PEF's of 15 and 20 respectively, for the

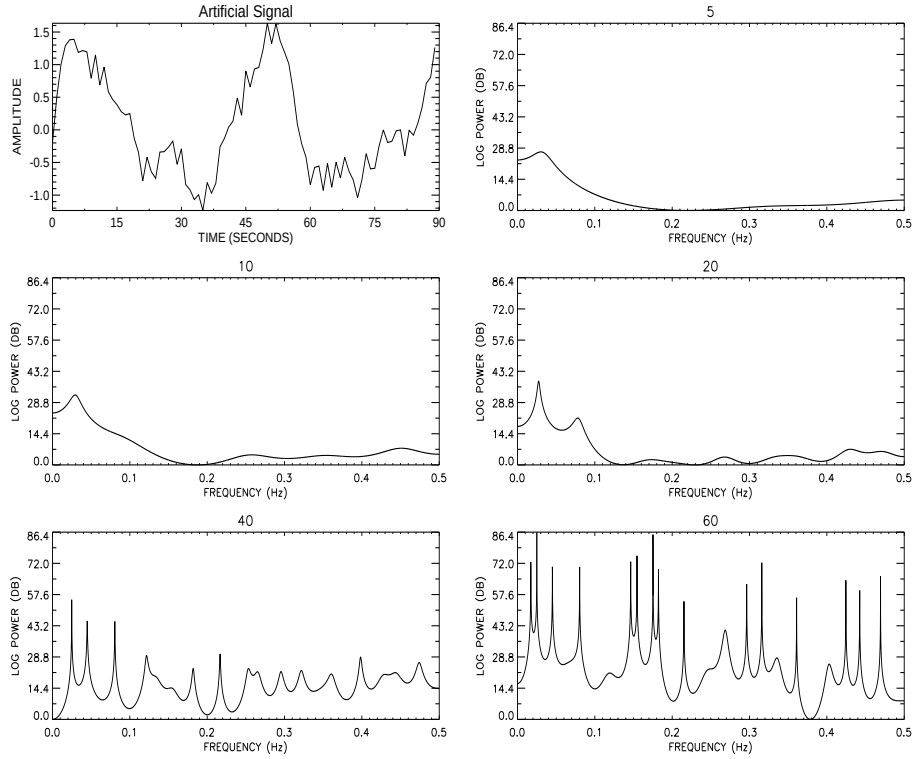

Figure 4.13: *MESA spectral estimates of a 90 second signal consisting of three sinusoids with 30 percent random noise added.*

ground-based and satellite data as adequate. However, if one were interested in studying the fast mode fine structure in more detail, then a larger PEF length would probably be desirable.

4.6 Detection of FLR's

In this section we describe a tool used to identify the eigenfrequencies of the magnetospheric field. Baransky et al. (1985) proposed a method for the direct measurement of the eigenfrequency of the magnetic field lines using ground based magnetometer data. They demonstrated that either the difference or ratio of Pc3-4 pulsation amplitude spectra observed at two closely spaced meridional ground stations can be used to determine the eigenfrequency associated with the field lines between the two stations. The resonant frequency was identified as the frequency where the amplitude difference equalled zero or the amplitude ratio equalled unity. Waters et al. (1991a), on applying this method to low-latitude Pc3 pulsation data, found that it was difficult to identify the resonant frequency unambiguously, since more than one frequency satisfied the condition. They proposed an alternative method of determining the presence of a field line resonance by the use of the H-components from two closely spaced stations to obtain the crossphase. The crossphase refers to a phase difference between two signals and it is calculated from the output of an readily available FFT. For two sampled time series $X(t)$ and $Y(t)$ the

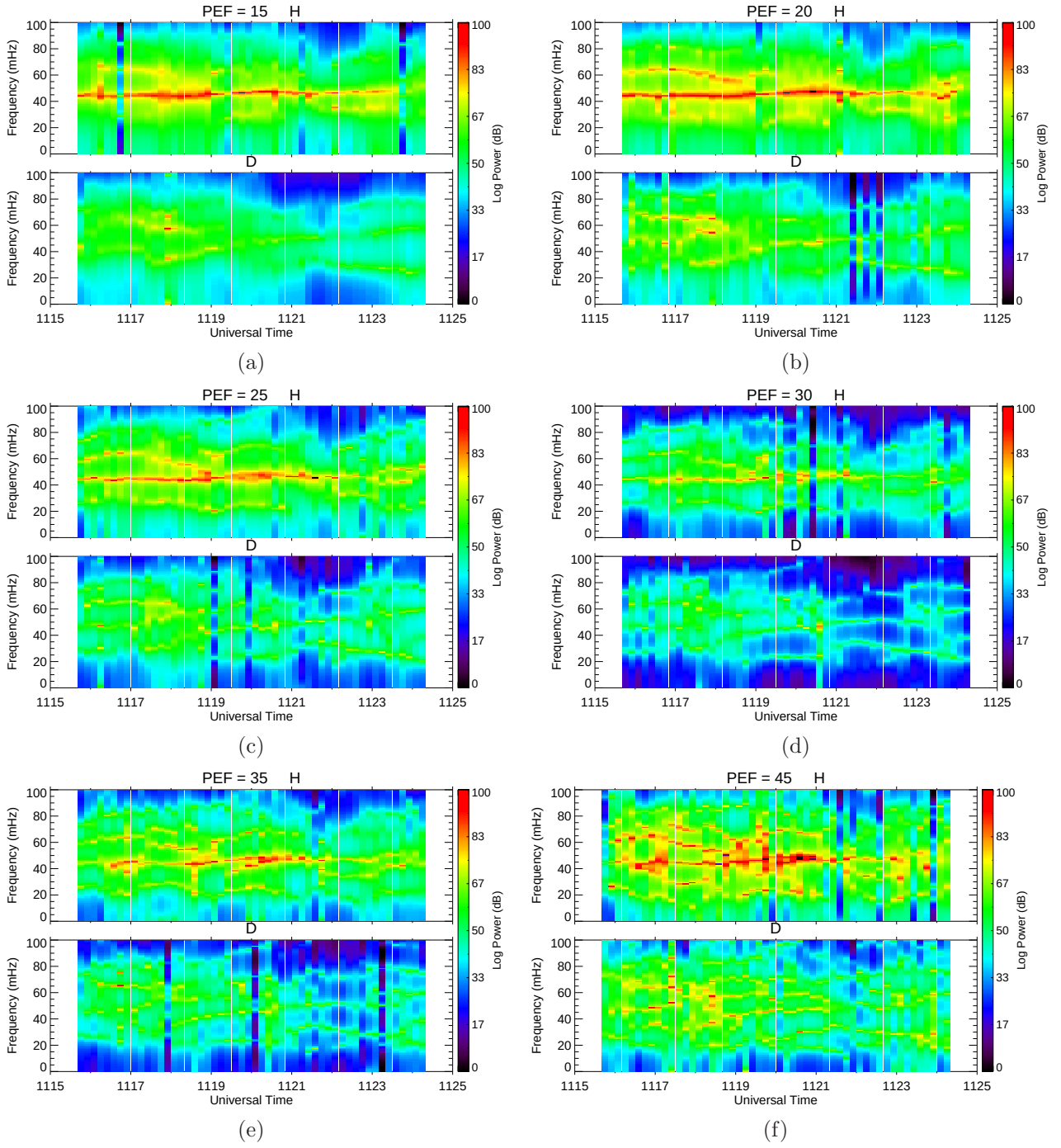

Figure 4.14: *MESA Hermanus ground dynamic spectra for the H- and D-components observed on 15 February 2003. The spectra are shown for different PEF lengths as indicated each spectrum heading.*

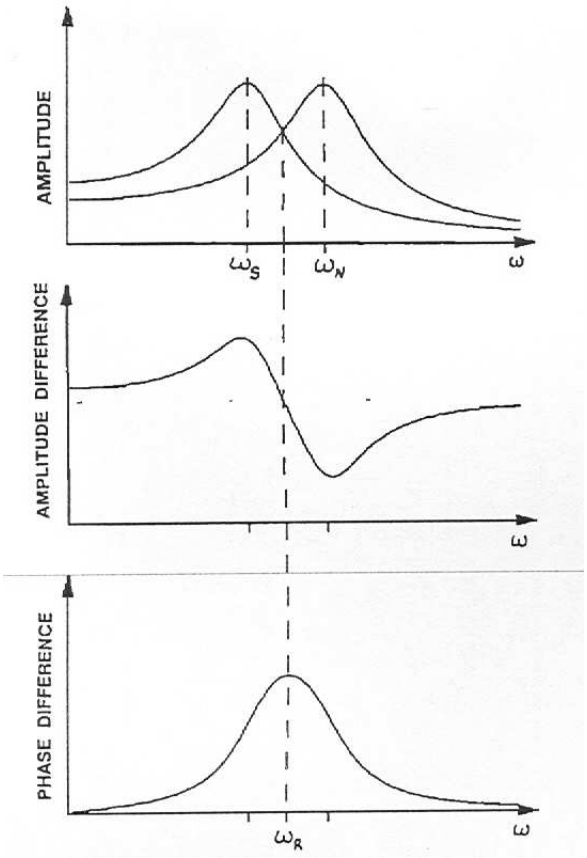

Figure 4.15: *Crossphase schematic plots of meridional stations at positions (*S*) and (*N*), the plots are for systems with slightly different eigenfrequencies. Shown from top to bottom are a) The amplitude response in each case and the meridional b) amplitude and c) crossphase difference adopted from Waters et al. (1991a).*

phase difference is calculated as:

$$\phi_{XY} = tan^{-1}\left[\frac{I(P_{XY}(f))}{Re(P_{XY}(f))}\right] \tag{4.22}$$

where P_{XY} is the cross power spectral estimates (Waters et al., 1991b). With this method the peak in the crossphase spectrum identifies the resonance. In their studies the technique based on the crossphase spectrum was used to identify eigenfrequencies of Pc3 pulsations recorded at stations located at L = 1.8 and L = 2.7 and used to study the temporal evolution of local field line resonances.

Figure 4.15 shows schematically the amplitude difference technique of Baransky et al. (1985) and the crossphase technique of Waters et al. (1991a) for detecting FLR frequencies. In the figure ω_R represents a resonant frequency. The crossphase technique of Waters assumes the existence of two simple harmonic oscillators to describe the oscillation of field lines at the lati-

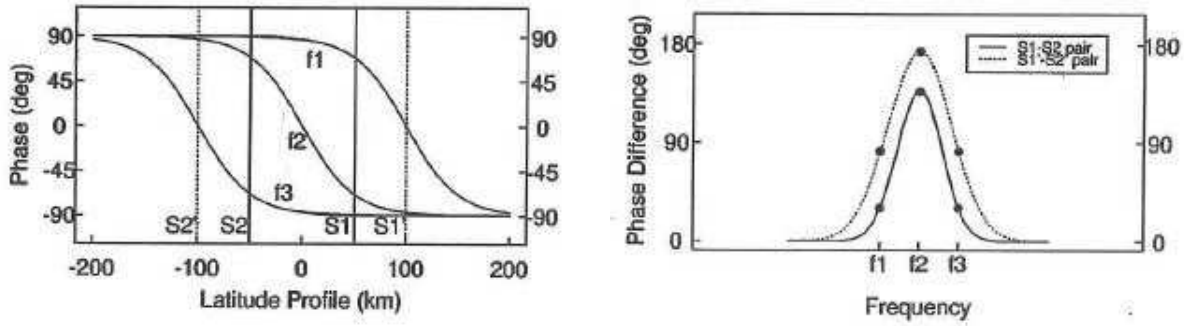

(a) (b)

Figure 4.16: *An illustration of how the phase differences arise between stations on the same magnetic meridian. a) The top panel shows the phase as a function of latitudes for three examples of resonant L-shells with resonant frequencies f_1, f_2, and f_3. b) plot of the phase difference between the signals observed at the two stations (adopted from Chi and Russell, 1998).*

tudes of the two stations, both driven by a pump wave (Chi and Russell, 1998). However, Chi and Russell (1998) explain the crossphase in terms of field line resonance theory. They showed that the original field line resonance theory and the ionospheric effects on pulsation signals can explain the properties of the crossphase spectrum of pulsations. They also showed why the simplified oscillators model has limited capability in interpreting pulsation observation e.g. failing to interpret the crossphase spectrum for the Z-component where pulsation can exist if the Earth is considered to have a finite conductivity. Chi and Russell (1998) used field line resonance theory and the ionospheric model of Hughes and Southwood (1976) to illustrate how the phase difference arises between two stations on the same meridian. They considered a scenario of several resonances with resonant frequencies f_1, f_2, and f_3. Figure 4.16(a) plots their phase predicted by FLR theory as a function of latitude. The phase difference of the signals measured by the two stations, S_2 and S_1 may be read off the left hand scale and is plotted in Figure 4.16(b). The size of phase difference depends on the station separation relative to the scale size for the phase change in the ionosphere (e.g. Chi and Russell, 1998). Chi and Russell's (1998) pulsation ground measurements were consistent with this interpretation where they observed phase difference between two stations increasing as the station separation in the meridian plane increases. The two oscillator model of Waters et al. (1991a) differs from the conventional field line resonance model (Chi and Russell, 1998) which has a phase change of 180^0 across any resonating L-shell. The amplitude difference and crossphase spectrum methods were both used in this study to determine the presence of a field line resonance.

4.7 Summary

In this chapter the reader was introduced to FFT linear and nonlinear MESA methods. The two were used to compute spectral estimates for an idealized Pc3 geomagnetic pulsation. The FFT method is used in Blackman-Tukey and periodogram methods where the spectral density is given by the absolute value squared of the Fourier transform of the time series. In these methods an unfounded assumption is made by the extension of the data outside the available range which result in a setback when analyzing short data records. To obviate this unfounded assumption of linear methods a nonlinear MESA method is used. This was experimented with using 600, 90 and 30 second test signals and it was shown that FFT spectra for short signals result in poorly resolved spectra. The MESA method is capable of determining the spectral estimate for short signals, but it is important to use correct PEF length. A PEF length value which is at least 10 percent of the value of the total signal duration was found to be best. An optimal length is dependent on the noise level present on a signal (Chen and Stegen, 1974). In the current study it was established that for a pure signal the shorter length is preferable, whereas for signals contaminated with noise a longer length is preferable.

We also introduced the crossphase technique, which is an effective tool to identify the field line resonance frequencies. The crossphase spectrum of the magnetic fields at two closely located stations on the same meridian provides a powerful tool to identify the eigenfrequencies of the magnetospheric field lines in the magnetosphere.

The PEF length values established in this chapter are applied in the next chapters when using the MESA method and the crossphase technique will be used to facilitate the detection of the field line resonances. In the next chapter the structures of Pc3's observed at low latitudes is studied by comparing ground and CHAMP satellite magnetic field measurements.

Chapter 5

The Structure of Pc3 Pulsations Observed at Low Latitudes on the Ground and by CHAMP

5.1 Introduction

In this chapter the structure of low-latitude Pc3 pulsations is studied by comparing ground and satellite magnetic field measurements. The main objective is to understand the coupling between the fast and Alfvén modes and the propagation of Pc3 pulsations between the magnetosphere and the ground. This was accomplished by comparing the frequency structure in spectra of the field aligned and transverse components in the ionosphere and the H- and D-components on the ground and investigating ionospheric rotation. Induction magnetometer data from Hermanus (HER) and Sutherland (SUT) stations in South Africa are used in conjunction with low Earth orbiting CHAMP satellite observations. This chapter presents a Pc3 event observed on 15 February 2003 at time when CHAMP was passing over the ground stations.

The chapter is organised as follows: In the first section we briefly review the first CHAMP Pc3 observation. In the second section event selection and data analysis are described. In the third section the current Pc3 CHAMP observations are presented and analysed. Thereafter the results are discussed in relation to existing MHD theory and previously published results. The chapter closes by summarizing the results discussed. Parts of this chapter have been published by Ndiitwani and Sutcliffe (2009).

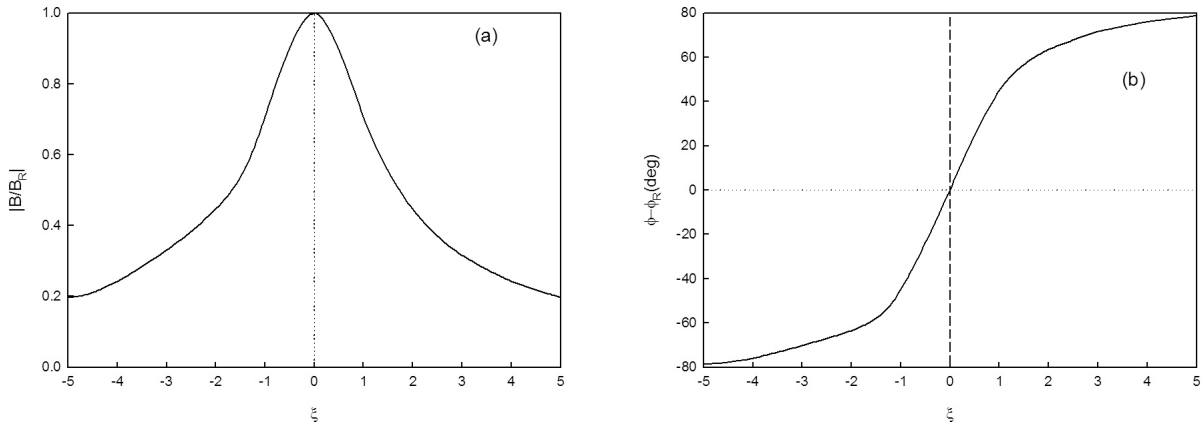

(a) (b)

Figure 5.1: *Theoretical meridional profiles of a) amplitude and b) phase of a FLR wave through the resonance region calculated by expressions given by equations 5.1 and 5.2 (after Vellante et al. (2004).)*

5.2 First CHAMP Pc3 observation

As a test of theoretical predictions, Vellante et al. (2004) compared ground and satellite signatures of a Pc3 field line resonance. They presented an analysis of a Pc3 pulsation event observed simultaneously in space by CHAMP and on the ground by the SEGMA array during a conjunction on 6 July 2002. They identified both compressional and transverse oscillations in CHAMP magnetic measurements and observed a close correspondence between the compressional component and the ground signals. The azimuthal component showed evidence for the occurrence of a field line resonance, however, the frequency of the azimuthal oscillations was 20% higher than the frequency of both the compressional and ground pulsations. They explained this difference in terms of a Doppler shift caused by the rapid movement of the satellite across the resonance region. Figure 5.1 shows theoretical meridional profiles of amplitude and phase of a FLR wave through the resonance region. The plots are shown in the range $(-5 < \xi < 5)$ where $\xi = [x - x_R(f)]/\epsilon$ is the distance from the resonance point (x_R) along the meridional direction normalised to the resonance width ϵ, and x is taken to increase toward the equator. The corresponding variations of amplitude and phase with respect to the values at the resonance point are (Green et al., 1993)

$$|B/B_R| = \left(1 + \xi^2\right)^{-1/2} \tag{5.1}$$

$$\phi - \phi_R = arctan\left(\xi\right). \tag{5.2}$$

The important point to note from the plots is that around the resonance the phase varies quite rapidly, and if a satellite like CHAMP crosses this region at high speed, the observed frequency

may be shifted with respect to the true frequency. By comparing the satellite velocity, V_{sat}, and the apparent phase velocity, V_{phase}, one can get an idea of the importance of this effect. Measurements performed by a satellite moving along x at velocity V_{sat} would be affected by a Doppler effect which determines an observed frequency (Vellante et al., 2004)

$$f_{sat}(\xi) = f(1 - V_{sat}/V_{phase}). \tag{5.3}$$

Vellante et al. (2004) also studied the effect of the ionosphere on pulsation polarization. The direct comparison of SEGMA and CHAMP pulsations showed a 90^0 rotation of the ULF wave polarization ellipse through the ionosphere.

5.3 Event selection and Data Analysis

The intended effort of this chapter is to investigate the structure of low-latitude Pc3 pulsations observed by CHAMP and on the ground, with particular emphasis on field line resonant structure. Due to CHAMP's orbit it traverses the latitudinal structure of geomagnetic field lines very rapidly (see Chapter 3). Thus, for example, for a Pc3 pulsation signal CHAMP covers a latitudinal range of 1^0-2^0 in 1 wave period. Nevertheless, previous studies have demonstrated that CHAMP data are extremely useful for studies of ULF waves (Sutcliffe and Lühr, 2003; Vellante et al., 2004; Heilig et al., 2007).

In selecting the data, instances when CHAMP traversed the southern African region, within 20^0 of longitude of HER, were determined. Both ground and satellite data were then scanned for presence of Pc3 signals. The magnetometer data were analysed primarily using Fourier and Maximum Entropy Spectral Analysis (MESA) techniques. The adequate PEF length for optimum MESA results for this study was established as 15 and 20 coefficients respectively for the ground-based and satellite data by experimenting with artificially generated signals as described in chapter 4.

CHAMP traverses the latitudinal structure of the geomagnetic pulsation field quite rapidly; consequently, the spectral content will also likely change rapidly. In order to take account of this effect we used dynamic MESA spectra computed for 90 second data lengths and progressively shifted by 10 seconds in a manner similar to that used by Vellante et al. (2004). However, our analysis differed from Vellante et al. (2004) in two important respects. Firstly, we used a shorter PEF length than Vellante, since we found that the length of 40 used by them sometimes introduced what we considered to be spurious peaks into the spectrum. Secondly, we plotted the dynamic spectra on a logarithmic scale to emphasize the oscillations at lower power levels.

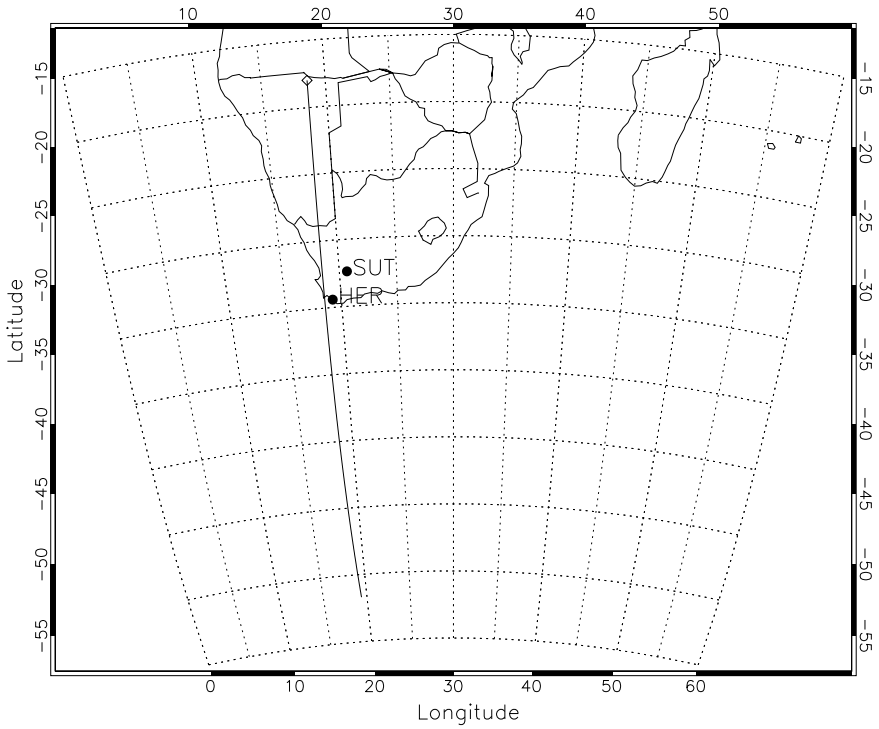

Figure 5.2: *Map of the southern African region showing the satellite-ground track as it traversed the region during a Pc3 pulsation on 15/02/2003. The locations of the two ground stations are also shown.*

5.4 Observations

On 15 February 2003 CHAMP passed close to HER in one of its orbits over southern Africa when there was good Pc3 pulsation activity. Figure 5.2 shows a map of the southern African region indicating the locations of the two induction magnetometer stations. The line across the map shows the satellite-ground track as the satellite traversed the region during 10 minutes of pulsation activity. The first point during the considered time is indicated by the diamond symbol. During the 10 minutes the satellite covered almost 40 degrees of latitude due to the low Earth orbit.

During the CHAMP traverse a Pc3 was simultaneously observed on the ground and in the magnetosphere as shown in Figures 5.3 and 5.4 respectively. Figure 5.3 shows the H- and D-components measured by the HER ground station. The components in a field-aligned coordinate system (for this coordinate system see Chapter 3 section 3.4) observed by CHAMP are shown in Figure 5.4. The data were filtered in the Pc3 frequency band, 20-100 mHz. The ground signal exhibits a wave packet structure, which is a characteristic of Pc3 pulsations. The H-component has larger amplitude than the D-component and appears rather monochromatic. The satellite data appear not to be as monochromatic as the ground data. The toroidal com-

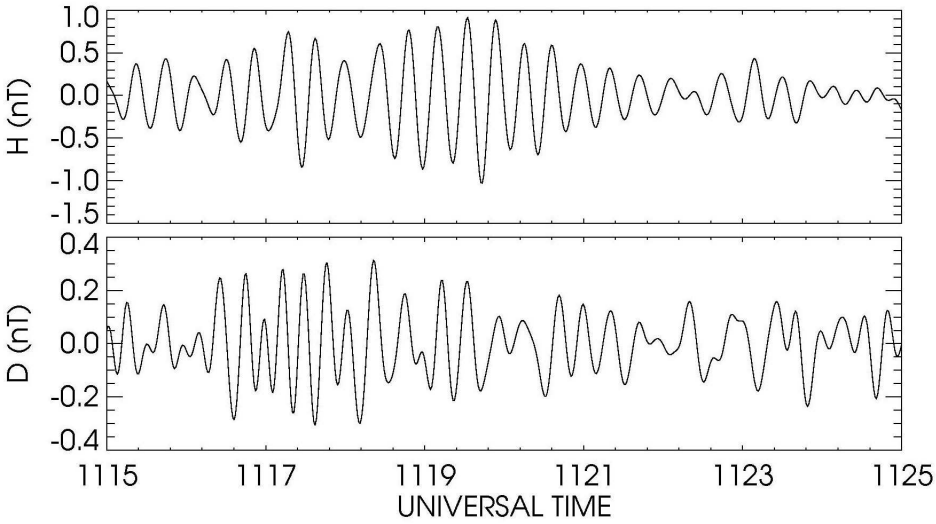

Figure 5.3: *H and D components of the Pc3 pulsation observed on the ground at Hermanus on 15 February 2003.*

ponent exhibits the largest amplitude oscillation ($\sim$ 6 nT), which maximises around 11:19 UT, suggesting that a resonance may be occurring at the time. This occurrence of a Pc3 pulsation when the satellite was crossing over HER provided an opportunity to test some of the predictions of MHD wave theory.

Figure 5.5 shows dynamic FFT spectra for the Pc3 pulsation activity observed on the ground using the HER and SUT data between 04:00 and 18:00 UT. The dynamic spectra were computed using an FFT for a 10 minute data window, which was progressively shifted by 5 minutes. The three plots from top to bottom are the log power at HER and the SUT-HER amplitude and phase difference respectively. Both amplitude and phase differences indicate the intermittent occurrence of a field line resonance throughout the day close to 50 mHz, which is a slightly higher frequency than 45 mHz where the maximum power at HER is found.

To allow for comparison of the signals observed on the ground and above the ionosphere, dynamic MESA spectra at HER and CHAMP were computed for the time of the CHAMP crossing as shown in Figures 5.6 and 5.7. The spectra were computed using a 90 second data window and progressively shifted by 10 seconds. The frequency resolution of the dynamic spectra is 1 mHz. The PEF values of 15 and 20 were used in ground and satellite data respectively. In Figure 5.6 the HER H-component spectrum clearly shows a field line resonance around 45 mHz. The D-component shows power at multiple frequencies. The slightly lower resonant frequency observed in Figure 5.6 relative to Figure 5.5 is expected since HER lies at higher latitude than the average HER-SUT latitude used to determine the resonant frequency by the

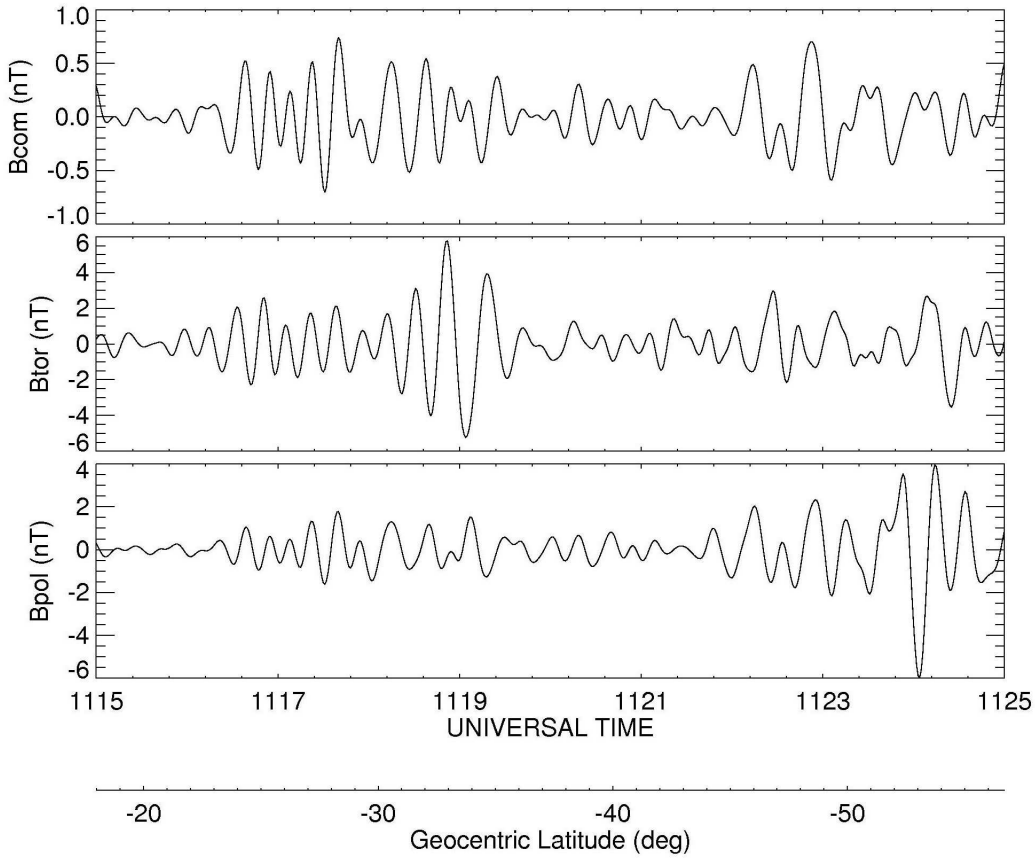

Figure 5.4: *The Pc3 signal observed along the CHAMP satellite trajectory on 15 February 2003. The three components in a field-aligned coordinate system, i.e. compressional (B_{com}), toroidal (B_{tor}) and poloidal (B_{pol}), are shown from top to bottom.*

amplitude and phase difference methods.

Figure 5.7 displays the dynamic spectra for the CHAMP data. All three components show multiple frequency structures that change over the 10 minute interval of the dynamic spectra. Similar frequency structures are observed in the compressional and poloidal components. During the first three minutes they both exhibit clear oscillations at 45 and 65 mHz. There is evidence of an oscillation at 25 mHz of which the frequency seems to increase and then decrease slightly with time. During the last three minutes there are clear oscillations at 25 and 45 mHz and evidence of an oscillation at 75 mHz.

There are similarities between the compressional (source) and toroidal (forced wave) components. However, there are differences between the first and last parts of the dynamic spectrum where toroidal mode (B_{tor}) intensities are high and low respectively. There is a short interval of intense oscillations in B_{tor} at 60 mHz centred at 11:17.5 UT when CHAMP was at geocentric

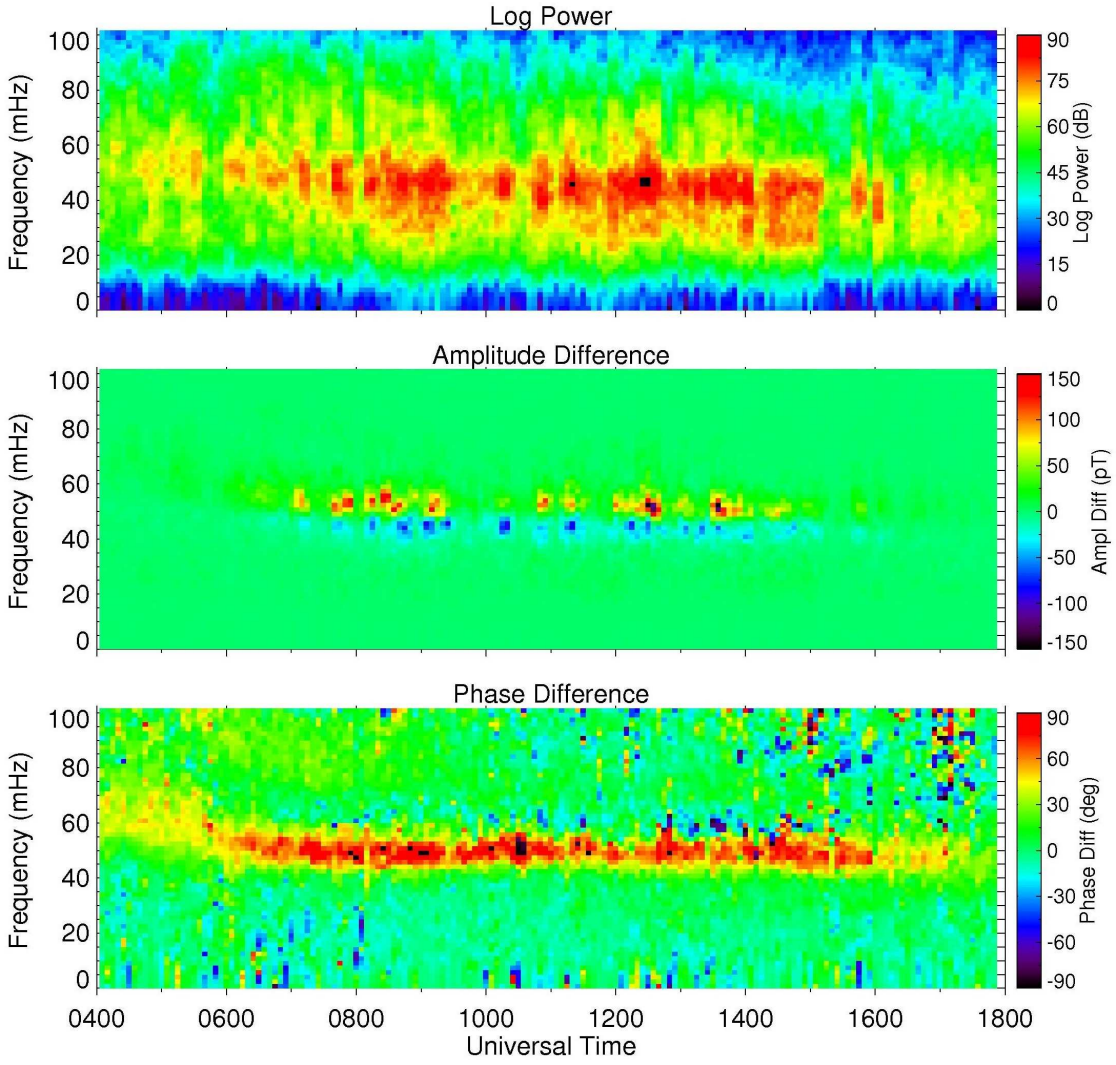

Figure 5.5: *Dynamic FFT spectra of the Pc3 pulsation H-component observed on the ground. Top panel: dynamic log power at HER, Middle panel: SUT-HER amplitude difference and bottom panel: SUT-HER phase difference.*

latitude of 27^0 south. This is followed by a short interval of intense oscillations at 40 mHz centred at 11:19 UT when CHAMP was at the geocentric latitude of 34^0 S and corresponds to the time when CHAMP was crossing close to HER. It thus appears that these high intensity toroidal mode oscillations are shifted to slightly lower frequencies relative to the fast mode oscillations at 65 mHz and 45 mHz respectively observed in the compressional component. The 40 mHz signal is also shifted to a lower frequency relative to the field line resonance oscillation observed on the ground at HER. During the last three minutes there are also clear oscillations in B_{tor} at 25 and 45 mHz and evidence of oscillations at 75 mHz. Thus, in contrast to the toroidal oscillations during the first part of the dynamic spectrum, toroidal oscillations during the second part of the dynamic spectrum do not suffer a frequency shift; they are also of a much lower intensity.

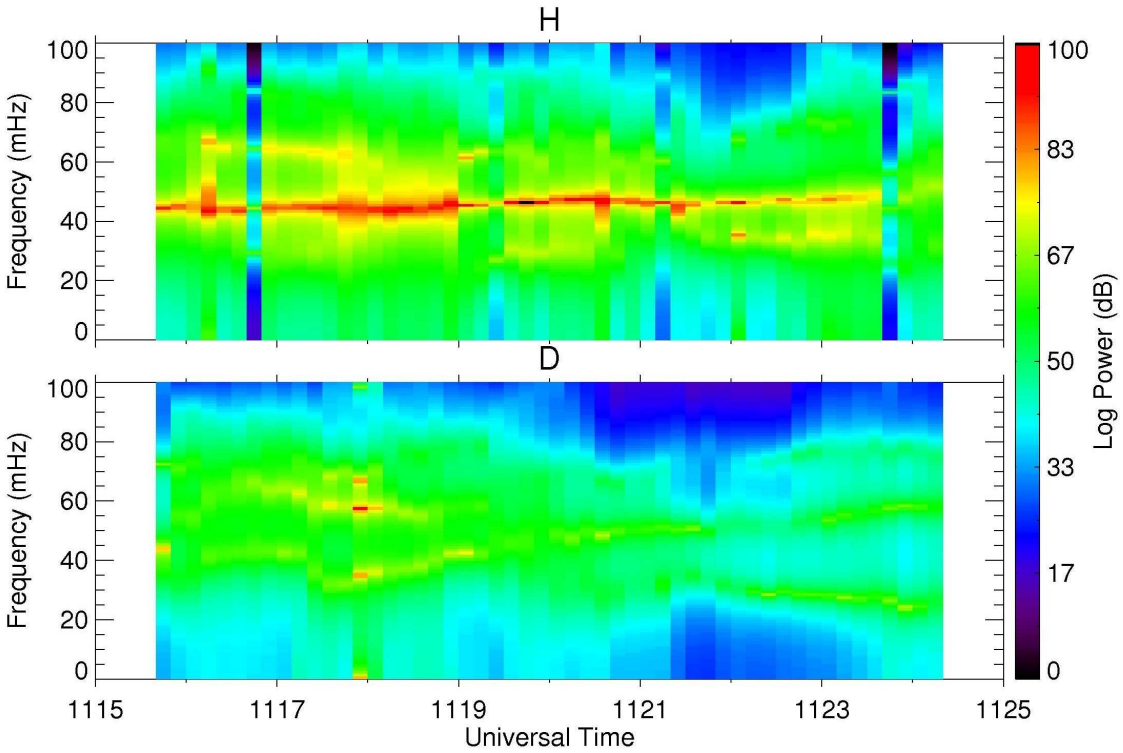

Figure 5.6: *MESA ground dynamic spectra for the H- and D-components observed at Hermanus on 15/02/2003.*

Comparison of the satellite and ground dynamic spectra exhibit similarities. The dynamic spectrum of the compressional component, B_{com}, has some similarities with the ground D-component spectrum. The three most significant frequency bands in the satellite dynamic spectrum are also observable in the ground dynamic spectrum at 75, 45 and 25 mHz. This correlation is in agreement with previous Pc3-4 observations by Odera et al. (1991); Kim and Takahashi (1999) and recently by Vellante et al. (2004). The intense oscillation in the H-component at frequency 45 mHz is ascribed to a field line resonance and manifests itself below 45 mHz in B_{tor} of the satellite dynamic spectrum. This is a consequence of the rapid motion of the satellite across the resonance region where the phase varies rapidly.

An analysis of polarization characteristics of the space and ground signals was also performed using the time series data around 11:19 UT, which is near the resonance time. This provides an opportunity to test the theoretical models of ULF wave transmission through the ionosphere. Figure 5.8 displays hodograms in the B_{pol}-B_{tor} plane for the satellite and in the H-D plane for the ground measurements for three consecutive 20 second time intervals during CHAMP's path over HER. First points are indicated by asterisks in the hodograms. The data were filtered in the frequency band 35 to 50 mHz in accordance with the dynamic spectrum observations. The

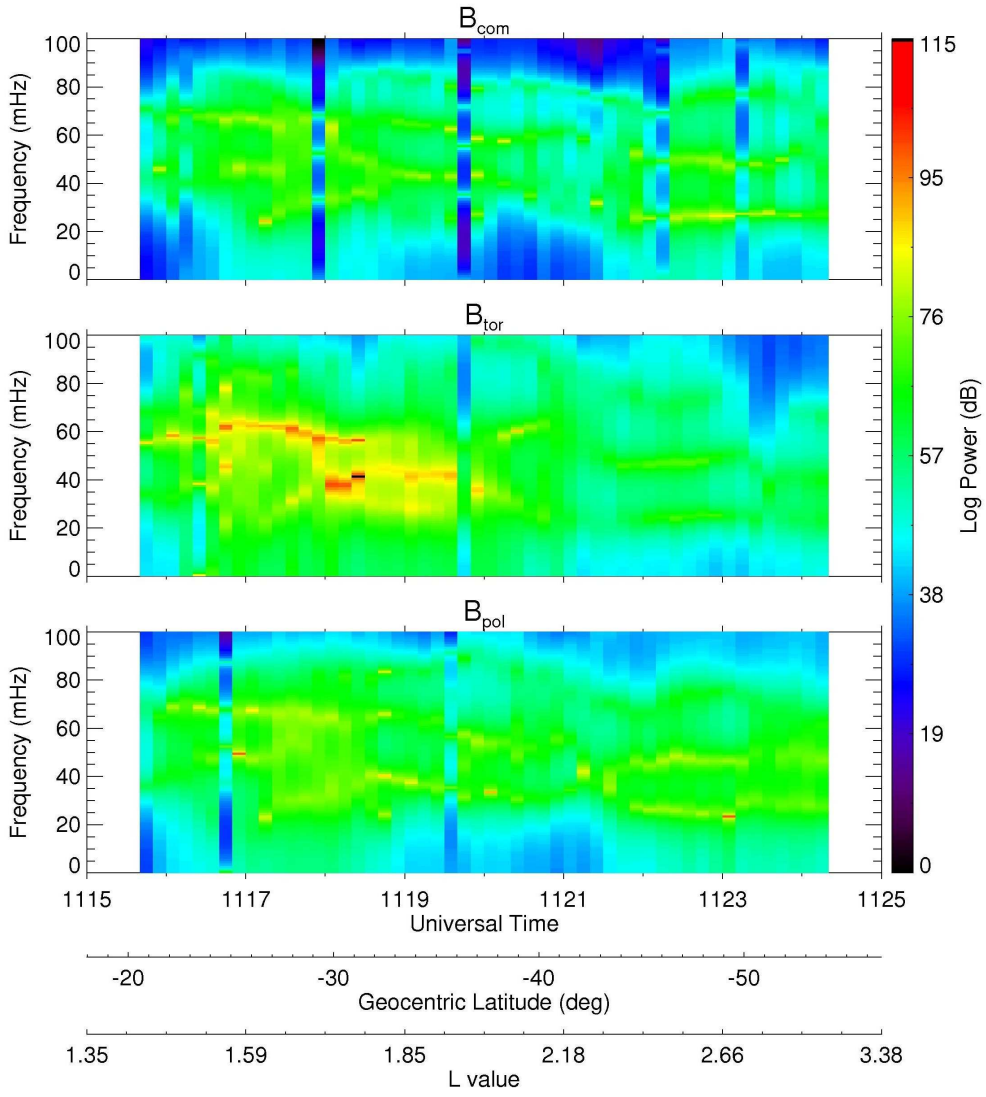

Figure 5.7: *MESA dynamic spectra for magnetic field components as measured by the CHAMP satellite on 15/02/2003. Also shown are the geocentric latitude and L-shell values during the satellite traverse.*

90^0 rotation of the magnetic field components due to ionospheric currents is clearly observable.

5.5 Discussion

In this section the observations and findings described above are discussed in the light of theoretical expectations and previous published observations. The ground FFT dynamic amplitude and phase difference spectra (Figure 5.5) indicate the intermittent occurrence of a field line resonance close to HER throughout the day. The intermittent nature of Pc3 field line resonances at low and mid-latitude ground stations was previously reported by Verõ et al. (1998).

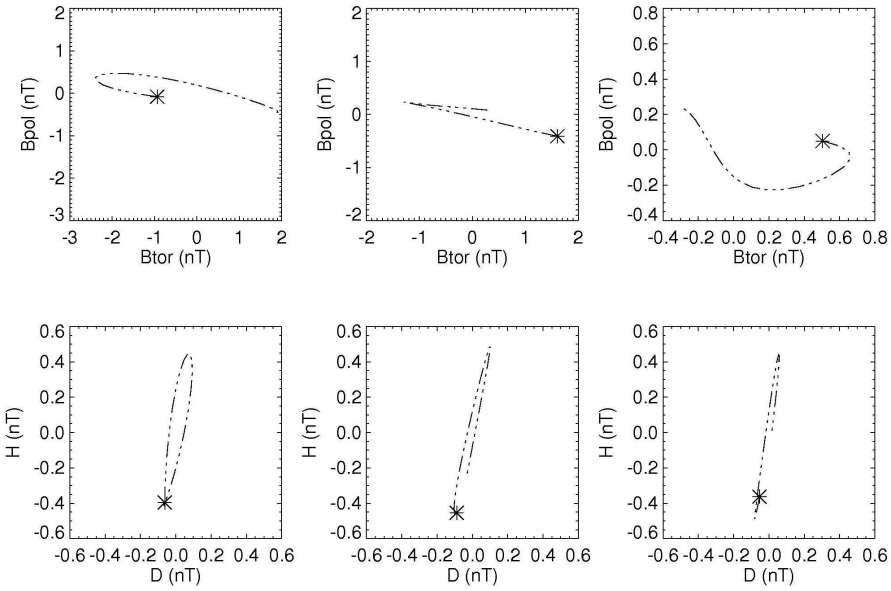

Figure 5.8: *CHAMP (top panel) and ground (bottom panel) wave hodograms for three consecutive 20 second intervals at the time when the satellite was passing over the Hermanus ground station.*

However, this discussion centres around the time when the satellite was passing over the HER ground station.

The MESA dynamic spectra for the CHAMP data show multiple frequency structures that vary with time. These variations resemble the intermittent nature and variations in period observed by Verõ et al. (1998) in UW pulsations at ground stations. The dynamic spectra show that the B_{com} and B_{pol} components tend to oscillate at similar frequencies. For example they both exhibit oscillations at 45 and 65 mHz during the first three minutes of the Pc3 event; however, the B_{pol} component decreased to 40 mHz at the time that the satellite approached the HER latitude and then decreased further to 35 mHz. During the last three minutes there are clear oscillations at 25 and 45 mHz and evidence of oscillations at 75 mHz. Consequently, our results are not in full agreement with Vellante et al. (2004), who reported the B_{pol} frequency to be 20% higher than B_{com} and which they ascribed to a Doppler effect as a result of the rapid motion of CHAMP across field lines. Our observations for the FLR driven by B_{com} at 65 mHz indicate that B_{pol} did not experience a Doppler shift. However, for the FLR driven by B_{com} at 45 mHz, the frequency of the B_{pol} component decreased at the time that CHAMP crossed over HER. In the non-uniform plasma of the real magnetosphere, the fast and transverse waves have a degree of coupling, and in such case then B_{pol} might be expected to be affected by a FLR as shown by Hughes and Southwood (1976). In their model it was demonstrated that phase variation and consequently the Doppler shift of B_{pol} around the resonance is less drastic but

can not be completely ignored. This can explain the frequency decrease of B_{pol} when CHAMP approached HER latitude. Despite the intermittent nature of the structure in the spectra and the changing latitude of CHAMP, some frequencies seem to persist, e.g. 25 mHz and 45 mHz. This is reminiscent of the results of Menk et al. (2000), who found power spectra for a ground magnetometer array to be similar over a range of latitudes.

The dynamic spectra of B_{com}, which acts as the source wave, and B_{tor}, which represents the driven or forced wave, exhibit some correlation. However, the nature of this correlation is different between the parts of the spectrum where B_{tor} intensities are high and the parts where intensities are low. The short intervals of intense oscillations, centred at 11:17.5 UT and 11:19 UT, are interpreted as times when CHAMP is crossing a field-line resonance. The observation of an apparent Doppler shift in B_{tor} frequency for the first part of the dynamic spectrum where intensities are high agrees with Vellante et al. (2004), who reported the B_{tor} frequency to be 20% higher than B_{com}. However, in our case the Doppler shift is to lower frequencies due to the satellite moving poleward rather than equatorward. In contrast with the first part of the spectrum, the last three minutes of the B_{tor} spectrum shows clear oscillations of much lower intensity at three frequencies as in B_{com} and B_{pol}. The latter are not subject to a Doppler shift. The absence of any Doppler shift at these frequencies can be explained by the oscillations not being associated with a FLR. The B_{tor} oscillations arise due to weak coupling between the fast mode and Alfvén mode waves. Note that these three frequencies are observed when CHAMP traverses magnetic shells with $L \geq 2.4$ and at these L-values the resonant frequency is expected to be < 20 mHz according to previous observations (e.g. Menk et al., 2004 and Dent et al., 2006). Consequently, the absence of a FLR and the associated Doppler shift at these frequencies is justifiable.

At low latitudes, we expect plasma density, magnetic field intensity, and field line length to vary smoothly with latitude. Consequently, the field line resonant frequency is also expected to vary smoothly and continuously as a function of latitude. However, resonant field line oscillations will only be excited at latitudes where there is a matching driving force, i.e. a fast mode wave. B_{com}, which is the signature of a fast mode wave, exhibits oscillations at frequencies 65 and 45 mHz from 11:16 to 11:20 UT. Consequently, we can expect toroidal mode oscillations to occur at these frequencies at latitudes where they match the field line resonant frequency. In Figure 5.7 we see that for a driving frequency of 65 mHz in B_{com}, this occurs at latitudes centered on 27^0 S as evidenced by the short interval of intense oscillations in B_{tor}. Note, however, that the B_{tor} frequency observed on CHAMP is Doppler shifted to a lower frequency of 60 mHz. Vellante et al. (2004) provide an explanation and derivation of this Doppler shift, which is due to the rapid rate at which a LEO satellite traverses the rapid phase change across the field line

resonance region. In the case of the example given by Vellante et al. (2004) the Doppler shift was to higher frequencies due to CHAMP moving equatorward. In our example the Doppler shift is to lower frequencies due to CHAMP moving poleward. Ninety seconds later CHAMP crossed another resonance centered at 34^0 S, where the B_{com} driving frequency is 45 mHz and the B_{tor} resonance frequency is shifted to 40 mHz as observed on CHAMP. The latter latitude is that of HER and the fast mode frequency matches the resonant frequency observed in the H-component on the ground at HER as shown in Figure 5.6.

In comparing the satellite and ground dynamic spectra we note that the compressional wave in the ionosphere has similarities with the D-component on the ground. Similar trends were also observed by Vellante et al. (2004) and confirm Odera's observations (Odera et al., 1991), who suggested that Pc3 energy is transported through compressional fluctuations. The hodograms computed confirm the 90^0 rotation of the magnetic field components.

5.6 Summary and Conclusions

In this chapter a Pc3 geomagnetic pulsation event at a time when the CHAMP satellite passed over the HER ground station was studied. The data were analysed using Fourier and MESA techniques. When a compressional wave is seen along the CHAMP trajectory, similar structures are observed in the D-component on the ground. These observations of a compressional wave in space and on the ground at the same frequency and with similar wave forms is viewed as an indicator that Pc3-4 wave energy is transported through compressional fluctuations, confirming previous observations. We observed oscillations at a number of discrete frequencies in the fast mode wave, one of which drives a field line resonance at the characteristic latitude as detected by both ground and satellite measurements. Therefore these observations confirm the compressional wave as being the driver of the field line resonance. The toroidal mode frequency observed on CHAMP experienced a Doppler frequency shift due to the rapid motion across the resonance region. Polarization hodograms in the resonance region show the expected 90^0 rotation of the magnetic field components.

Chapter 6

A Study of L-dependent Pc3 Pulsations Observed by the Low Earth Orbitting CHAMP Satellite

6.1 Introduction

References to observations of toroidal standing Alfvén mode oscillations with clearly L-dependent frequencies from spacecraft in the outer magnetosphere for $L > 3$ are limited in the literature. Such observations in the inner magnetosphere for $L < 3$, have not yet been reported in the literature.

This chapter offers three interesting case studies of ULF wave observations by the low Earth orbiting CHAMP satellite. The magnetic field measurements from CHAMP are compared to Hermanus magnetometer data for times when CHAMP crossed the ground station L-shell, namely for 7 February 2002, 13 February 2002 and 18 February 2003. For the first time observations of Pc3 toroidal oscillations with clearly L-dependent frequencies for lower L-shell values ($L < 3$) observed by an LEO satellite are reported. These observations show FLR frequencies increasing as a function of decreasing latitude down to L =1.6 and then decreasing as a result of the larger plasma density of the upper ionosphere. The L-dependent frequency oscillations were observed in the presence of a broadband compressional wave spectrum.

In the first part of this chapter a brief overview is given of L-dependent oscillations observed in the outer magnetosphere for $L > 3$. Inner magnetosphere L-dependent observations for $L < 3$ are studied in the second part of this chapter. The inner magnetosphere observations are discussed in the third section and summarised in the last section where conclusions are also drawn. Parts of this chapter have been published by Ndiitwani and Sutcliffe (2010).

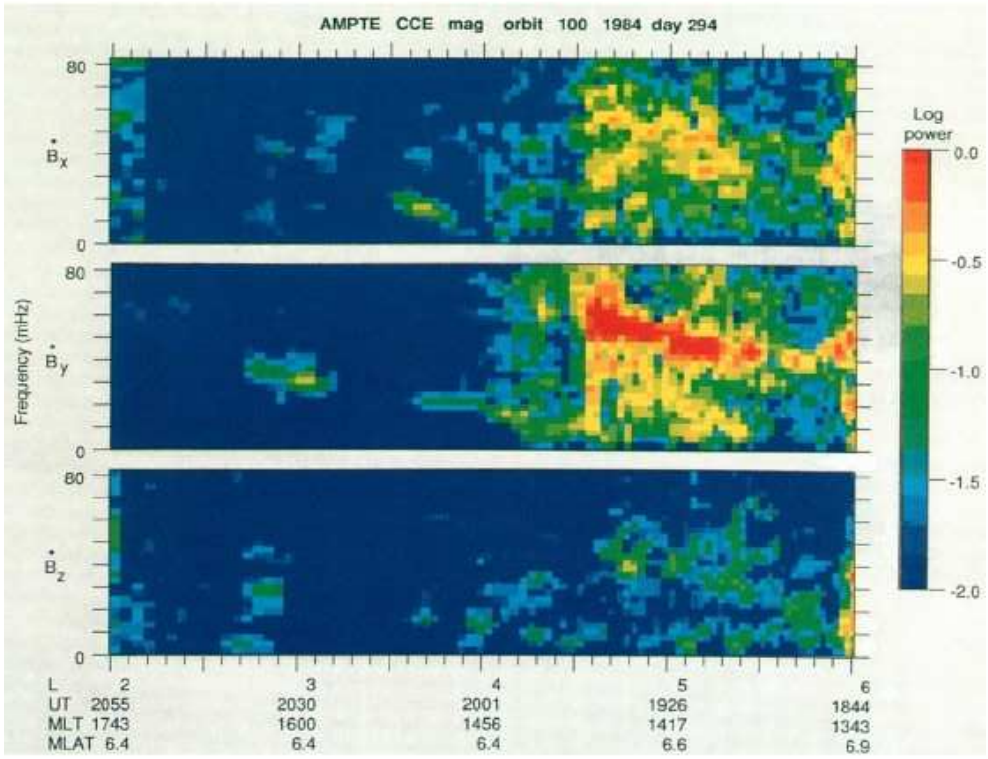

Figure 6.1: *An example of dynamic spectra from CCE magnetic field measurements. On the horizontal axes, the location from of the space craft is shown using L, Magnetic local time (MLAT) and magnetic latitude (MALT) in degrees (adopted from Takahashi et al. (1990)).*

6.2 L-dependent pulsations in the outer magnetosphere for $L > 3$

The characteristics of field line resonant oscillations excited by fast mode waves may be expected to depend on the source wave frequency content, that is, whether it is monochromatic or broad-band. Magnetic pulsations can be excited when a monochromatic source is present in the magnetosphere and the field line with eigenperiod similar to the monochromatic source resonates with maximum intensity at the L-shell value of the resonant field line (Chen and Hasegawa, 1974; Southwood, 1974). Hasegawa et al. (1983) present a theoretical discussion that supports the conjecture of a wideband source able to excite harmonics for a given field line. The Hasegawa mathematical model explains how the local field line can oscillate at its resonant frequency in response to a wideband source, the frequency spectrum of which covers the resonant frequency. This explains certain observations of magnetic pulsations where the frequency varies continuously as a function of latitude for a given event. In this study this model is employed to interpret the L-dependence of FLR frequencies for Pc3 pulsations observed on L-shells with $L < 3$. This kind of FLR structure has previously been observed in the outer magnetosphere between L = 3 and 6 by Takahashi et al. (1990) and between L = 4.5 and

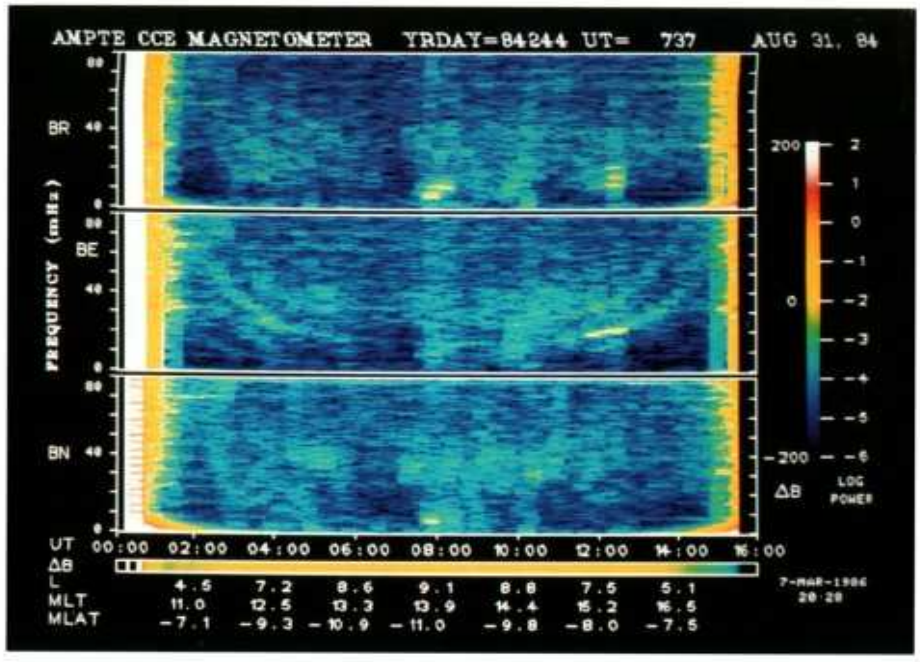

Figure 6.2: *Three dynamic power spectra of magnetic data from the AMPTE CCE satellite for a full orbit from 0019 to 1559 UT August 31, 1984 adopted from (Engebretson et al., 1987).*

9.1 by Engebretson et al. (1987).

In order to remedy the lack of observations of Pc3 magnetic pulsations in the outer magnetosphere, Takahashi et al. (1990) initiated an analysis of magnetic field data between L = 2 and 6 acquired by the AMPTE CCE spacecraft. They presented dayside pulsation activity recorded by CCE during inbound passes. The noise level of AMPTE CCE data was at least 4 times stronger for $L < 2.3$ than for $L > 2.3$. The amplitude of pulsations is expected to decrease at smaller L-shells, thus making it relatively difficult to detect pulsations at $L < 2.3$. The ability to detect Pc3-4 pulsations was made possible by averaging the highest time resolution (0.124 s) data down to nearly exactly the spacecraft spin period (5.9 s). They identified toroidal standing Alfvén wave oscillations with clearly L-dependent frequencies between L = 3 and 6. Their ability to detect small amplitudes in CCE magnetometer data led to the possibility of identifying the origin of various waves types of magnetic pulsation observed on the ground at low and middle latitudes using in situ measurements by satellites. They generated dynamic spectra using the FFT method computed for a 6-minute window progressively shifted by 1.5 min. at each step. As shown in Figure 6.1 their dynamic spectra were characterized by traces of pulsation activity with a frequency that falls with L between L = 3 and 6. Engebretson et al. (1987) observed toroidal oscillations with frequencies that decreased as a function of increasing L-shell from L = 4.5 up to 9.1 and that increased again as the satellite moved to lower L-shells for a single full orbit as shown in Figure 6.2.

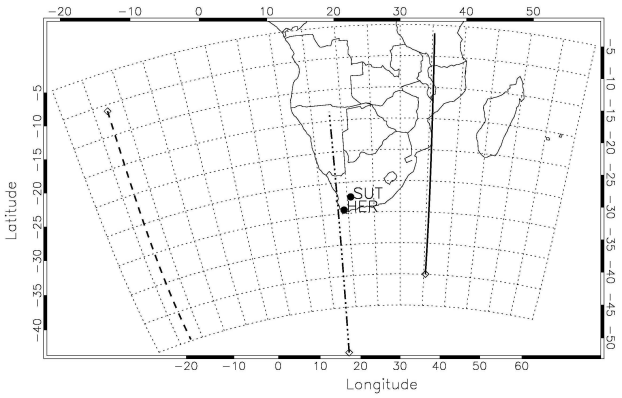

Figure 6.3: *Map of southern African and central Africa and adjacent ocean areas. Locations of Hermanus and Sutherland ground stations and the satellite ground tracks during the occurrence of three Pc3 pulsation events are also shown.*

6.3 Inner magnetosphere Pc3 observation

Menk et al. (2000) utilized a temporary 12 magnetometer ground array in Eastern Australia spanning L = 1.3 to 2.0 to investigate the variation in Pc3-4 power with latitude, the nature and low-latitude limit of FLRs, and properties of spectral components below the local resonant frequency. They employed a number of effective methods for detecting FLRs such as those described by Baransky et al. (1985, 1989) and Waters et al. (1994, 1995). They found that the resonant frequency increases with decreasing latitude up to $L \sim 1.6$ and then decreases at lower latitudes as a result of mass loading on the field line eigenfrequency due to the effect of ionospheric heavy ions at low altitudes (Hattingh and Sutcliffe, 1987).

Vellante et al. (2004) used SEGMA and CHAMP data to show that discrete Pc3 FLR oscillations are excited at low latitudes where the local resonant frequency matched that of the fast mode driver. In chapter 5 we confirmed this observation using an independent data set to study the structure of low-latitude Pc3 pulsations observed by CHAMP and on the ground. In this chapter, we continue the investigation of toroidal oscillations at $L < 3$ observed by CHAMP. However, we find that the spectral structure of the FLR oscillations differs from that reported in the previous two studies (i.e. Vellante et al. (2004) paper and chapter 5 observations published by Ndiitwani and Sutcliffe (2009)). The results in this chapter are consistent with Hasegawa's mathematical model (Hasegawa et al. 1983). They are also consistent with previous satellite observations in the outer magnetosphere from L = 3 up to 6 by (Takahashi et al., 1990) and between L = 4.5 and 9.1 by Engebretson et al. (1987). Some characteristics of the spectral structure also agree with the statistical results determined from ground observations by Menk et al. (2000). To the best of our knowledge, this study is the first to report on toroidal resonant oscillations observed at $L < 3$ with clearly L-dependent frequencies, which vary continuously

with latitude and are resolved from LEO satellite vector magnetometer data. Takahashi et al. (1990) had to adopt special techniques to detect Pc3-4 pulsations with amplitudes of only 1 nT or less. In this study, CHAMP magnetic field data of unprecedented resolution are used that make it possible to extract and resolve clear Pc3 oscillations from the data.

6.3.1 Current Observations

In this chapter we present an analysis of the Pc3 pulsation events of 7 February 2002, 13 February 2002 and 18 February 2003 for times when the CHAMP satellite crossed the HER ground station L-shell. Figure 6.3 shows a map of the southern African and adjacent ocean regions indicating the locations of two induction magnetometers for recording geomagnetic pulsations in South Africa, namely at (HER) (34°25′ S, 19°13′ E) and (SUT) (32°24′ S, 20°40′ E). This station pair can be used to facilitate field line resonance detection using the amplitude difference method of Baransky et al. (1985) and cross phase technique of Waters et al. (1991a, 1994). The three lines across the map show the CHAMP ground tracks during the three traverses, the respective paths on 7 February 2002, 13 February 2002 and 18 February 2003 are indicated by dashed-dotted, solid and dashed lines on the map. The first points during the considered times are indicated by diamond symbols. The dashed-dotted and solid lines show CHAMP moving in the direction of the equator, whereas the dashed line shows the satellite moving south poleward. In all three cases the satellite covered almost 40 degrees of latitude in 10 minutes due to the low Earth orbit, thus a rapid movement of the satellite across different L-shell regions. The continuous movement of CHAMP across these L-shells provides an opportunity to study the latitude dependence of field line resonance frequency.

Since the prime objective of this work is to study FLRs, we use well established techniques to demonstrate the presence of FLRs in the ground-based data prior to considering them in combination with the satellite data. Figure 6.4 shows the amplitude difference and crossphase plots for the event on 13 February 2002 (discussed in detail below) that occurred between 07:25 and 07:35 UT. The top panel shows the amplitude spectra at HER (dashed line) and SUT (solid line). The HER spectrum exhibits a peak centered at $\sim$ 35 mHz. The SUT spectrum exhibits two peaks at $\sim$ 35 and $\sim$ 42 mHz. The bottom two plots are the SUT-HER amplitude and phase difference respectively. Both amplitude and phase difference techniques identify FLR occurring close to 37 mHz. This is in agreement with the dynamic cross-phase spectrum (not shown) that indicated FLR frequency of 40-35 mHz between 06:00 and 18:00 UT.

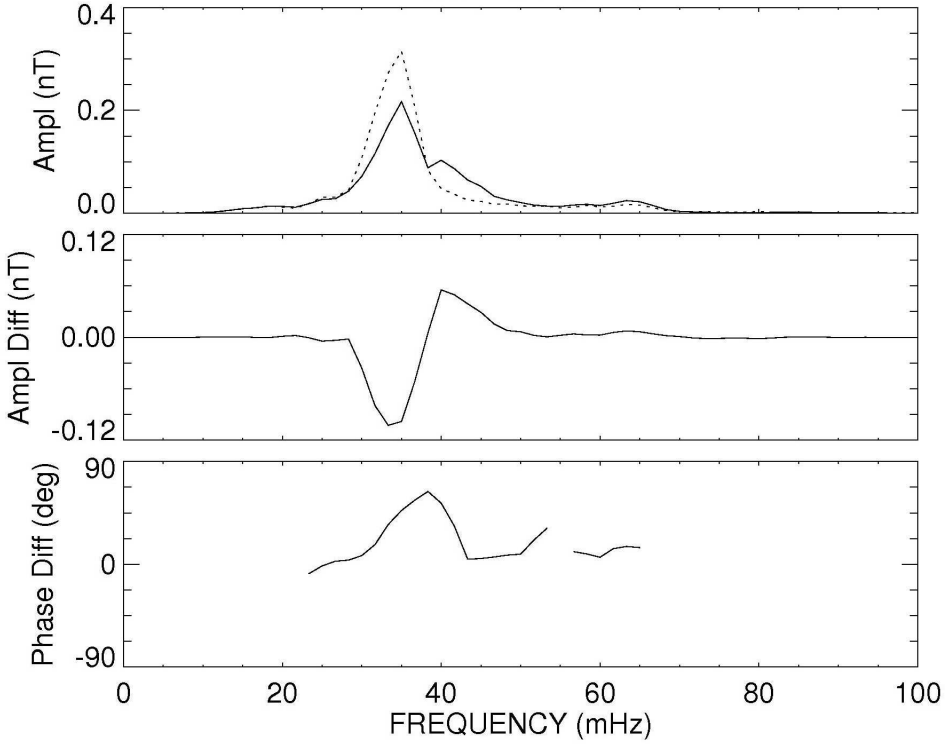

Figure 6.4: *The spectrum of the Pc3 pulsation H-component observed on the ground for the 13 February 2002 event that occurred between 07:25 and 07:35 UT. Top panel: Amplitude spectra at HER and SUT, Middle panel: SUT-HER amplitude difference and bottom panel: SUT-HER phase difference*

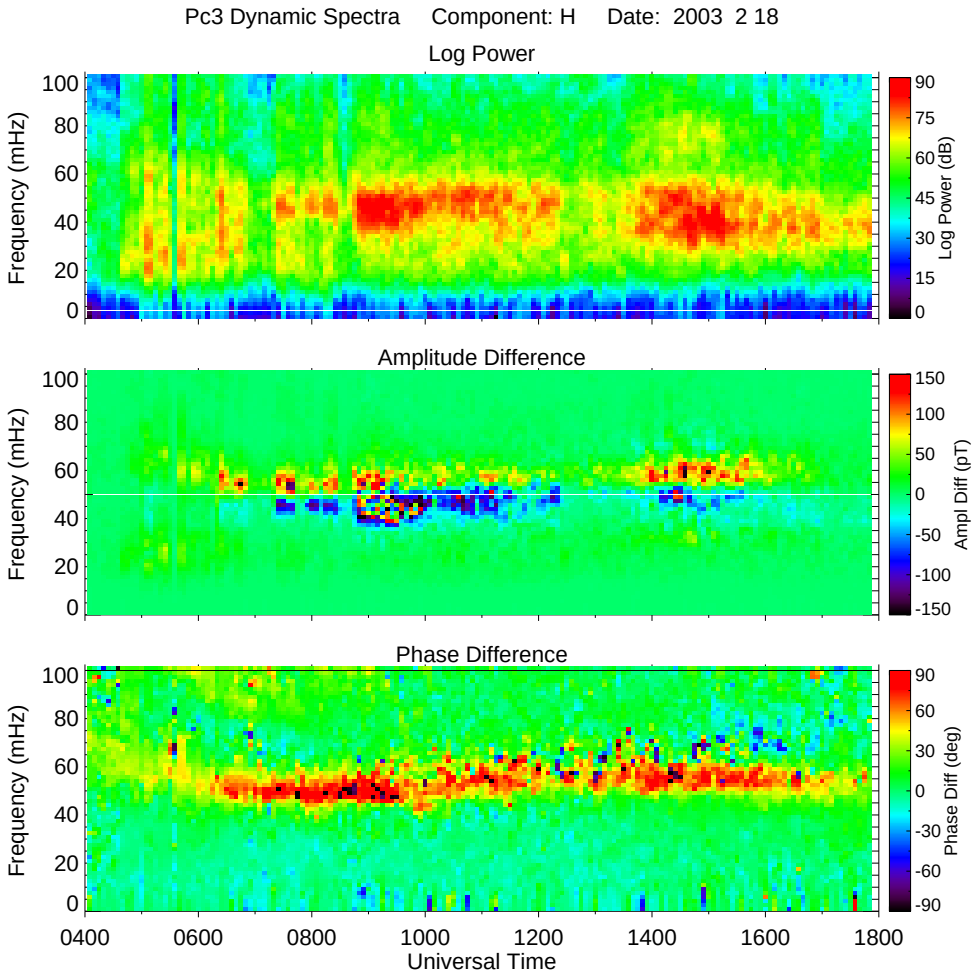

Figure 6.5: *The amplitude difference and cross-phase dynamic spectrum for the H-component for the station pair in Figure 6.3 during 18 February 2003. The top panel shows dynamic log power at HER.*

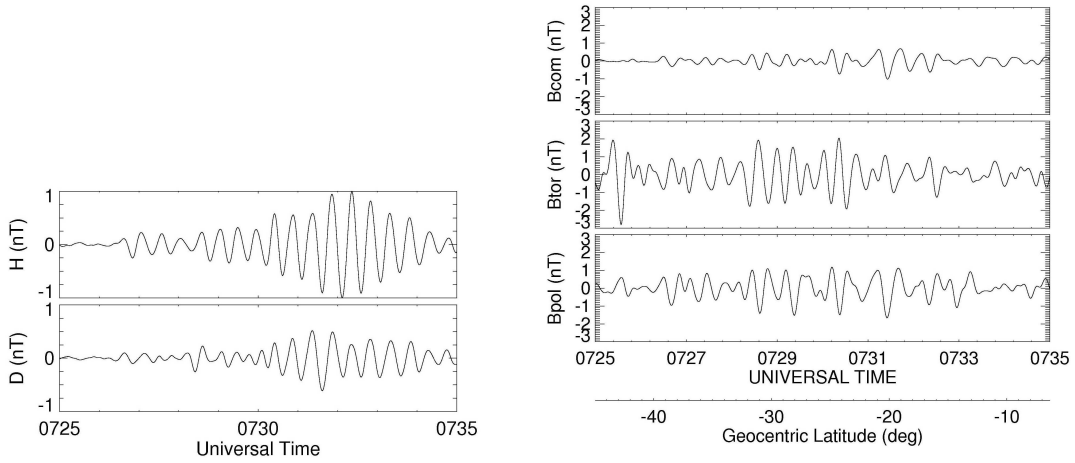

(a) (b)

Figure 6.6: *The pulsation signals observed simultaneously on ground and along CHAMP trajectory. (a) H and D components of the Pc3 pulsation activity observed on the ground on 13 February 2002. (b) A Pc3 signal observed along the CHAMP satellite trajectories on 13 February 2002. The CHAMP vector magnetic field components are in field-aligned coordinate system i.e. compressional (B_{com}), toroidal (B_{tor}) and poloidal (B_{pol}), from top to bottom.*

6.3.2 Event 1

The first event considered occurred on 13 February 2002 between 07:25-07:35 UT. During this time a Pc3 was simultaneously observed on the ground at HER and in the upper ionosphere along the CHAMP trajectory as shown in Figures 6.6(a) and 6.6(b) respectively. Figure 6.6(a) shows H- and D- components as measured by the Hermanus ground station. The components in a field-aligned coordinate system observed by CHAMP are shown in Figure 6.6(b). Also shown is the geocentric latitude axis which illustrates the change of latitude over a given time. These time series signals were filtered in the Pc3 frequency band, 20-100 mHz. The ground signal appears quasi-monochromatic and the H-component has a larger amplitude than the D-component. The satellite data appears to be more broadband. The B_{tor} exhibits larger amplitude than both the B_{com} and B_{pol} components.

In order to facilitate comparison of the ground and satellite data, dynamic MESA spectra of both data sets were computed using a 90 second data window shifted by 10 seconds as shown in Figures 6.7(a) and 6.7(b) for ground and satellite respectively. The frequency resolution of the dynamic spectra is 1 mHz. The prediction error filter (PEF) length values of 15 and 20 determined experimentally by Ndiitwani and Sutcliffe (2009) given in chapter 4 were used for ground and satellite data respectively. Additional geocentric latitude and L-value axes are

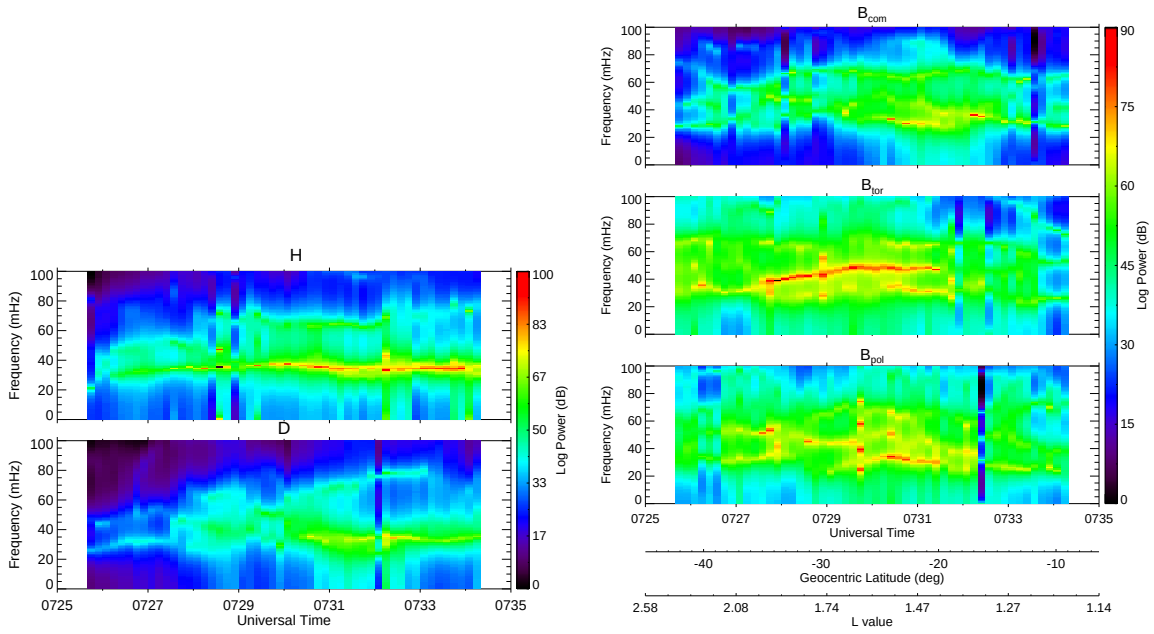

(a) (b)

Figure 6.7: *MESA dynamic power spectra for magnetic components observed on 13 February 2002 (a) on the ground at Hermanus and (b) along CHAMP trajectory. Also shown are the geocentric latitude and L-shell values for the satellite traverses.*

added to the CHAMP dynamic spectra to facilitate studying the L-shell dependence of the field line resonance frequencies.

Figure 6.7(a) shows the dynamic spectra computed for the Hermanus ground data. A field line resonance (FLR) is clearly visible in the H-component with frequency centred around 34 mHz between 07:27 UT and 07:35 UT. In addition there is an oscillation of much lower power at 65 mHz from 07:29 to 07:32 UT. The FLR frequency also appears visible in the D-component between 07:30 UT and 07:35 UT. In addition, there are weaker bands of oscillation at other frequencies.

The dynamic spectra of CHAMP data displayed in Figure 6.7(b) exhibit multiple frequency structures that change over the 10-minute interval of the dynamic spectra. The most noticeable aspect observable for all components is increased power in the band of frequencies between about 20 and 70 mHz. There are similarities observable between the more intense structures in the compressional (B_{com}) and poloidal (B_{pol}) components. An important feature in B_{com} is the broadband frequency structure of enhanced intensity between 30 and 60 mHz, increasing to 70 mHz, between 07:26 and 07:33 UT.

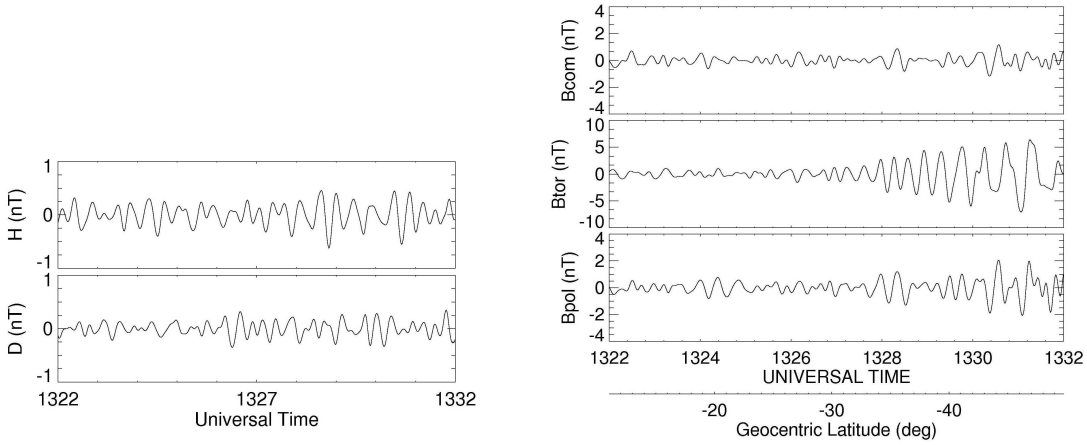

(a) (b)

Figure 6.8: *The pulsation signals observed simultaneously on the ground and along the CHAMP trajectory. (a) H and D components of the Pc3 pulsation activity observed on the ground on 18 February 2003. (b) A Pc3 signal observed along the CHAMP satellite trajectory on 18 February 2003.*

The most outstanding feature in the toroidal component (B_{tor}) is an intense oscillation starting at 30 mHz at about 07:27 UT that increases to a maximum of 50 mHz at about 07:30 UT, when the satellite reaches a shell value of $L \sim 1.6$ and then decreases slightly. In addition there are oscillations at 30 mHz and 65 mHz which can be ascribed to coupling with fast mode oscillations. The satellite crossed the latitude of the Hermanus ground station at about 07:28 UT.

6.3.3 Event 2

The second case study considers the event that occurred between 13:22-13:32 UT on 18 February 2003. Figure 6.8(a) shows 10 minutes of the HER H- and D- component time series. The signal exhibits a non-wave packet structure with H-component amplitude slightly larger than the D-component. The corresponding satellite signal shown in Figure 6.8(b) exhibits a broadband structure as was the case for the first event considered. The B_{tor} again exhibits larger amplitude compared to the other two components (note the larger amplitude scale). The prominent feature of the B_{tor} signal is the increase of amplitude as the satellite moves from low to high latitudes.

The oscillation frequencies of the signals can be viewed from the MESA dynamic spectra shown in Figures 6.9(a) and 6.9(b) for ground and CHAMP signals respectively. In Figure 6.9(a) the HER H-component shows two prominent frequency bands of similar intensity. The upper band oscillates at a frequency of about 50 mHz. The lower band varies in frequency around 35 mHz

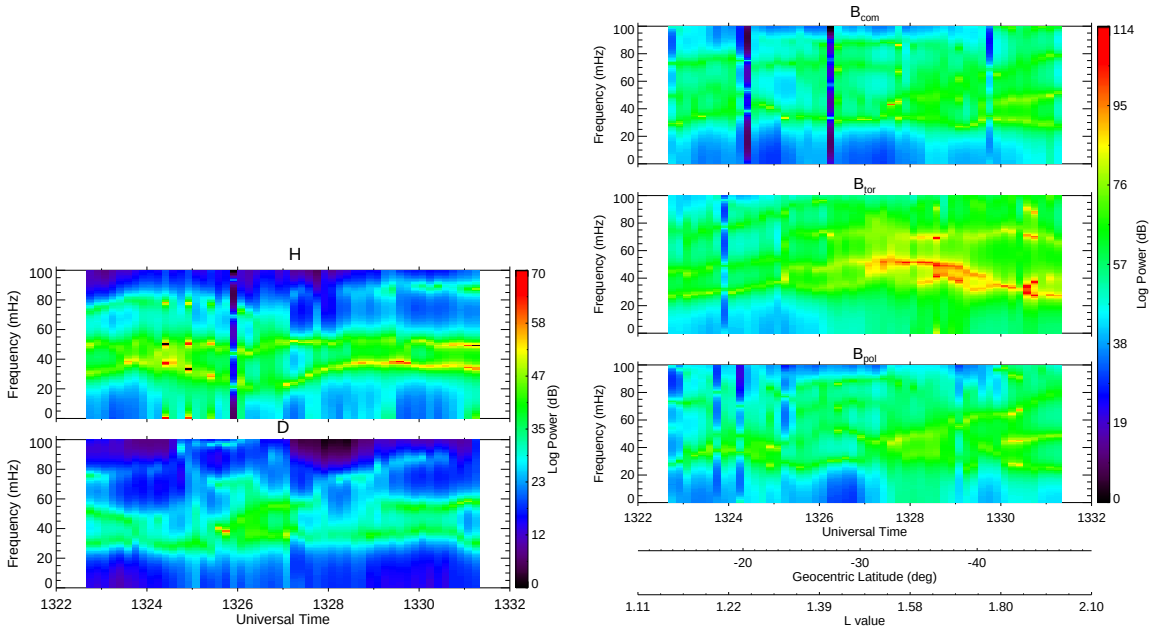

(a) (b)

Figure 6.9: *MESA dynamic power spectra for (a) data plotted in 6.8(a) and (b) for data plotted in 6.8(b).*

going as low 20 and as high as 40 mHz. The upper and lower frequency bands are respectively associated with FLR and upstream wave (UW) activity. As shown in Figure 6.5 the crossphase spectrum of the HER-SUT pair indicates FLR frequency of 50-55 mHz between 06:00 and 16:00 UT on this day. This value corresponds to the field line which has its footpoint at the midpoint between HER and SUT. The upstream wave frequency can be estimated from the empirical relationship $f_{uw}(mHz) = 6\ B_{IMF}$ (Russell and Hoppe, 1981; Yumoto et al., 1984). The magnetic field intensity B_{IMF} observed during the course of this event from the ACE satellite (taking into account the propagation delay from ACE to the magnetopause) was $\sim$ 6.2 nT. Therefore, the value of the empirical relationship $f_{uw} =\sim$ 37 mHz is close to the frequency value of the band associated with UW. The solar wind conditions on this day, i.e. high solar wind velocity and small cone angle, were conducive to intense UW activity (B. Heilig, private communication, 2009). The UW activity frequency also appears visible on the D-component lower band that oscillates at frequencies between 30 and 40 mHz. There is also evidence of oscillation at other higher frequencies.

The dynamic spectra for the CHAMP components in Figure 6.9(b) show multiple frequency structures changing over 10 minutes. This is reminiscent of the first event considered and the results in chapter 5. The fast mode components, B_{com} and B_{pol}, exhibit a broadband frequency structure and a number of clear discrete frequency bands around 30, 40, 75, and 85 mHz. The most outstanding feature of B_{tor} occurs when the satellite is located between L = 1.3 and 2.1.

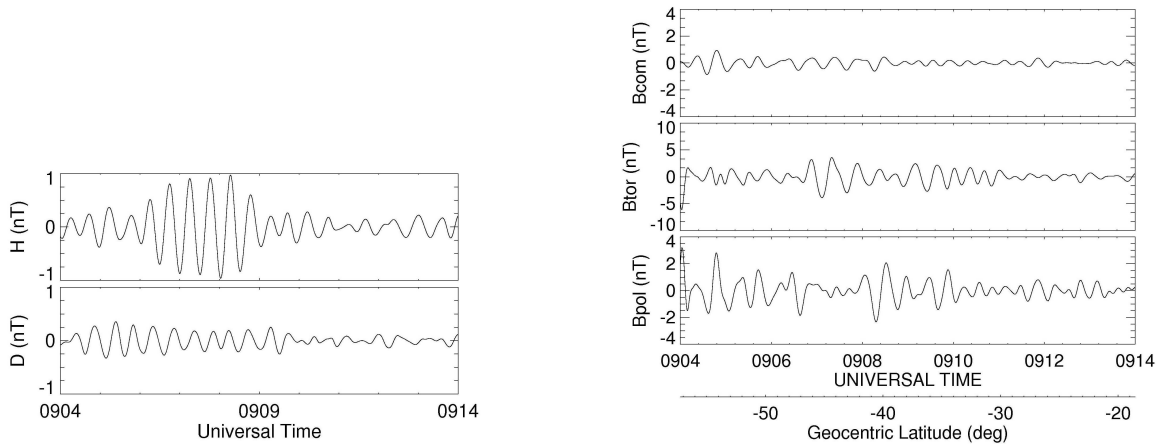

(a) (b)

Figure 6.10: *The pulsation signals observed simultaneously on the ground and along the CHAMP trajectory on 07 February 2002. (a) H- and D- components of the Pc3 pulsation activity observed at Hermanus. (b) A Pc3 signals observed along the CHAMP satellite trajectory.*

There is oscillation centered at 45 mHz around 13:26 UT when satellite crossed L $\sim$ 1.4 and which increases as a function of L-value to a maximum of 52 mHz at 13:28 UT when the satellite approached L $\sim$ 1.6. After the satellite crossed L $\sim$ 1.6 the toroidal resonant frequency decreases with increasing L-value to about 27 mHz at 13:31 UT and L $\sim$ 2.1.

6.3.4 Event 3

The third case study considers the 07 February 2002 event that occurred between 09:07-09:14 UT as shown in Figure 6.10. Shown in Figure 6.10 are Pc3 events observed simultaneously on the ground at HER and along CHAMP trajectory. Figure 6.10(a) shows ground signal that exhibits typical characteristics of Pc3 pulsation activity; namely a wave packet structure and higher H-component amplitudes than D-component amplitudes. The H-component signal appears quasi-monochromatic. The corresponding satellite signal is shown in Figure 6.10(b). The CHAMP signal is broadband as was the case in the other events studied.

Ground MESA dynamic spectra confirms a quasi-monochromatic behaviour depicted by the HER time signal (see Figure 6.11(a)). In Figure 6.11(a) a FLR is clearly visible in the H-component with frequency centred around at 35 mHz between 09:04 and 09:10 UT. As shown in Figure 6.11(b) the dynamic spectra for the CHAMP data show B_{com} and B_{pol} oscillating at similar frequencies although B_{pol} intensities are higher. In this event B_{tor} exhibit both latitude dependent and independent oscillation frequency bands which are associated to FLR and UW

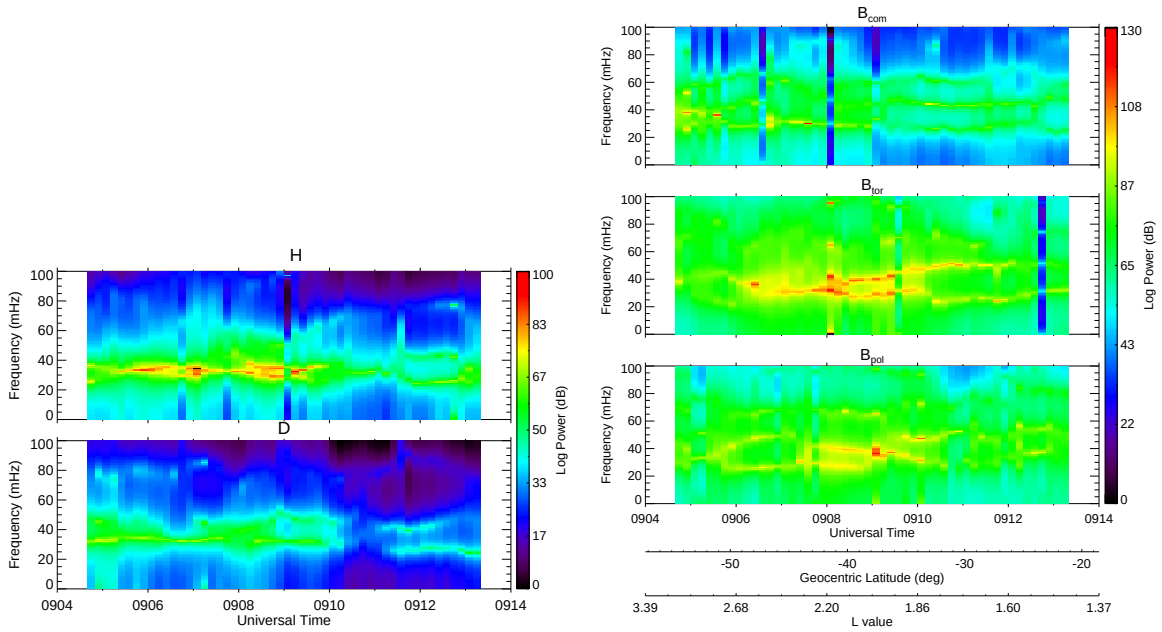

(a) (b)

Figure 6.11: *MESA dynamic spectra for magnetic components (a) measured on the ground and (b) by the CHAMP satellite.*

activities respectively. The latitude independent band is centred around 30 mHz. The UW frequency can be estimated by the empirical relationship $f_{uw}(mHz)$ = 6*IMF(nT). On this date during the period considered the mean magnitude of IMF was 5 nT (as obtained from OMNI data set), corresponding to an upstream wave frequency of 30 mHz according to the empirical relationship. The most outstanding feature of B_{tor} is the intense oscillation that starts to increase at about 09:08 UT as a function of decreasing L-values to a maximum of 53 mHz at $L \sim 1.6$.

6.4 Discussion

In the previous section frequency structures, which indicate the presence of L-dependent field line resonance were identified using ground-based and LEO satellite data. In this section the observations are discussed in the light of MHD theoretical models and previously published field line resonance observations. We presented three Pc3 pulsation events characterised by a broadband compressional source spectrum and toroidal resonant oscillations with clear continuous L-dependent frequency.

At low latitudes, plasma density, magnetic field intensity and field line length vary smoothly with latitude. Consequently, the field line resonant frequency is expected to vary smoothly and continuously as a function of latitude. In our results the inner magnetosphere CHAMP

observations show this clearly for $L < 3$. The resonant field line oscillations are excited where there is a matching driving force, i.e. a fast mode wave. In all three events studied fast mode signatures which exhibit broadband frequency structures able to drive a broad band of FLR toroidal mode oscillations, were observed in the compressional component spectra. In event 1, the beginning of this behaviour was observed shortly before CHAMP crossed the Hermanus L-shell (i.e. $\sim$ 1.8) with a frequency of 30 mHz observed on CHAMP. In Figure 6.7(b) we see that the FLR frequency in the B_{tor} spectrum noticeably increased with decreasing latitude, reaching a maximum of 50 mHz when the satellite reached L $\sim$ 1.6 and then remained constant. According to the dayside cavity model of Waters et al. (2000), (which invokes the usage of realistic profile of Alfvén velocity of Lee (1996) that depends on the radial coordinate and reaches a maximum at L=1.6), the FLR frequency increases with decreasing L-value to reach a maximum frequency at a particular L-shell. The frequency then decreases gradually with decreasing L-value due to the increase in plasma density caused by heavy ions such as O^+. Menk et al. (2000) observed this L-value to be L $\sim$ 1.6 in agreement with the cavity model and current results. In our observations the apparent decrease of FLR frequency due to the effect of heavy ions is particularly noticeable in the second case study. In Figure 6.9(b), before the satellite crossed L $\sim$ 1.55 at 13:27.5 UT, the FLR frequency was observed to increase with the increase in latitude.

In event 3 the toroidal dynamic spectra contains UW activity and a FLR component. The upstream wave activity frequencies are independent of latitude. ULF upstream waves are driven by a wave particle interaction in the terrestrial foreshock, and as a consequence their frequency is proportional to the magnitude of the IMF. In Figure 6.12 the black line across B_{tor} dynamic spectra is the UW frequency estimated from the proportionality. It is evident that UW frequency is not changing as the satellite traverses the region but is only dependent on the IMF strength. According to the OMNI data set during this 10 minute interval the conditions were favourable for the generation of UW (i.e. high solar wind speed of 650 km/s and average cone angle of 30^0). In Figure 6.12 it is observable that between 09:06 and 09:08 UT, the FLR it is oscillating at similar frequency to that of the UW activity. After the satellite crossed L = 2.2 at 09:08 UT the frequency bands of the two component separate and the FLR frequency increases as a function of L-values to a maximum of $\sim$ 53 mHz when the satellite reached $L \sim 1.6$.

When comparing ground and satellite observations, the following was noticed: In event 1 the FLR observed on the ground at frequency 34 mHz driven by a compressional wave at the same frequency is observed at 38 mHz in the satellite B_{tor} spectrum as it crossed the HER L-shell. The difference in frequency is the result of a Doppler frequency shift caused by the rapid movement of the satellite across the resonance region. The frequency shift to higher frequencies is attributed to the equatorward motion of the satellite. In the example presented in chapter 5 the

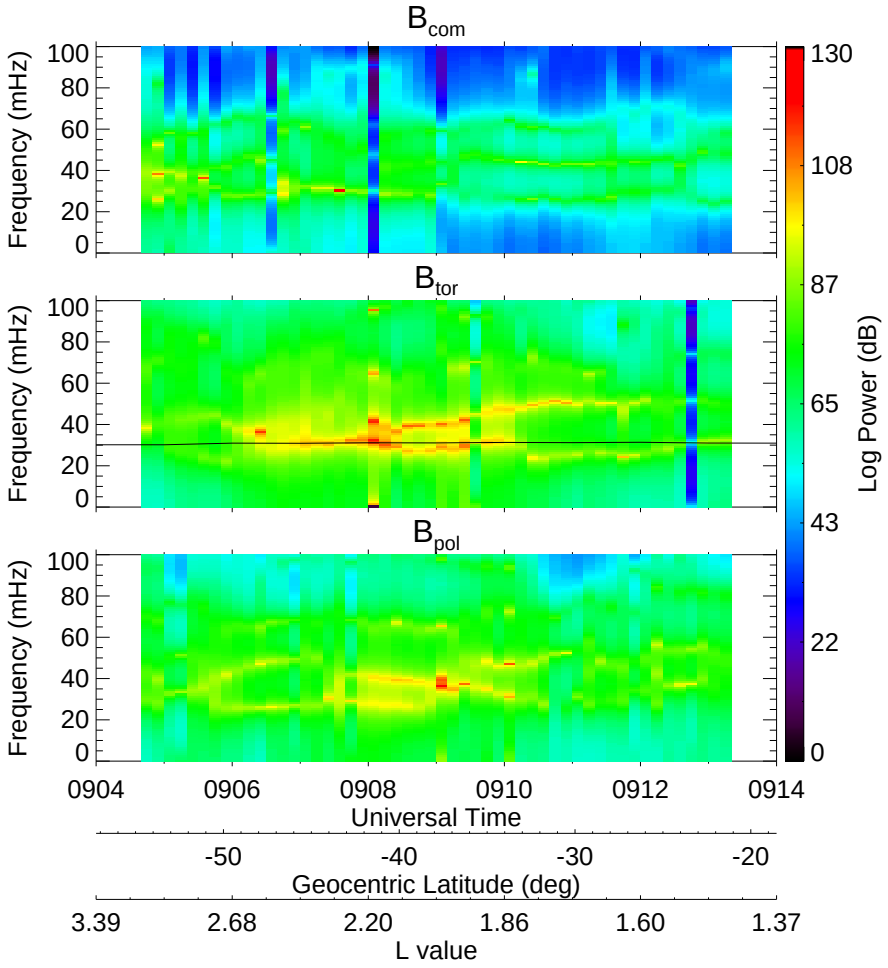

Figure 6.12: *Same as in Figure 6.9(b) but the UW frequency dependent on IMF strength is illustrated by black line plotted over the B_{tor} spectrum.*

satellite was moving poleward and the frequency shift was to lower frequencies. Vellante et al. (2004) provide an explanation and derivation of this Doppler shift effect, namely that it is due to the rapid rate at which a LEO satellite traverses the rapid phase change across the field line resonance region. In event 2, the CHAMP ground track was over the South Atlantic Ocean. Around 13:30 UT the satellite crossed the L=1.8 L-shell, where CHAMP observed a frequency of about 38 mHz, which is lower than the 50 mHz observed at the HER ground station. The Doppler shift to the lower frequency of the satellite FLR frequency with respect ground frequency is the result of the poleward motion of the satellite; however, in this case the frequency difference may also have been affected by the significant longitudinal difference between the satellite track and the Hermanus ground station. In Table 6.1 the Doppler shifts of previous and current observations are compared. In this table we specify the FLR frequencies observed on the ground and by CHAMP on crossing ground stations L-shells, the difference between the two frequencies, as well as their percentage differences. Vellante et al. (2004) observed an 18% difference whereas for the event described in chapter 5 an 11% difference is observed. In

Event	Ground frequency (mHz)	CHAMP frequency (mHz)	Difference	%Difference
Vellante et al. (2004)	55	65	+10	18
Chapter 5	45	40	-5	11
Event 1	34	38	+4	12
Event 2	50	38	-12	24
Event 3	35	45	+10	28

Table 6.1: *Comparison of the FLR Doppler shifts of different (previously published and current) events.*

Event 1 a 12% difference was observed, which is similar to the observation described in chapter 5. A significantly larger percentage difference of 24% is observed in Event 2. In event 3 a 28% difference which is in the order of event 2 is observed. The signs of the Doppler shift are consistent and depend on the direction of motion of the satellite. The reason for the differences in magnitude is not clear; however, the larger shift for Event 2 may be due to the significant longitudinal difference between the satellite track and the Hermanus ground station.

6.5 Summary

In summary, we made observations consistent with Hasegawa's et al. (1983) mathematical model of field line resonance excitation and showed examples where B_{tor} resonates with L-dependent frequency. The examples presented in this chapter differ from the observations in the previous chapter and by Vellante et al. (2004) who observed discrete FLR frequencies excited at latitudes where there was a matching driving force, i.e. a fast mode wave.

The events presented in this chapter exhibit toroidal resonant frequency increasing continuously as a function of decreasing latitude down to $L \sim 1.6$ and thereafter decreasing as a result of the larger plasma density of the upper ionosphere. This confirms that Pc3 pulsations do not always have a source with the same frequency structure. The events discussed in this chapter arise from a broad band source, while the previous results come from a narrow band source. We also presented an example of Pc3 with azimuthal perturbation spectral content that is constituted of FLR and UW frequency components.

Chapter 7

Statistical Study of FLR Occurrence

7.1 Introduction

In the previous two chapters the structure and nature of field line resonance observed at low latitudes was studied. The field line resonances observed along CHAMP trajectory were compared to ground observations. Chapter 5 presented a Pc3 event that exhibits FLR's excited at characteristic latitude where there was a matching driving frequency. In chapter 6 we presented observations of FLR with frequency changing as a function of L-shells when the source wave spectrum is broadband. This chapter reports a statistical study of event types presented in the last two chapters. The main objective was to investigate if FLR are frequently observed by CHAMP on crossing HER L-shell value.

We established a database of events scanned from a two year (2002 and 2003) data set. To avoid false interpretation of the spatial structures observed along the satellite trajectory as pulsation signals, we verified our events using ground data. According to the theoretical models such as those of Vellante et al. (2004) and observations presented in chapter 5 the frequency of FLR evident on the azimuthal perturbation is Doppler shifted with respect to the FLR frequency observable on the ground. This is as the result of the fast movement of satellite across the resonance region. The ionospheric effect on the propagation of ULF waves observable from magnetic field data is the rotation of shear Alfvén mode components. Therefore the events that constitutes the database were examined for typical FLR characteristics, which are the frequency Doppler shift and a degree of rotation between the resonant magnetic field components on the ground and satellite.

7.2 Data selection

The establishment of the event database commenced with the inspection of HER filtered 24-hour H-component magnetic field data plots. They were examined for quasi-sinusoidal oscillation characteristics. Figure 7.1 shows a 24-hour H-component plot of HER station (at L =1.8) data for 07 February 2002. The signal shown is band pass filtered in the range 10-100 mHz. This is an example of a day when typical characteristics of Pc3 waves, i.e. quasi-sinusoidal wave packet structures were clearly observed during daytime hours. The spikes observable on this data, more pronounced at $\sim$ 00:15, 01:13, 01:30, 03:33, 04:31, 05:05, 07:00 and 08:58 UT, are man made disturbances such as railway line systems. Typically, observable from the ground magnetic field data, is a mixture of FLR and fast-mode compressional perturbations. Generally, the compressional perturbations tend to have a global scale size whereas FLR oscillations are localised near the resonant latitude. Practically, using data from two adjacent stations, latitudinally separated, and taking the difference between the two data sets, the compressional waves tend to cancel out each other and thus the FLR oscillation can be extracted (Baransky et al., 1985, 1989). The difference can be either an amplitude or a phase difference. As discussed in previous chapters, in order to detect FLR, we rely on a reliable, sensitive technique, namely the phase difference method of Waters et al. (1991), often called the crossphase technique.

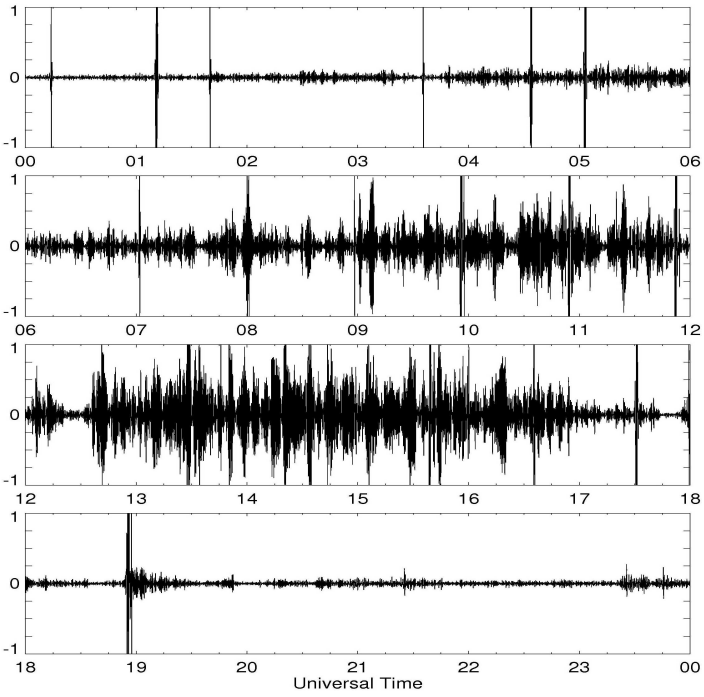

Figure 7.1: *A 24-hour H-component time-series plot of the 07 February 2002 event. Shown is the signal filtered in the Pc3 range.*

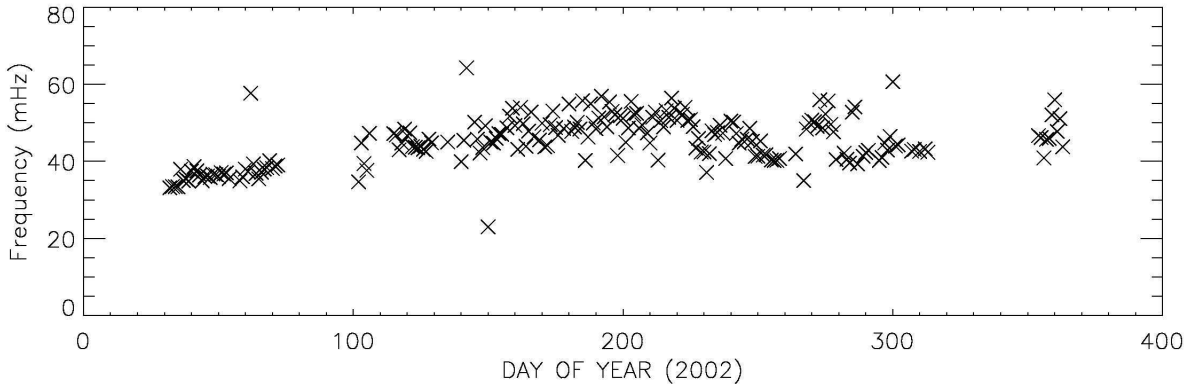

(a)

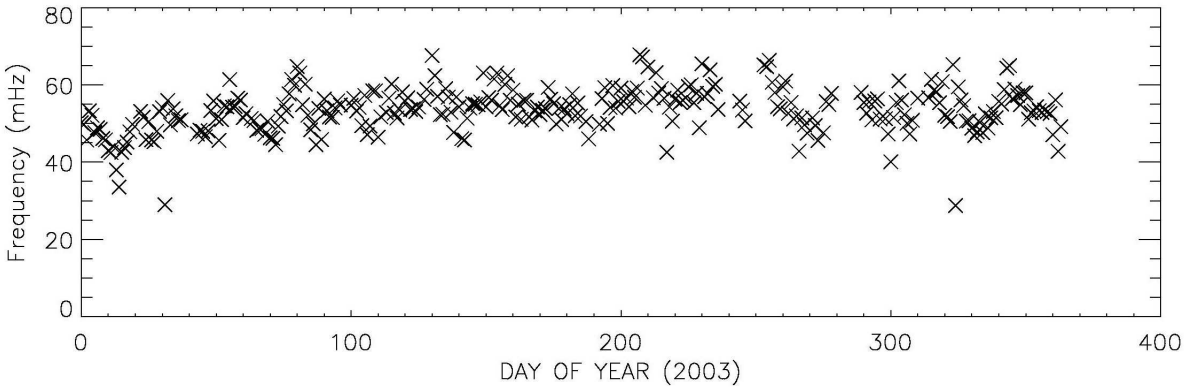

(b)

Figure 7.2: *Daytime averaged FLR frequency (f_R) values during the year a) 2002 and b) 2003.*

Therefore, the second step in establishing the database of events was the determination of the presence of FLR using the crossphase technique. The HER-SUT station pair provide the opportunity to determine the FLR frequency using this technique. The crossphase technique can be used to monitor FLR frequency on a daily basis. In this technique a peak in the H-component phase difference spectrum identifies the eigenfrequency of the geomagnetic field line that has its footpoint between the two stations. In Figures 7.2(a) and 7.2(b) daily averages of daytime FLR frequency are shown for the year 2002 and 2003 respectively.

In selecting events, instances when CHAMP traversed the Southern African region within 10^0 of longitude of HER, were determined. Figure 7.3 shows an example of the output of software used to scan events. The satellite tracks are characterised by *Start* and *End* universal time and the respective latitudinal and longitudinal co-ordinates. For each day there are daytime and nighttime tracks. We considered only daytime tracks, since at the latitudes considered for this study, Pc3 pulsations are observed during local daytime.

```
CHAMP satellite data scanned with parameters:
  Start date:     2002        2        1
  End date:     2002        2       29
  Latitude:      -34.4250    Limits:       20.0000
  Longitude:      19.2250    Limits:       10
*************************************************************************
FGM data for date:       2002        2        1
          YY  DDD:         02      032

  START UT:      9   12   43.0     Lat:   -54.37     Long:    23.68
  END UT:        9   23    0.0     Lat:   -14.39     Long:    24.20

  START UT:     21    6   42.0     Lat:   -14.48     Long:    29.02
  END UT:       21   15   36.0     Lat:   -49.10     Long:    29.23
*************************************************************************
FGM data for date:       2002        2        2
          YY  DDD:         02      033

  START UT:      9   57   54.0     Lat:   -54.42     Long:    10.96
  END UT:       10    8   12.0     Lat:   -14.40     Long:    11.49

  START UT:     21   51   52.0     Lat:   -14.45     Long:    16.31
  END UT:       22    2    9.0     Lat:   -54.43     Long:    16.84
*************************************************************************
FGM data for date:       2002        2        3
          YY  DDD:         02      034

  START UT:      9   10   14.0     Lat:   -54.40     Long:    21.56
  END UT:        9   20   32.0     Lat:   -14.39     Long:    22.09

  START UT:     21    4   11.0     Lat:   -14.47     Long:    26.91
  END UT:       21   14   28.0     Lat:   -54.48     Long:    27.45
*************************************************************************
FGM data for date:       2002        2        4
          YY  DDD:         02      035

  START UT:      9   56   55.0     Lat:   -48.30     Long:     9.23
  END UT:       10    5   39.0     Lat:   -14.36     Long:     9.40

  START UT:     21   49   16.0     Lat:   -14.45     Long:    14.23
  END UT:       21   59   33.0     Lat:   -54.47     Long:    14.76
*************************************************************************
FGM data for date:       2002        2        5
          YY  DDD:         02      036

  START UT:      9    7   36.0     Lat:   -54.37     Long:    19.49
  END UT:        9   17   54.0     Lat:   -14.39     Long:    20.01

  START UT:     21    1   30.0     Lat:   -14.45     Long:    24.85
  END UT:       21   11   47.0     Lat:   -54.48     Long:    25.38
*************************************************************************
```

Figure 7.3: *Example of output of software used to scan the satellite trajectory over the Southern African region.*

7.3 Upstream wave conditions

For a specific trajectory the OMNI data set was used to check whether the solar wind conditions were conducive to intensification of the upstream wave activity, i.e. the source of Pc3 waves. The OMNI data set contains solar wind magnetic field and plasma data from many spacecrafts in geocentric orbit and in orbit about the L1 Lagrange point $\sim$ 225 Re in front of the Earth. The OMNIWeb interface provides access to low and high resolution data. The low resolution data are averaged hourly and high resolution data set are minutes averaged data. In this work we used the one-minute OMNI high resolution data available on the OMNI website: http://omniweb.gsfc.nasa.gov. The primary use of the OMNI data set is to support studies of the effects of solar wind variations on the magnetosphere. Therefore, the data is time-shifted to the magnetosphere's bow-shock nose from the original location of the satellites. A detailed description of the processing for the correction for convection delay is available on the OMNI website. For our purpose of testing the upstream wave conditions, we extracted total IMF strength and solar wind (SW) speed as well their components. The cone angle was calculated as the arc-cos of the absolute value of the x-component of IMF (B_x) over total IMF strength (B_{total}).

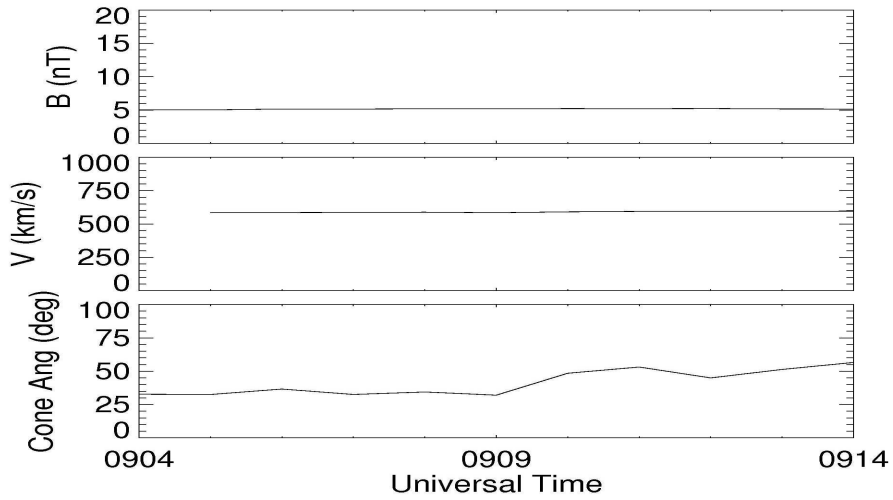

Figure 7.4: *A typical example of the upstream parameters that are suitable for the generation of upstream waves. Shown for this data set for 07 February 2002 are total IMF strength, solar wind speed and cone angle from top to bottom respectively.*

Figure 7.4 shows a typical example of the magnitude of solar wind parameters, (i.e. solar wind speed and cone angle) that favour conditions suitable for the generation of the upstream wave activity in the upstream region. Figure 7.4 also shows the IMF strength, which in our studies serves the purpose of estimating the UW frequency. ULF upstream waves are driven by a wave particle interaction in the terrestrial foreshock and as a consequence, their frequency is proportional to the magnitude of the IMF. The shown data set illustrates that in a 10-minute period (during which CHAMP can traverse the Southern African region) the IMF strength and solar wind are stable. The cone angle is the only variable of the three that varies during a 10-minute period. For the threshold cut-off we regard values established experimentally by Heilig et al. (2007) as adequate. Hence, for our statistical study we considered events observed when the solar wind speed was $>\sim$ 450 km/s and the cone angle was $\sim 50^0$ or lower.

7.4 Criteria for quantifying the FLR

The criteria used to quantify the FLR structure are the expected Doppler shift and an amount of degree of rotation of the transverse Alfvén wave components. The wave has an amplitude and a phase. Their profiles around the resonance are shown in Figure 7.5. The observed frequency of the sinusoidal wave reflects the rate of change of phase. Depending on the direction in which the satellite moves the rate of change of phase either decreases or increases. The decreasing rate is associated with the Doppler shift to lower frequency whereby the satellite data show a lower frequency compared to the ground data. The increasing rate is associated with Doppler

shift to higher frequency, and if the satellite moves across the resonance region rapidly, the observed frequency will be shifted to a higher frequency with respect to the true frequency.

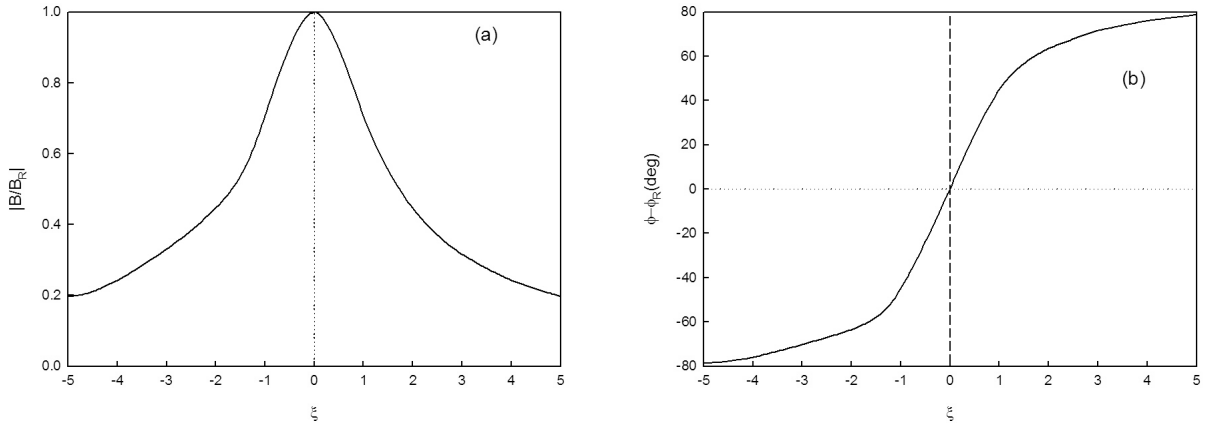

(a) (b)

Figure 7.5: *Theoretical meridional profiles of a) amplitude and b) phase of a FLR wave through the resonance region.*

Ionospheric currents cause modification to the MHD wave modes as they are transmitted through the ionosphere and the atmosphere as, for example, reported by Hughes and Southwood (1976). In the case of uniform ionospheric conductivity the magnetic signal on the ground is rotated through 90^0 with respect to the magnetic field of the transverse Alfvén mode in the magnetosphere, because the signal below the ionosphere is proportional to the Hall current (Kivelson and Southwood, 1988). Polarization hodograms in the resonance region are expected to clearly show a 90^0 rotation of the field line resonant magnetic field components. The observations in chapter 5 clearly demonstrated the 90^0 rotation of the transverse resonant magnetic field components. Glassmeier (1984, 1988) showed that for a non uniform ionospheric conductivity the previously predicted 90^0 rotation between the magnetic field below and above ionosphere does not hold generally because the rotation angle depends strongly on the conductivity gradients.

7.5 Data base

During the year 2002 when the satellite was orbiting between latitudes 15^0 S and 55^0 S within 10^0 longitude of HER, and when conditions were suitable for the generation of the upstream activity, 16 Pc3 events were identified. The date and time of events that constitute the database are shown in Table 7.1. The shown IMF, SW and cone angle magnitude values are the average of the values during the course of the event. Listed in the 6th and 7th columns are the FLR frequencies observed at the ground station and by CHAMP respectively on crossing the ground

Date	Time	BIMF	VSW	cone angle	frequency (mHz) at L=1.8		polarisation
	UT	nT	(km/s)	(deg)	HER	CHAMP	
2002 02 07	09h04-09h14	5	650	35	35	40	90^0 *rotation*
2002 02 08	08h18-08h28	5	500	15	35	42	90^0 *rotation*
2002 02 12	08h10-08h20	7	500	25	35	50	90^0 *rotation*
2002 02 13	08h55-09h05	5	500	30	35	40	Not clear
2002 02 18	08h00-08h10	8	350	25	40	50	Not clear
2002 02 21	07h08-07h18	8	450	25	36	45	Not clear
2002 03 14	05h31-05h41	6	400	45	40	45	Not clear
2002 05 29	10h27-10h37	4	550	30	40	35	Not clear
2002 06 09	10h09-10h19	7	450	35	55	45	Not clear
2002 07 13	07h17-07h27	5	450	15	50	45	90^0 *rotation*
2002 07 20	06h13-06h22	8	850	54	55	45	90^0 *rotation*
2002 10 15	10h07-10h17	13	450	50	35	45	Not clear
2002 10 19	09h47-09h57	8	750	75	40	45	Not clear
2002 10 27	09h05-09h15	7	550	46	40	45	Not clear
2002 10 29	08h54-09h04	6	510	30	40	45	Not clear
2002 12 27	15h07-15h17	7	700	35	40	45	Not clear

Table 7.1: *The 2002 events considered for statistical study. The table gives the date and time for events, solar wind parameters, frequency on the ground and observed by CHAMP on crossing the HER ground station as well the nature of polarisation characteristics.*

station L-shell. By comparing the two values, the Doppler shift, can be determined. Listed in the last column is the verdict on the polarization hodogram characteristics.

It is clear that the data coverage for the year 2002 is limited. This is attributed to poor ground data coverage. This was because for a number of days magnetic data from either HER or SUT or both were unavailable. Consequently, one can not compute crossphase spectra. Therefore, the initiative was taken to scan events from 2003 data, as shown in Table 7.2. The arrangement of the table is the same as for Table 7.1. The statistics of events listed in the two tables are summarised in Figure 7.7. It gives the classification of:

- events in terms of the satellite direction i.e. whether equatorward or poleward,
- the number of events where the expected Doppler shift was observed when the satellite was crossing the HER L-shell value.

In Tables 7.1 and 7.2 the polarisation is characterised in three ways: 90^0 *rotation*, *not clear* and *no rotation*. 90^0 *rotation* describes hodograms where 90^0 rotation of magnetic field components was observed as in chapter 5, Figure 5.8. The *no rotation* describes cases where polarisation

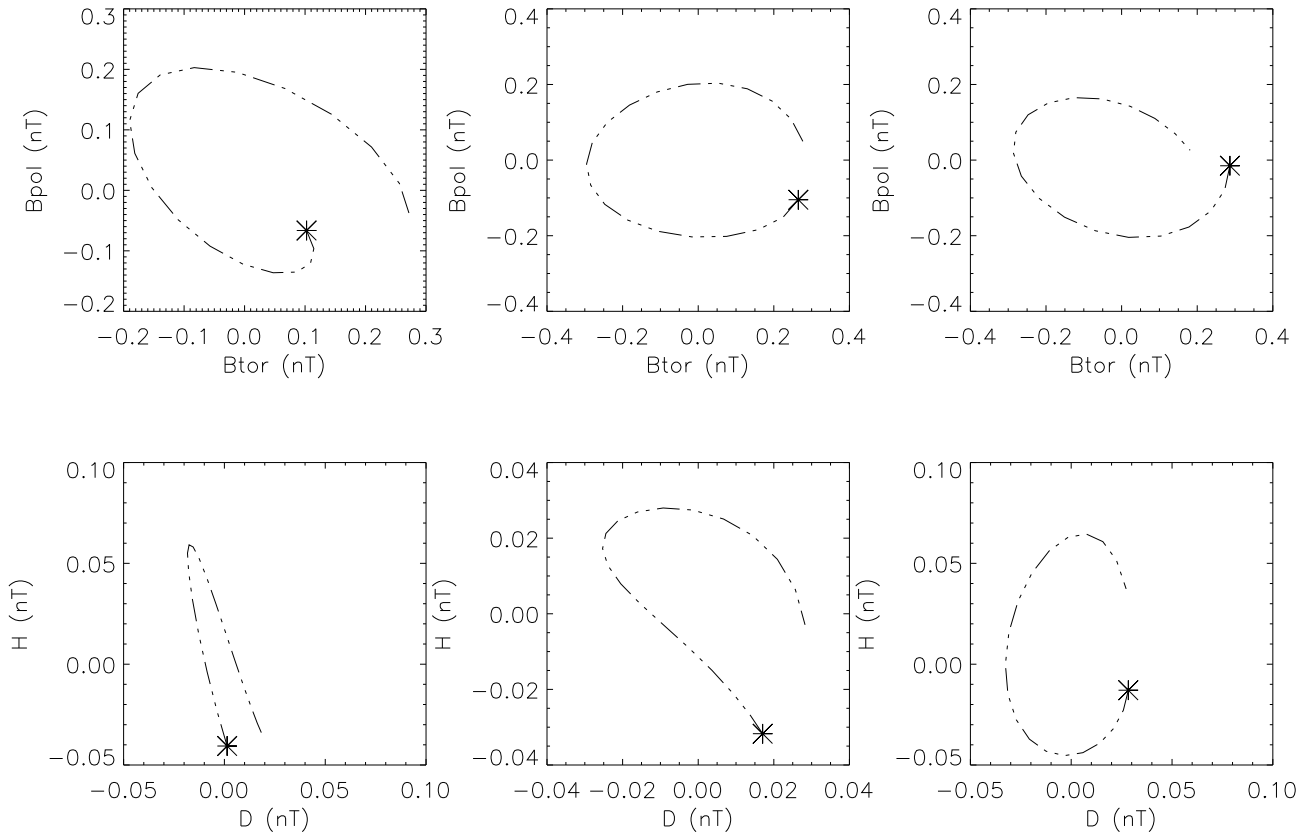

(a)

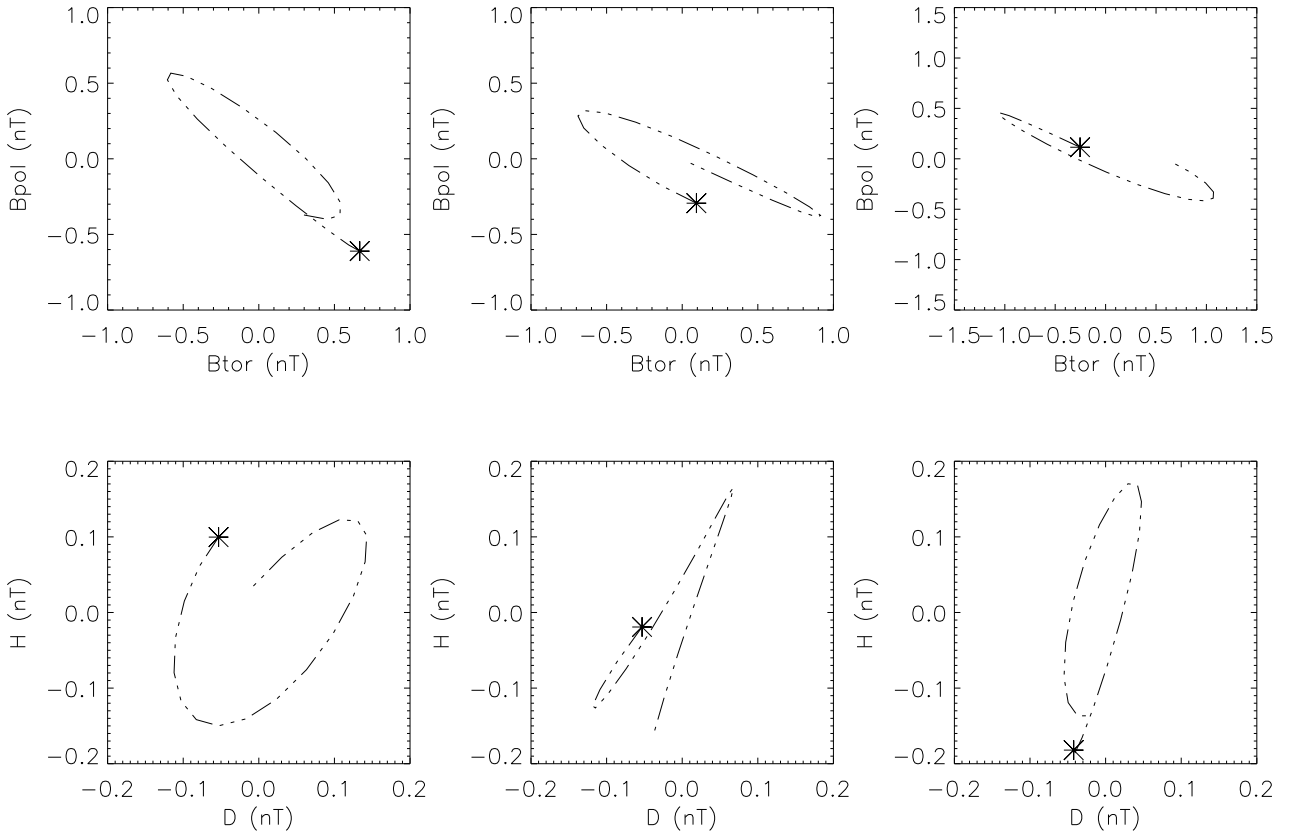

(b)

Figure 7.6: *Examples of the polarisation ellipse where the* 90^0 *rotation a) cannot be observed and b)cannot be clearly observed.*

hodograms of the satellite and ground data have the same polarisation and consequently no rotation is observable. The *not clear* describes hodograms where the rotation is intermediate together with a mixture of polarisation sense (i.e. the interchange between clock wise and counter clock wise polarisation sense). Examples of polarisation ellipse hodograms that resemble *no rotation* and *not clear* characteristics are presented in Figure 7.6(a) and 7.6(b) respectively. The 90^0 rotation is a direct result of the field-aligned currents associated with a shear Alfvén mode meeting the neutral atmosphere, where the curl of magnetic field is finite/zero (Hughes, 1983). The explanation of *no rotation* and *not clear* polarisation involves the reflection and conversion coefficients that determine the mixing of the shear Alfvén and fast mode MHD waves in the ionosphere. The modelling studies of Sciffer et al. (2005) informs that in cases where there is only propagating compressional mode and no incident shear Alfvén mode there is no 90^0 rotation observable.

At lower latitudes such as those considered in this study the rotation effects depends highly on the conversion coefficients of the MHD wave mode and consequently the ionosphere conductivities. In performing our statistical study we did not determine the reflection and conversion coefficients as this was beyond the scope of this work. Therefore, the *not clear* ellipses are not completely ruled out not to be a rotation but rather a variety of polarisation that depends on the altitude, conversion of shear Alfvén wave to compressional wave between the ionosphere and ground as shown by Sciffer et al. (2004, 2005) for particular wave lengths. By inspecting the two tables it is clear that the Doppler frequency shift is frequently observed but it is not the case for pure 90^0 rotation of the resonant magnetic field components. Therefore, at this stage one can speculate and associate the *not clear* polarisation ellipse to the variety of azimuth polarisation as per studies cited above.

It is worthwhile noticing that the events considered are 10 minute activities because we were interested in those events observed (simultaneously by the satellite and on the ground) when CHAMP was passing over the HER and SUT ground stations. It is possible that some of these events were observed when the FLR was switching off or at the commencement stage before the resonance activity could peak. It is understood that at both of these stages the resonance activity has not significantly risen to the maximum. The technique used to facilitate FLR detection is very sensitive and it is desirable to have an indicator of the FLR strength. Hence, we also attribute the outcome of the experiment to the strength of the resonance observed.

Date	Time	BIMF	VSW	cone angle	frequency (mHz) at L=1.8		polarisation
	UT	nT	(km/s)	(deg)	HER	CHAMP	
2003 01 03	15h37-15h47	13	550	30	40	35	90^0 *rotation*
2003 01 15	13h34-13h44	7	400	55	35	30	not clear
2003 01 19	13h23-13h33	11	550	30	45	40	not clear
2003 01 20	14h06-14h17	8	600	50	35	40	90^0 *rotation*
2003 02 05	11h46-11h56	7	550	35	45	40	not clear
2003 02 06	12h29-12h39	5	500	55	55	50	90^0 *rotation*
2003 02 17	11h07-11h17	7	600	25	45	40	90^0 *rotation*
2003 02 19	11h00-11h10	6	530	25	55	45	not clear
2003 02 20	10h10-10h20	7	650	25	50	50	not clear
2003 02 21	10h53-11h03	7	600	40	45	45	not clear
2003 02 23	10h46-10h56	5	600	55	50	45	not clear
2003 02 26	09h49-09h59	8	500	25	55	45	not clear
2003 02 28	09h42-09h52	7	450	40	55	45	90^0 *rotation*
2003 03 02	09h35-09h47	6	400	50	45	40	not clear
2003 03 06	09h20-09h30	6	500	45	50	40	not clear
2003 03 14	08h49-09h00	14	600	45	40	40	not clear
2003 03 15	07h59-08h09	7	600	50	50	40	not clear
2003 03 16	08h41-08h51	7	700	50	58	45	90^0 *rotation*
2003 03 17	07h51-08h01	6	700	25	55	40	not clear
2003 03 18	08h33-08h43	6	750	30	55	40	not clear
2003 03 19	07h43-07h53	4	750	55	55	40	not clear
2003 03 21	07h35-07h45	6	600	50	55	40	not clear
2003 03 22	08h17-08h27	6	600	30	60	50	not clear
2003 03 24	08h09-08h19	5	600	27	50	45	no rotation
2003 03 27	07h10-07h17	9	450	50	58	50	not clear
2003 03 28	07h52-08h02	6	500	60	50	40	not clear
2003 03 29	07h02-07h12	5	450	15	50	45	not clear
2003 04 04	06h36-06h46	7	500	26	55	45	90^0 *rotation*
2003 04 05	07h18-07h28	7	500	45	55	50	not clear
2003 04 14	05h34-05h44	6	650	60	55	45	not clear
2003 04 16	05h43-05h53	7	700	53	55	40	not clear
2003 04 18	05h52-06h02	7	500	55	55	50	not clear
2003 04 22	05h16-05h26	7	600	50	55	50	not clear
2003 06 01	13h13-13h23	8	550	30	53	55	90^0 *rotation*
2003 06 07	12h40-12h50	10	650	50	55	60	90^0 *rotation*
2003 06 09	12h30-12h40	6	650	40	60	65	not clear
2003 06 25	11h00-11h10	7	550	53	50	60	90^0 *rotation*
2003 06 27	10h49-10h59	8	700	50	50	55	not clear

Table 7.2: *Same as Table 7.1 but for the year 2003.*

Date	Time	BIMF	VSW	cone angle	frequency (mHz) at L=1.8		polarisation
	UT	nT	(km/s)	(deg)	HER	CHAMP	
2003 07 05	10h03-10h13	5	700	55	50	55	not clear
2003 07 16	09h44-09h54	12	650	60	50	50	not clear
2003 07 17	08h52-09h02	6	550	35	60	50	not clear
2003 07 27	07h51-08h01	6	700	25	55	60	not clear
2003 07 29	07h38-07h59	8.5	750	15	55	55	not clear
2003 07 30	08h18-08h29	6.3	750	40	60	70	not clear
2003 08 01	08h06-08h16	6	800	45	60	65	not clear
2003 08 03	07h53-08h04	4	650	30	55	50	not clear
2003 08 08	06h36-06h46	9	750	55	55	60	not clear
2003 08 09	07h16-07h26	7	650	55	65	75	not clear
2003 08 11	07h03-07h13	7	500	55	65	50	not clear
2003 08 12	06h11-06h21	9	650	60	60	60	90^0 *rotation*
2003 08 16	05h45-05h55	5	600	45	55	60	not clear
2003 08 21	05h59-06h09	13	600	57	70	60	90^0 *rotation*
2003 08 22	05h06-05h17	8.5	750	35	75	80	not clear
2003 08 23	05h46-05h56	7	750	60	65	65	clear
2003 09 17	15h36-15h46	8	800	35	50	40	not clear
2003 09 19	15h22-15h32	6	750	40	60	55	90^0 *rotation*
2003 10 06	14h08-14h18	10	500	25	55	50	not clear
2003 10 21	13h04-13h14	8	700	75	50	40	not clear
2003 11 04	11h15-11h25	12	750	75	50	45	not clear
2003 11 11	11h04-11h14	11	700	55	55	50	not clear
2003 11 12	10h10-10h20	6	700	25	55	50	not clear
2003 11 13	10h48-10h58	9	700	55	55	40	not clear
2003 11 14	09h53-10h03	8	650	60	55	40	not clear
2003 11 15	10h31-10h41	9	650	25	50	45	90^0 *rotation*
2003 11 17	10h15-10h25	7	700	20	60	55	not clear
2003 11 18	09h20-09h30	5	700	40	50	40	not clear
2003 11 19	09h58-10h08	5	600	40	50	43	not clear
2003 11 24	10h02-10h12	10	550	45	55	45	not clear
2003 11 25	09h07-09h17	6	600	45	50	45	not clear
2003 11 27	08h50-09h00	5	450	15	50	50	not clear
2003 12 06	08h18-08h28	8	550	35	47.5	38	not clear
2003 12 08	08h00-08h10	11	450	35	55	50	not clear
2003 12 09	08h37-08h47	11	650	45	55	45	not clear
2003 12 10	07h42-07h53	8	700	40	75	60	90^0 *rotation*
2003 12 11	08h20-08h30	7	800	45	60	50	90^0 *rotation*
2003 12 12	07h25-07h35	6	730	45	75	50	not clear
2003 12 13	08h02-08h12	6	750	50	55	40	not clear
2003 12 14	07h07-07h17	6	800	60	55	50	not clear
2003 12 21	06h50-07h00	11	550	40	55	45	not clear

Table 7.2 continued.

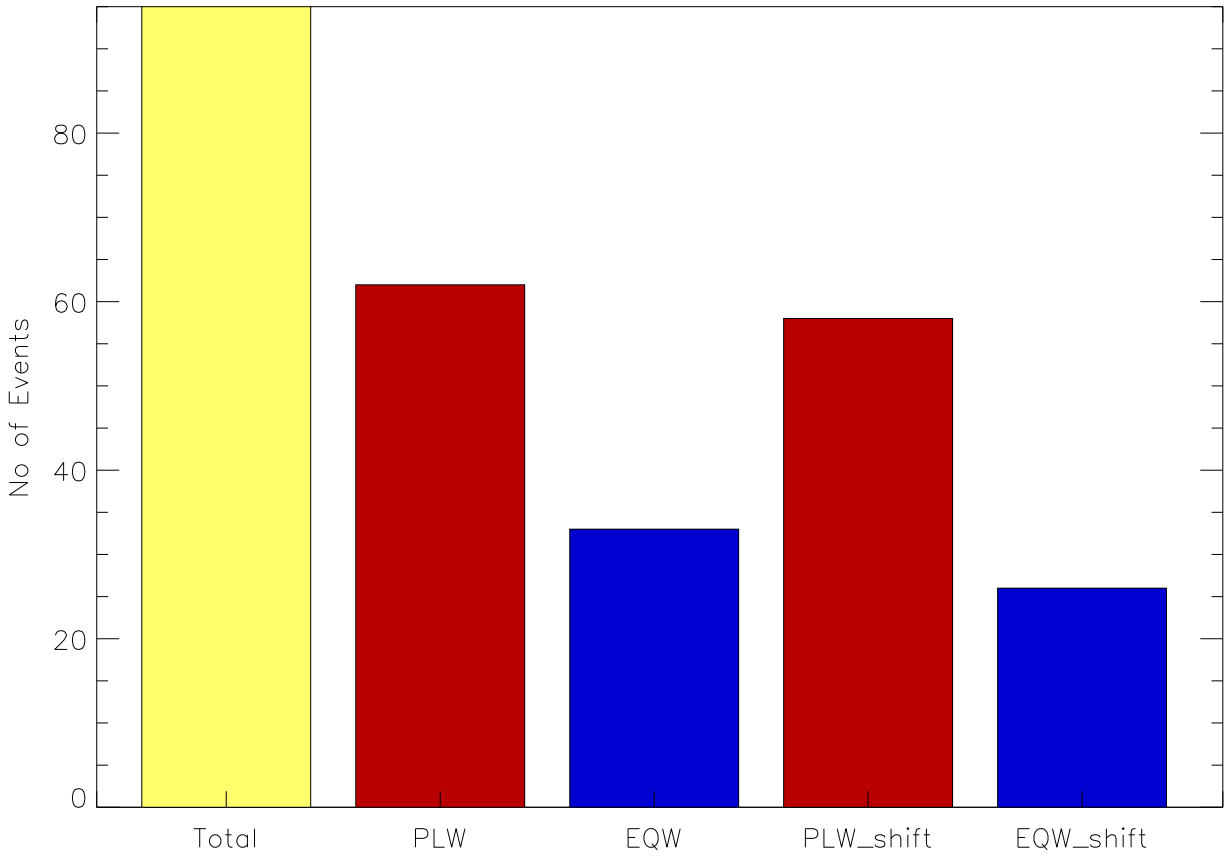

Figure 7.7: *Summary of statistics of Tables 7.1 and 7.2. Shown by the bars are the total number of events in the two tables, pole and equator wards events abbreviated PLW and EQW respectively, and the events with the expected Doppler shift was observed.*

7.6 Summary

This chapter reported a statistical study of FLR's Pc3 events observed by CHAMP when the satellite was in conjunction with HER and SUT southern Africa ground stations. We focused on events observed when the upstream wave activity in the ion foreshock region was intensified. The OMNI high resolution data was used to verify if the solar wind conditions were suitable for the generation of the upstream wave. We used the Doppler shift associated with the rapid motion of the satellite and the rotation of the transverse resonant components caused by ionospheric currents to quantify FLR structure. It was observed that only the Doppler shift condition was mainly satisfied and this was not the case for the pure ionospheric rotation. We suggest that another threshold should be considered to quantify the FLR structure observed resolved from the magnetometer data. The third threshold should estimate the strength of field line resonance. The formulation of an indicator of the strength of FLR is an integral part of future work.

Chapter 8

Summary and conclusion

In this work the structure of continuous pulsations observed at low latitudes was studied by comparing ground and satellite observations of the Earth's magnetic field. In particular, the study focused on the Pc3's field line resonances oscillations excited by the ULF upstream waves generated in the region upstream of the bow shock. These are frequently observed during local day time at latitudes considered for this work. The magnetosphere is a dynamic entity and the magnetic activities occurring such as field aligned currents and other associated currents can disturb estimation of Pc3 pulsation activity. We established a preferable laboratory for our low-latitude Pc3 observation.

We used both linear and non-linear techniques for computing spectral estimates to visualise FLR frequency structure in the vector magnetometer data. These techniques are FFT and MESA respectively. We assessed the performances of these methods by applying both methods to compute spectral estimates for a modelled Pc3 signal. The exercise of experimenting with the generated pulsation signal avoids a biased conclusion, since the input to sinusoids function used to generate the signal and the expected spectra outcome are not unknown. Our assessment demonstrates the superior resolving power of MESA method over FFT technique irrespective of the signal length.

In this study the ULF waves detected in the topside ionosphere by the CHAMP satellite was directly compared to the ground magnetic field measurements in order to study the structure of Pc3 waves at low latitudes. We identified a number of 10-minute Pc3 events observed at times when CHAMP was passing over Southern Africa ground stations. In a 10-minute period CHAMP traverses the latitudinal structure of the geomagnetic pulsation field rapidly due to its low altitude orbit and as a result, the spectral content is likely to change. In order to take into account this effect, we used dynamic MESA spectra computed for 90-second data lengths progressively shifted by 10 seconds in a manner similar to that used by Vellante et al. (2004).

However, our analysis differed from that of Vellante et al. (2004) in two important respects as discussed in chapter 5.

Our observations confirm the compressional wave as the driver of the field line resonance. We observed that low-latitude FLR either oscillate with L-dependent frequencies or discrete frequencies depending on the frequency structure of the source wave spectral content. The spectral content of observations given in chapter 5 are characterised by a number of discrete frequency oscillations for the fast mode wave, one of which drives a field line resonance at a characteristic latitude as detected by both ground and satellite measurements. However, the toroidal mode frequency observed on CHAMP experienced a Doppler shift due to the rapid motion of the satellite across the resonance region. These kinds of observations of discrete FLR oscillations observed at characteristic latitude have been published by Ndiitwani and Sutcliffe (2009)

Chapter 6 reports the results of spectrum analysis of low latitudinal Pc3 geomagnetic pulsations characterised by the toroidal oscillation frequency continuously increasing with decreasing latitude from L =3 to L $\sim$ 1.6 and then decreasing as a result of the larger plasma density of the upper ionosphere. To the best of our knowledge these are first-time observations of toroidal oscillation with a clear L-dependent frequency for lower L-shell values (L $<$ 3) observed by a LEO satellite. The L-dependent frequency oscillations were observed in the presence of a broadband compressional wave spectrum. The events discussed in chapter 6 arise from a broadband source, while the results in chapter 5 and other observations such as those of Vellante et al. (2004) come from a narrow band source. This confirms that Pc3 pulsations do not always have sources with the same frequency structure. Therefore, our observations suggest that we can expect a low-latitude L-dependent spectrum structure to be generated by resonant coupling between a broadband compressional wave field and a toroidal field line oscillation with a specific distribution of plasma density at the upper ionosphere. The study of L-dependent Pc3 pulsations have been published by Ndiitwani and Sutcliffe (2010).

Our investigation of spectral structures observed both in chapter 5 and 6 confirmed that a typical Pc3 pulsation consists of a field line resonance (FLR) component, with latitude dependent frequency and an upstream wave (UW) component, with frequency proportional to the IMF intensity. During this study we noticed that, both CHAMP and ground power spectra also exhibit frequency components which are independent of latitude and IMF intensity. However, these were not studied further but suggest that there is a third mechanism playing a role in the generation of a typical Pc3 pulsation. We believe that the cavity or wave guide mode resonance is the most likely explanation of additional frequency components, similar to those previously

reported by Menk et al (2000). The study of Sutcliffe et al. (article in preparation) aims to demonstrate the simultaneous presence of all three components.

Overall, we have shown that the CHAMP mission provides an interesting opportunity to test theoretical predictions of MHD waves. As a result of the success of this approach much has been learned about the structure of Pc3, in particular the field line resonances and the effect of ionospheric currents on the transmission of ULF signals to the ground. The results of this study, together with MHD mathematical models and previously published results will help to understand the physical system responsible for geomagnetic pulsations. A mid latitude HF radar is planned for South Africa, the observation of which should greatly enhance these investigations.

8.1 Future work

The previous chapter reported a statistical study of FLR observations presented in chapter 5 and 6. We established a database of events scanned from two years of data. We set two criteria namely, the Doppler shift and the expected 90^0 rotation of resonant magnetic field components to quantify the FLR structure. It was observed that only one of the two criteria is clearly observed. Hence, we could not safely conclude whether the FLR are frequently observed by CHAMP on crossing HER and SUT stations or not. We suggest that for this kind of study a threshold that would estimate the strength of the resonance should be developed. The development of an estimator of FLR strength is part of future work. The suggested estimator would not only improve this kind of study but will introduce a new dimension to the interpretation of the crossphase spectrum used to identify the FLR frequency.

There are interesting observations that were made in the course of the statistical study that are not shown in this document, which suggest that the CHAMP satellite at higher latitudes observes a second harmonic oscillation. This was still on the basis of comparing ground and satellite magnetic data spectral contents. For a few hours during the local morning of 08 February 2002 the fundamental and second harmonic oscillations were observable in the HER-SUT dynamic crossphase spectrum. At certain latitudes the corresponding azimuthal component spectral frequency structure observed along the satellite trajectory exhibited an harmonic oscillation comparable to the second harmonic frequency observed on the ground. This interpretation requires the necessary theoretical calculation. In the future it is intended to develop a mathematical model capable of estimating the fundamental and harmonic frequencies to confirm this interpretation.

Bibliography

Alfvén, H., 1942, On the existence of electromagnetic-hydrodynamic waves, Nature., 150, 405–406.

Allan, W., White, S. P., and Poulter, E. M., 1985, Magnetospheric coupling of hydromagnetic waves - Initial results, Geophys. Res. Lett., 12, 287–290.

Anderson, B. J., 1994, An overview of spacecraft observations of 10 s to 600 s period magnetic pulsations in Earth's magnetosphere., Geophysical Monogr, AGU, Washington., 81, 25–43.

Anderson, M., 1974, On the calculation of filter coefficients for maximum entropy analysis., Geophysics., 39, 69–72.

Armstrong, J. C. and Zmuda, A. J., 1973, Triaxial magnetic measurements of field-aligned currents at 800 km in the auroral region: Initial results., J. Geophys. Res., 78, 6802–6807.

Baransky, L. N., Belokris, S. P., Borovkov, Y. E., Gokhberg, M. B., Fedorov, E. N., and Green, C. A., 1989, Restoration of the meridional structure of geomagnetic pulsation fields from gradient measurements., Planet. Space Sci., 37, 859–864.

Baransky, L. N., Borovkov, J. E., Gokhberg, M. B., Krylov, S. M., and Troitskaya, V. A., 1985, High resolution method of direct measurement of the magnetic field line's eigenfrequencies., Planet. Space Sci., 33, 1369–1374.

Barnes, A., 1970, A theory of generation of bow-shock-associated hydromagnetic waves in the upstream interplanetary medium., Cosmic Electrodynamics., 1, 90–114.

Baumjohann, W. and Treumann, R. A., 1997, Basic space plasma physics, Imperial College press.

Beard, D. B., 1960, The interaction of the Terrestrial magnetic field with the solar corpuscular radiation, J. Geophys. Res., 65, 3559–3568.

Bellan, P. M., 1996, Mode conversion into non-MHD waves at the Alfvén layer: The case against the field line resonance, J. Geophys. Res., 101(A11), 24887–24898.

Biermann, L., 1951, *Kometenschwiefe und solar Korpuskularstrahlung*, Zeit. Astrophys., 29, 274–286.

Birkeland, K., 1908, The Norwegian Aurora Polaris, 1902-1903, Vol. 1 Sect. 1, Aschehoug, Oslo.

Blackman, R. B. and Tukey, J. W., 1959, The measurement of power spectra from the point of view of communications Engineering., Dover, New York.

Bloomfield, P., 1976, Fourier Analysis of Time Series., John Wiley and Sons.

Bolshakova, O. V., 1966, Stable geomagnetic micropulsation and solar corpuscular streams, Geomag. Aeron., 6, 851–879.

Bolshakova, O. V. and Troitskaya, V. A., 1968, Relation of the IMF direction to the system of stable oscillations, Dokl. Akad. Nauk. USSR., 180, 343–346.

Brigham, E. O., 1974, The Fast Fourier Transform., Prentice-Hall, Inc.

Brigham, E. O., 1988, The Fast Fourier Transform and Its Applications., Expansion of the 1974 book, Prentice-Hall, Englewood Cliffs.

Burg, J. P., 1967, Maximum entropy spectral analysis, paper presented at 37th meeting, Soc. Geophys., Oklahoma City, Okla., Oct. 1967.

Burg, J. P., 1968, A new analysis technique for time series data, paper presented at NATO Advanced Study Institute on Signal processing, Enschede, Netherlands, Aug. 1968.

Burg, J. P., 1972, The relationship between maximum entropy spectra and maximum likehood spectra., Geophysics., 37, 375–376.

Burg, J. P., 1975, Maximum Entropy Spectral Analysis., Ph.D. thesis, Stanford University.

Burgess, D., 1995, Collisionless shocks. In Introduction to space physics (ed. Kivelson M. G. and Russel C. T.) p. 129-163., Cambridge University Press.

Burrus, C. D., 2009, The Cooley-Tukey Fast Fourier Transform Algorithm., http://cnx.org/content/m16334/latest/.

Chapman, S. and Ferraro, V. C., 1931a, A new theory of magnetic storms, Terr. Magn. Atmos. Elect., 36, 77–97.

Chapman, S. and Ferraro, V. C., 1931b, A new theory of magnetic storms, I. The initial Phase, Terr. Magn. Atmos. Elect., 36, 171–186.

Chapman, S. and Ferraro, V. C., 1931c, A new theory of magnetic storms. II. The initial phase, Terr. Magn. Atmos. Elect., 37, 147–156.

Chen, L. and Hasegawa, A., 1974, A theory of long-period magnetic pulsations, I, Steady state excitation of field line resonances., J. Geophys. Res., 79, 1024–1032.

Chen, W. Y. and Stegen, G. R., 1974, Experiment with maximum entropy power spectra of sinusoid., J. Geophys. Res., 79, 3019–3022.

Chi, P. J. and Russell, C. T., 1998, An interpretation of the cross-phase spectrum of geomagnetic pulsations by the field line resonance theory., Geophys. Res. Lett., 25, 4445–4448.

Cooley, J. W. and Tukey, J. W., 1965, An algorithm for the machine calculation of complex Fourier series., Math. Comput., 19, 297–301.

Cravens, T. E., 1997, Physics of solar system plasma, Cambridge University Press.

Cummings, W. D., O'Sullivan, R. J., and Coleman Jr, P. J., 1969, Standing Alfvén waves in the magnetosphere, J. Geophys. Res., 74, 778–793.

Dent, Z. C., Mann, I. R., Goldstein, J., Menk, F. W., and Ozeke, L. G., 2006, Plasmaspheric depletion, refilling, and plasmapause dynamics: A coordinated ground-based and IMAGE satellite study., J. Geophys. Res. A03205, doi:10.1029/2005JA011046.,, 111.

Denton, R. E. and Gallagher, D. L., 2000, Determining the mass density along magnetic field lines from toroidal eigenfrequencies, J. Geophys. Res., 105, 27717–27725.

Dungey, J. M., 1954, Electrodynamics of the outer atmosphere, Penn. State Ionosph. Res. Lab. Report 69.

Dungey, J. W., 1961, Interplanetary magnetic field and the auroral zones, Phys. Rev. Lett., 6, 47–48.

Dungey, J. W., 1963, The structure of the exosphere or adventures in velocity space. In Geophysics, The Earth's Environment (ed. C. Dewitt, J. Hieblot and A. Lebeau) p. 503-550., Gordon & Breach, New York.

Dungey, J. W., 1964, Evidence of hydromagnetic waves in the Earth's magnetosphere and of their propagation to the Earth's surface, Phys. Rev. Lett., 12, 213–215.

Dungey, J. W., 1965, Effects of electromagnetic perturbations on particles trapped in the radiation belts, Space Sci. Rev., 4, 199–222.

Engebretson, M. J., Cahill Jr, L. J., Arnoldy, R. L., Anderson, B. J., Rosenberg, T. J., Carpenter, D. L., Inan, U. S., and Eather, R. H., 1991, The role of the ionosphere in coupling upstream ULF wave power into the dayside magnetosphere, J. Geophys. Res., 96, 1527–1542.

Engebretson, M. J., Meng, C. I., Arnoldy, R. L., and Cahill, L. J., 1986, Pc3 pulsations observed near the south polar cusp., J. Geophys. Res., 91, 8909–8918.

Engebretson, M. J., Zanetti, L. J., Potemra, T. A., Baumjohann, W., Lühr, H., and Acuna, H., 1987, Simultaneous observation of Pc3-4 pulsations in the solar wind and in the Earth's magnetosphere., J. Geophys. Res., 92, 10053–10062.

Erickson, K. N., Swanson, R. L., Walker, R. J., and Winckler, J. R., 1979, A study of magnetosphere dynamics during auroral electrojet events by observations of energetic electron intensity changes at synchronous orbit., J. Geophys. Res., 84, 931–942.

Erickson, K. N. and Winckler, J. R., 1973, Auroral electrojets and evening sector electron dropouts at synchronous orbit., J. Geophys. Res., 78, 8373–8380.

Fairfield, D. H., 1969, Bow shock associated waves observed in the far upstream interplanetary medium., J. Geophys. Res., 74, 3541–3553.

Ferreira, S. E. S., 2002, The heliospheric transport of galactic cosmic rays and jovian electrons., Ph.D. thesis, Potchefstroom University for CHE, South Africa.

Fougere, P. F., 1977, A solution to the problem of spontaneous line splitting in maximum entropy power spectrum analysis., J. Geophys. Res., 82, 1051–1054.

Fougere, P. F., Zawalick, E. J., and Radoski, H. R., 1976, Spontaneous line splitting in maximum entropy power spectrum analysis., Phys. Earth Planet. Inter., 12, 201–207.

Fraser, B. J., McPherron, R. L., and Russell, C. T., 1988, Radial Alfvén velocity profiles in the magnetosphere and their relation to ULF wave field-line resonances., Adv. Space Res., 8, 849–852.

Gary, S. P., Gosling, J. T., and Forslund, D. W., 1981, Electromagnetic ion-beam instabilities upstream of the Earth's bow shock., J. Geophys. Res., 86, 6691–6696.

Gilbert, W., 1600, De Magnete magneticisque corporibus et de magno magnete Tellure. London [reprinted in Latin: Stettin (1628) and Frankfurt (1629);English transl by P.F. Mottelay: Wiley, New York (1893); reprinted in English: Dover New York (1958)].

Glassmeier, K.-H., 1984, On the influence of ionospheres with non-uniform conductivity distribution on hydromagnetic waves., J. Geophys., 54, 125–137.

Glassmeier, K.-H., 1988, Reconstruction of the ionospheric influence on ground-based observations of a short-duration ULF pulsation event., Planet. Space Sci., 36, 801–817.

Gold, T., 1959, Motions in the magnetosphere of the Earth., J. Geophys. Res., 64, 1219–1224.

Green, A. W., Worthington, E. W., Baransky, L. N., Fedorov, N. A., Kurneva, V. A., Pilipenko, D. N., Shvetzov, D. N., Bektemirov, A. A., and Philipov, G. V., 1993, Alfvén field line resonances at low latitudes (L = 1.5)., J. Geophys. Res., 98, 15693–15699.

Green, C. A., Odera, T. J., and Stuart, W. F., 1983, The relationship between the strength of the IMF and the frequency of magnetic pulsations on the ground and in the solar wind., Planet. Space Sci., 31, 559–567.

Greenstadt, E. W., Green, I. M., Inouye, G. T., Hundhausen, A. J., Bame, S., and Strong, I. B., 1968, Correlated magnetic field and plasma observations of the Earth's bow shock., J. Geophys. Res., 73, 51–60.

Greenstadt, E. W. and Olson, J. V., 1977, A contribution to ULF activity in the Pc3-4 range correlated with IMF radial orientation., J. Geophys. Res., 82, 4991–4996.

Gringauz, K. I., Troitskaya, V. A., Solomatina, E. K., and Shchepetnov, R. V., 1970, The relationship of solar wind variables to periods of continuous micropulsations of electromagnetic field of the Earth., Dokl. Akad. Nauk. USSR., 5, 1061–1069.

Hasegawa, A., Tsui, K. H., and Assis, A. S., 1983, A theory of long period magnetic pulsations, 3. Local field line oscillations., Geophys. Res. Lett., 10, 765–767.

Hattingh, S. K. F. and Sutcliffe, P. R., 1987, Pc3 pulsation eigenperiod determination at low latitudes., J. Geophys. Res., 92, 12433–12436.

Haykin, S. and Kesler, S., 1979, Prediction-error filtering and maximum-entropy spectral estimation, In: S. Haykin (Editor), Nonlinear Methods of Spectral analysis, Vol 34, p. 9-72., Springer-Verlag Berlin Heidelburg.

Heilig, B., Lühr, H., and Rother, M., 2007, Comprehensive study of ULF upstream waves observed in the topside ionosphere by CHAMP and on the ground., Ann. Geophys., 25, 737–754.

Hughes, W. J., 1983, Hydromagnetic waves in the magnetosphere. In Solar-terrestrial physics (ed. Caravillano, R. L. and Forbes, J. M.) p. 453-477., Reidel D. Pub. Co. Dordrecht.

Hughes, W. J., 1994, Magnetospheric ULF waves: A tutorial with a historical perspective, in: Solar wind sources of magnetospheric Ultra-Low-Frequency waves, Geophysical Monogr, AGU, Washington, D.C., 81, 1–11.

Hughes, W. J. and Southwood, D. J., 1976, An illustration of modification of geomagnetic pulsation structure by the ionosphere., J. Geophys. Res., 81, 3241–3247.

Hundhausen, A. J., 1995, The solar wind. In Introduction to space physics (ed. Kivelson M. G. and Russel C. T.) p. 91-128, Cambridge University Press.

Iijima, T. and Potemra, T. A., 1976a, The amplitude distribution of field-aligned currents at northern high latitudes observed by TRIAD., J. Geophys. Res., 81, 2165–2174.

Iijima, T. and Potemra, T. A., 1976b, Field-aligned currents in the dayside cusp observed by Triad., J. Geophys. Res., 81, 5971–5979.

Jacobs, J. A., 1970, Geomagnetic Micropulsation., Springer-Verlag, New York.

Jacobs, J. A., Kato, Y., Matsushita, S., and Troitskaya, V. A., 1964, Classification of geomagnetic micropulsations., J. Geophys. Res., 69(1), 180–181.

Jenkins, G. M. and Watts, D. G., 1969, Spectral Analysis and its application., Holden-day, San Francisco.

Jones, R. H., 1965, A reappraisal of the periodogram in spectral analysis., Technometrics., 7, 531–542.

Junginger, H. and Baumjohann, W., 1988, Dayside long-period magnetospheric pulsations: solar wind dependence., J. Geophys. Res., 93, 877–883.

Kane, R. P. and Trivedi, N. B., 1982, Comparison of Maximum Entropy Spectral Analysis (MESA) and Least-Squares Linear Prediction (LSLP) methods for some artificial samples., Geophysics., 47, 1731–1736.

Kim, K.-H. and Takahashi, K., 1999, Statistical analysis of compressional Pc3-4 pulsations observed by AMPTE CCE at L = 2-3 in the dayside magnetosphere., J. Geophys. Res., 104, 4539–4558.

Kivelson, M. G., 1995, Pulsations and Magnetohydrodynamic waves. In Introduction to space physics (ed. Kivelson M. G. and Russel C. T.) p. 330-355., Cambridge University Press.

Kivelson, M. G. and Southwood, D. J., 1985, Resonant ULF waves: A new interpretation., Geophys. Res. Lett., 12, 49–52.

Kivelson, M. G. and Southwood, D. J., 1986, Coupling of global megnetospheric MHD eigenmodes to field line resonances, J. Geophys. Res., 91, 4345–4351.

Kivelson, M. G. and Southwood, D. J., 1988, Hydromagnetic waves and the ionosphere., Geophys. Res. Lett., 15, 1271–1274.

Lacoss, R. T., 1971, Data adaptive spectral analysis methods., Geophysics., 36, 661–675.

Le, G. and Russell, C., 1994, The Morphology of ULF Waves in the Earth's Foreshock, in: Solar wind sources of magnetospheric Ultra-Low-Frequency waves., Geophysical Monogr, AGU, Washington, D.C., 81, 87–98.

Le, G. and Russell, C., 1996, Solar wind control of upstream wave frequency., J. Geophys. Res., 101, 2571–2575.

Lee, D., 1996, Dynamics of MHD wave propagation in the low-latitude magnetosphere., J.Geophys. Res., 101, 15371–15386.

Levinson, H., 1947, The Wiener rms (root mean square) error criterion in filter design and prediction., J. Math. Phys., 25, 261–278.

Maeda, N., Takasaki, S., Kawano, H., Ohtani, S., Décréau, P. M. E., Trotignon, J. G., Solovyev, S. I., Baishev, D. G., and Yumoto, K., 2009, Simultaneous observations of the plasma density on the same field line by the CPMN ground magnetometers and the Cluster satellites., Adv. Space. Res., 43, 265–272.

Maus, S., Lühr, H., Balasis, G., Rother, M., and Mandea, M., 2005, Introducing POMME, The Potsdam Magnetic Model of the Earth, In Earth Observation with CHAMP, (ed C., Reigber, H., Lühr, P., Schwintzer, and J., Wickert,) p. 293-298., Springer, Berlin-Heidelberg.

McComas, D. J., Phillips, J. L., Bame, S. J., Gosling, J. T., Glodstein, B. E., and Neugebauer, M., 1995, Ulysses solar wind observation to 56^0 south, Space. Sci. Rev., 72, 93–98.

McPherron, R. L., 1995, Magnetospheric dynamic, In Introduction to space physics (ed M.G. Kivelson and C.T. Russel) p. 400-458., Cambridge university press.

McPherron, R. L., 2005, Magnetic pulsations: Their sources and relation to solar wind and geomagnetic activity., Surveys in Geophysics., 26, 545–592.

Mead, G. D., 1967, Neutral points on the boundary of the closed magnetosphere., Space Sci. Rev., 7, 158–165.

Mead, G. D. and Beard, D. B., 1964, Shape of the Geomagnetic field solar wind boundary., J. Geophys. Res., 69, 1169–1179.

Menk, F. W., Mann, I. R., Smith, A. J., Waters, C. L., Clilverd, M. A., and Milling, D. K., 2004, Monitoring the plasmapause using geomagnetic field line resonances., J. Geophys. Res. A04216, doi:10.1029/2003JA010097.,, 109.

Menk, F. W., Orr, D., Clilverd, M. A., Smith, A. J., Waters, C. L., Milling, D. K., and Fraser, B. J., 1999, Monitoring spatial and temporal variations in the dayside plasmasphere using geomagnetic field line resonances, J. Geophys. Res., 104, 19955–19969.

Menk, F. W., Waters, C. L., and Fraser, B. J., 2000, Field line resonances and waveguide modes at low latitudes: 1. Observations., J. Geophys. Res., 105, 7747–7761.

Midgley, J. E. and Davis, L. J., 1963, Calculation by a moment technique of the perturbation of the geomagnetic field by the solar wind., J. Geophys. Res., 68, 5111–5123.

Nagata, T., Kokubun, S., and Iijima, T., 1963, Geomagnetically conjugate relationships of giant pulsations at Syowa Base, Antarctica, and Reykjavik, Iceland., J. Geophys. Res., 68, 4621–4625.

Ndiitwani, D. C. and Sutcliffe, P. R., 2009, The structure of low-latitude Pc3 pulsations observed by CHAMP and on the ground., Ann. Geophys., 27, 1267–1277.

Ndiitwani, D. C. and Sutcliffe, P. R., 2010, A study of L-dependent Pc3 pulsations observed by low Earth orbitting CHAMP satellite., Ann. Geophys., 28, 407–414.

Nishida, A., 1978, Geomagnetic diagnosis of the magnetosphere., Springer-Verlag, New York.

Odera, T. J., Van Swol, D., Russell, C. T., and Green, C. A., 1991, Pc3,4 magnetic pulsations observed simultaneously in the magnetosphere and at a multiple ground stations., Geophys. Res. Lett., 18, 1671–1674.

Oppenheim, A. V. and Schafer, R. W., 1975, Digital signal processing., Prentice-Hall, Englewood Cliffs, N.J.

Orr, D., 1973, Magnetic pulsations within the magnetosphere., J. Atmos. Terr. Phys., 35, 1–50.

Parker, E. N., 1958, Cosmic ray modulation by the solar wind, Physical Reviews., 110, 1445–1449.

Parker, E. N., 1963, Interplanetary dynamical processes, Interscience, New York.

Paschmann, G., 1991, The Earth's magnetopause. In Geomagnetism Volume 4 (ed. Jacobs J. A.) p. 295-331., Academic press limited.

Phillips, J. L., Bame, S. J., Barnes, A., Barraclough, B. L., Feldman, W. C., Goldstein, B. E., Gosling, J. T., Hoogeven, G. W., McComas, D. J., Neagebauer, M., and Suess, S. T., 1995, Ulysses solar wind plasma observation from pole to pole, Geophys. Res. Lett., 22, 3301–3304.

Pilipenko, V. A., Fedorov, E., and Engebretson, M. J., 2008, Structure of ULF Pc3 waves at low altitudes, J. Geophys. Res. A11 208, doi:10.1029/2008JA013243.,, 113.

Poulter, E. M., Allan, W., and Bailey, G. J., 1988, ULF pulsation eigenperiods within the plasmasphere., Planet. Space. Sci., 36, 185–196.

Reigber, C., Lühr, H., and Schwintzer, P., 1999, The CHAMP geopotential mission, Bollettion di Geofisicica Teorica ed Applicata., 40, 285–289.

Reigber, C., Lühr, H., and Schwintzer, P., 2002, CHAMP Mission status., Adv.Space Res., 30, 129–134.

Ruohoniemi, J. M., Greenwald, R. A., Baker, K. B., and Samson, J. C., 1991, HF radar observation of Pc5 field line resonances in the midnight/early morning MLT sector, J. Geophys. Res., 96, 15697–15710.

Russell, C., Luhmann, J. G., Odera, T. J., and Stuart, W. F., 1983, The rate of occurrence of day side Pc3, 4 pulsations; the L-value dependence of the IMF cone angle effect., Geophys. Res. Lett., 10, 663–666.

Russell, C. T., 1979, The interaction of the solar wind with Mars, Venus and Mercury. In solar system plasma physics, Vol II (ed. C. F. Kennel, L. J. Lanzerotti and E. N. Parker) p. 207-252., North-Holland, Amsterdam.

Russell, C. T., 1985, Planetary bow shocks. In Collisionless Shocks in the Heliosphere: Reviews of current Research (ed. B. T. Tsurutani and R. G. Stone) p. 109-130, AGU. Washington, D.C.

Russell, C. T., 1987, Planetary magnetism. In Geomagnetism, Vol. 2 (ed. J. A. Jacobs) p. 457-523., Academic Press, London.

Russell, C. T. and Hoppe, M. M., 1981, The dependence of upstream wave periods on the interplanetary magnetic field strength., Geophys. Res. Lett., 8, 615–618.

Saito, T., 1964, A new index of geomagnetic pulsation and its relation to solar M-regions., Report., Ionsph. Space Res., Japan., 18, 260–274.

Saito, T., 1969, Geomagnetic pulsation., Space Sci. Rev., 10, 319–412.

Samson, J. C., Harrold, B. G., Ruohoniemi, J. M., Greenwald, R. A., and Walker, A. D. M., 1992, Field line resonances associated with MHD waveguides in the magnetosphere, J. Geophys. Res., 19, 441–444.

Samson, J. C., Jacobs, J. A., and Rostoker, G., 1971, Latitude-dependent characteristics of long period geomagnetic pulsation,., J. Geophys. Res., 76, 3675–3683.

Sciffer, M. D., Waters, C. L., and Menk, F. W., 2004, Propagation of ULF waves through the ionosphere: Inductive effect for oblique magnetic fields., Ann. Geophys., 22, 1155–1169.

Sciffer, M. D., Waters, C. L., and Menk, F. W., 2005, A numerical model to investigate the polarisation azimuth of ULF waves through an ionosphere with oblique magnetic fields., Ann. Geophys., 23, 3457–3471.

Slutz, R. J. and Winkelman, J. R., 1964, Shape of magnetosphere boundary under solar wind pressure., J. Geophys. Res., 69, 4933–4948.

Southwood, D. J., 1974, Some features of field line resonances in the magnetosphere., Planet. Space Sci., 22, 483–491.

Southwood, D. J., 1985, An introduction to magnetospheric MHD, In Solar system magnetic fields, (ed E. R. Priest) p. 25-35, Kluwer.

Southwood, D. J. and Hughes, W. J., 1983, Theory of Hydromagnetic waves in the magnetosphere., Space Sci. Rev., 35, 301–366.

Southwood, D. J. and Kivelson, M. G., 1981, Charged particle behavior in low frequency Geomagnetic pulsations 1. Transverse waves., J. Geophys. Res., 86, 5643–5655.

Spreiter, J. R. and Briggs, B. R., 1962, Theoretical determination of the form of the boundary of the solar corpuscular stream produced by interaction with the magnetic dipole field of the Earth., J. Geophys. Res., 67, 37–51.

Spreiter, J. R. and Stahara, S. S., 1985, Magnetohydrodynamic and gasdynamic theories for planetary bow waves. In Collisionless plasmas in the Heliosphere: Reviews of current Research (ed. B. T. Tsurutani and R. G. Stone) p. 85-107., AGU, Washington. D. C.

Stephenson, J. A. E. and Walker, A. D. M., 2010, Coherence between radar observations of magnetospheric field line resonances and discrete oscillations in the solar wind., Ann. Geophys., 28, 47–59.

Stewart, B., 1861, On the great magnetic disturbance which extends from August 28th to September 7th, 1859, as recorded by photography at the Kew Observatory, Phil. Trans. R. Soc., 151, 423–430.

Sugiura, M. and Wilson, C. R., 1964, Oscillation of the geomagnetic field lines and associated magnetic perturbations at conjugate points., J. Geophys. Res., 69, 1211–1216.

Sutcliffe, P. R. and Lühr, H., 2003, A comparison of Pi2 pulsations observed by CHAMP in low Earth orbit and on the ground at low latitudes., Geophys. Res. Lett. 2105, doi:10.1029/2003GL018270.,, 30.

Swingler, D. N., 1979, A comparison between Burg's maximum entropy method and a non-recursive technique for the spectral analysis of deterministic signals., J.Geophys. Res., 84, 676–685.

Takahashi, K., Anderson, B. J., and Strangeway, R. J., 1990, AMPTE CCE Observations of Pc3-4 pulsations at L = 2-6., J. Geophys. Res., 95, 17179–17186.

Takahashi, K., Anderson, B. J., and Yumoto, K., 1999, Upper atmosphere research satellite observation of Pi2 pulsation, J. Geophys. Res., 104, 25035–25045.

Thomsen, M. F., 1985, Upstream suprathermal ions, in collisionless shocks in the Heliosphere, Reviews of current Research, (ed by B. T. Tsurutani and R.G. Stone) Geophys. Monogr. Ser., Vol 35, p. 253-270, AGU, Washington, D. C.

Troitskaya, V. A., 1961, Pulsations of the electromagnetic field with periods 1-15 sec. and their connection with Phenomena in the high atmosphere., J. Geophys. Res., 66, 5–19.

Troitskaya, V. A., Alperovitch, L. S., and Djordjio, N. V., 1962, Connection of short period oscillations of electromagnetic field of the Earth and aurora., Izvestia. Akad. Nauk. USSR, Geophys. Series., 2, 178–267.

Troitskaya, V. A. and Gul'elmi, A. V., 1967, Geomagnetic micropulsations and diagnostics of the magnetosphere, Space Sci. Rev., 7, 689–768.

Troitskaya, V. A. and Melnikova, M. V., 1959, On IPDP (10-1 sec) in the electromagnetic field of the Earth and their connection with phenomena in high atmosphere., Dokl. Akad. Nauk. USSR., 91, 181–183.

Troitskaya, V. A., Plyasova-Bakounina, T. A., and Gul'elmi, A., 1971, Relationship between Pc2-4 pulsations and the interplanetary magnetic field., Dokl. Akad. Nauk. SSSR., 97, 1312–1314.

Ulrych, T. J., 1972, Maximum entropy power spectrum of truncated sinusoids., J. Geophys. Res., 77, 1396–1400.

Ulrych, T. J. and Clayton, R. W., 1976, Time series modelling and maximum entropy., Phys. Earth Planet. Inter., 12, 188–200.

Varga, M., 1980, A numerical study of the excitation of Pc2-4 type pulsations., J. Atm. Terr. Phys., 42, 365–369.

Vellante, M., Lühr, H., Zhang, T. L., Wesztergom, V., Villante, U., De Lauretis, M., Piancatelli, A., Rother, M., Schwingenschuh, K., Koren, W., and Magnes, W., 2004, Ground/satellite signatures of field line resonance: A test of theoretical predictions., J. Geophys. Res. A06 210, doi:10.1029/2004JA010392.,, 109.

Verõ, J., Lühr, H., Vellante, M., Best, I., Střeštik, J., Cz. Miletits, J., Holló, L., Szendrõi, J., and Zieger, B., 1998, Upstream waves and field line resonances: simultaneous presence and alternation in Pc3 pulsation events., Ann. Geophys., 16, 34–48.

Walker, A. D. M., 2002, Excitation of field line resonances by MHD waves originating in the solar wind., J. Geophys. Res. 107, 1481, doi:10.1029/2001JA009188,, 107.

Walker, A. D. M., 2005, Magnetohydrodynamic waves in geospace: The theory of ULF waves and their interaction with Energetic Particles in the Solar-Terrestrial Environment., IOP publishing Ltd.

Walker, A. D. M., Greenwald, R. A., Stuart, W. F., and Green, C. A., 1978, Resonance region of a Pc5 micropulsation examined by a dual auroral radar., Nature., 273, 646–649.

Walker, A. D. M., Greenwald, R. A., Stuart, W. F., and Green, C. A., 1979, STARE auroral radar observations of Pc5 geomagnetic pulsations., J. Geophys. Res., 84, 3373–3388.

Walker, A. D. M., Ruohoniemi, J. M., Baker, K. B., Greenwald, R. A., and Samson, J. C., 1992, Spatial and temporal behavior for ULF pulsations observed by the Goose Bay H F radar., J. Geophys. Res., 97, 12187–12202.

Waters, C. L., 2000, ULF resonance structure in the magnetosphere, Adv. Space. Res., 25, 1541–1558.

Waters, C. L., Anderson, B. J., and Liou, K., 2001, Estimation of global field aligned currents using the Iridium system magnetometer data., Geophys. Res. Lett., 28, 2165–2168.

Waters, C. L., Harrold, B. G., Menk, F. W., Samson, J. C., and Fraser, B. J., 2000, Field line resonances and waveguide modes at low latitudes: 2. A model., J. Geophys. Res., 105, 7763–7774.

Waters, C. L., Menk, F. W., and Fraser, B. J., 1991a, The resonance structure of low latitude field line resonances., Geophys. Res. Lett., 18, 2293–2296.

Waters, C. L., Menk, F. W., and Fraser, B. J., 1994, Low-latitude geomagnetic field line resonance: experiment and modeling., J. Geophys. Res., 99, 17547–17558.

Waters, C. L., Menk, F. W., Fraser, B. J., and Ostwald, P. M., 1991b, Phase structure of low-latitude Pc3-4 pulsations., Planet. Space Sci., 39, 569–582.

Waters, C. L., Samson, J. C., and Donovan, E. F., 1995, The temporal variation of the frequency of high latitude field line resonances., J. Geophys. Res., 100, 7987–7996.

Wilson, C. R. and Sugiura, M., 1961, Hydromagnetic interpretation of sudden commencements of magnetic storms., J. Geophys. Res., 66, 4097–4111.

Wright, A. N., 1994, Dispersion and wave coupling in inhomogeneous MHD waveguides, J. Geophys, Res., 99, 159–167.

Yoshikawa, A. and Itonaga, M., 1996, Reflection of shear Alfvén waves at the ionosphere and the divergent Hall curent., Geophys. Res. Lett, 23, 101–104.

Yoshikawa, A. and Itonaga, M., 2000, The nature of reflection and mode conversion of MHD waves in the inductive ionosphere: Multistep mode conversion between divergent and rotational electric fields., J. Geophys. Res., 105, 10565–10584.

Yumoto, K., Saito, T., Tsurutani, B. T., Smith, E. J., and Akasofu, S.-I., 1984, Relationship between the IMF magnitude and Pc3 magnetic pulsations in the magnetosphere., J. Geophys. Res., 89, 9731–9740.

Zmuda, A. J., Martin, J. H., and Heuring, F. T., 1966, Transverse magnetic disturbances at 1100 km in the auroral region., J. Geophys. Res., 71, 5033–5045.